

©2018

Alexander Hook

ALL RIGHTS RESERVED

A DFT STUDY OF HYDROGEN ABSTRACTION FROM
LIGHT ALKANES:
Pt ALLOY DEHYDROGENATION CATALYSTS AND
TiO₂ STEAM REFORMING CATALYSTS

By

ALEXANDER HOOK

A dissertation submitted to the

School of Graduate Studies

Rutgers, The State University of New Jersey

In partial fulfillment of the requirements

For the degree of

Doctor of Philosophy

Graduate Program in Chemical and Biochemical Engineering

Written under the direction of

Fuat E. Celik

And approved by

New Brunswick, New Jersey
May, 2018

ABSTRACT OF THE DISSERTATION

A DFT STUDY OF HYDROGEN ABSTRACTION FROM LIGHT ALKANES:
Pt ALLOY DEHYDROGENATION CATALYSTS AND TiO₂ STEAM REFORMING
CATALYSTS

By ALEC HOOK

Dissertation Director:

Fuat E. Celik

Sustainable energy production is one of the biggest challenges of the 21st century. This includes effective utilization of carbon-neutral energy resources as well as clean end-use application that do not emit CO₂ and other pollutants. Hydrogen gas can potentially solve the latter problem, as a clean burning fuel with very high thermodynamic energy conversion efficiency in fuel cells. In this work we will be discussing two methods of obtaining hydrogen. The first is as a byproduct of light alkane dehydrogenation where we obtain a high value olefin along with hydrogen gas. The second is in methane steam reforming where hydrogen is the primary product.

Chapter 1 begins by introducing the reader to the current state of the energy industry. Afterwards there is an overview of what density functional theory (DFT) is and how this computational technique can elucidate and complement laboratory experiments. It will also contain the general parameters and methodology of the VASP software package that runs the DFT calculations.

Chapter 2 will introduce the reader to light alkane dehydrogenation over platinum. Then this chapter goes into detail about the current industry standard alloy, PtSn, and how it dehydrogenates light alkanes. After the dehydrogenation process, the olefin may be further dehydrogenated into coke precursors which are often thought of as atomic carbon. This work looks into this claim by continuing the dehydrogenation down to atomic carbon and testing its thermodynamic and kinetic possibilities.

Chapter 3 will follow up with light alkane dehydrogenation over various platinum alloys. This work consists of a comprehensive comparison of alloys of platinum with transition and post-transition metals. Trends in reactivity will be used to predict optimum alloy compositions.

Chapter 4 will introduce a common method of removing carbon monoxide while producing hydrogen gas, the water gas shift (WGS) reaction. The various WGS kinetic pathways over TiO_2 have been mapped out including all thermodynamic reaction energies. These energies indicate the most probable pathways for WGS over anatase TiO_2 . The role of water in the elementary reaction steps is of special interest.

Chapter 5 expands the scope of TiO_2 surface reactions to include methane steam reforming coupled with the WGS reaction. The role of water in methane activation is examined, and the predicted reaction pathways are explored in the presence of adsorbed water molecules. The potential energy surfaces for steam reforming have been investigated along with both binding energies and activation energies.

Acknowledgements

I would like to express my heartfelt gratitude to my advisor Dr. Fuat E. Celik for his guidance and support throughout my Ph. D. endeavor at Rutgers University. His encouragement and assistance was crucial as we both stumbled along in establishing the group's computational division. His passion for catalysis and guidance has helped shape me over the past years.

I would also acknowledge my committee members: Dr. Alexander V. Neimark and Dr. Alan S. Goldman for their assistance in both my thesis proposal and defense, Dr. George Tsilomelekis for his support on my thesis defense committee, and Dr. Yee C. Chiew for his help with my thesis proposal committee.

I thank the Celik group members for the great working environment and for their company. I would like to give special thanks to Ashley Pennington for her assistance on the TiO₂ project and Deniz Dindi for his assistance in setting up our group's supercomputer.

Finally, I want to thank my family, without whom I would not have been able to last on this long, long endeavor.

Table of Contents

ABSTRACT.....	ii
Acknowledgements.....	iv
Table of Contents.....	v
Table of Figures	ix
Table of Tables	xiv
Chapter 1: Background and General Introduction	1
Chapter 2: Light alkane dehydrogenation over Pt and PtSn	5
2.1 Introduction.....	5
2.2 Methods.....	9
2.3 Results and Discussion	10
2.3.1 Model Pt _x Sn/Pt(111) Surfaces	10
2.3.2 Binding of CH _x & H species.....	12
2.3.3 C-H bond-breaking steps in CH _x species.....	16
2.3.4 Binding of C ₂ H _x species.....	20
2.3.5 Hydrogen coadsorption with C _x H _y species	24
2.3.6 C-H bond-breaking steps in C ₂ H _x species and ethene formation	26
2.3.7 C-C bond-breaking steps in C ₂ H _x species.....	32
2.3.8 Minimum energy pathway to atomic carbon	34
2.4 Conclusions.....	36

2.A Supporting Information: Pictorial Mechanisms for C _x H _y dehydrogenation on Pt and PtSn alloys.....	38
Chapter 3: Light alkane dehydrogenation over various Pt Alloys	50
3.1 Introduction.....	50
3.2 Methods.....	53
3.3. Results and Discussion	54
3.3.1 Model Pt _x M/Pt(111) Surfaces	56
3.3.2 Binding of CH _x & H species	59
3.3.3 Binding of C ₂ H _x	62
3.3.4 Ethene Dehydrogenation Mechanism	67
3.3.5 Selectivity	68
3.3.5 Scaling Relations	70
3.4. Conclusions.....	76
3.A Supporting Information: PtM alloys	78
Chapter 4: Density Functional Theory Investigation of the Role of Cocatalytic Water in Water Gas Shift Reaction over Anatase TiO ₂ (101)	81
4.1 Introduction.....	81
4.2 Methods.....	84
4.3 Results and Discussion	85
4.3.1 Model Anatase TiO ₂ (101) Surface.....	85

4.3.2 Binding of WGS intermediates	86
4.3.2.1 Hydrogen Adsorption.....	88
4.3.2.2 Water Adsorption.....	90
4.3.2.3 Cationic Adsorbates	93
4.3.2.4 Anionic Adsorbates.....	94
4.3.2.5 Molecular Adsorbates	96
4.3.3 Oxygen Vacancies	96
4.3.4 Elementary Reactions in WGS Reaction Mechanism	97
4.3.5 Cocatalytic Water.....	102
4.4 Conclusions.....	110
Chapter 5: Density Functional Theory Investigation of the Role of Cocatalytic Water in	
Methane Steam Reforming over Anatase TiO ₂ (101).....	112
5.1 Introduction.....	112
5.2 Methods.....	115
5.3 Results and Discussion	116
5.3.1 Model TiO ₂ Surfaces.....	116
5.3.2 MSR Reaction Pathways and Intermediates	118
5.3.2.1 Binding of CH _x Species	120
5.3.2.2 Binding of CH _x O Species	123
5.3.2.3 Binding of CO _x Species	128

5.3.3 Methane Steam Reforming Pathways	128
5.3.4 Elementary Reactions without Assistance from Cocatalytic Water	133
5.3.5 Effect of Cocatalytic Water on Dehydrogenation Steps and MSR Pathways	139
5.4 Conclusions.....	144
Bibliography	147

Table of Figures

Figure 1.1 Fischer-Tropsch Synthesis, a process that produces hydrocarbons of varying length. When producing maximum gasoline about 25% is C1-C3.	1
Figure 1.2: Catalytic ethane dehydrogenation: Light alkane dehydrogenation produces both the olefin and hydrogen gas byproduct	3
Figure 2.1: Best binding geometries of H and CH _x species on Pt and alloy surfaces.	14
Figure 2.2: Two-dimensional potential energy surfaces for successive dehydrogenation of CH _x species beginning with CH _{4(g)} on Pt(111) and Pt/Sn alloys. Ordinate is energy relative to CH ₄ in the gas phase. Gaseous species are indicated; all others are adsorbed on the metal surface. All species are at infinite separation. Hydrogen atoms remain on surface at infinite separation, and are omitted from labels for clarity. Potential energy surface on Pt(111) shown in black, on Pt ₃ Sn/Pt shown in red, and on PtSn/Pt shown in blue.....	17
Figure 2.3: Best binding geometries of H and CH _x species on Pt and alloy surfaces.	23
Figure 2.4: Two-dimensional potential energy surfaces for successive dehydrogenation of C ₂ H _x species beginning with C ₂ H _{6(g)} on a) Pt(111), b) Pt ₃ Sn/Pt, and c) PtSn/Pt. Ordinate is energy relative to C ₂ H ₆ in the gas phase. Gaseous species are indicated; all others are adsorbed on the metal surface. All species are at infinite separation. Hydrogen atoms remain on surface at infinite separation, and are omitted from labels for clarity. Ethene/vinyl/vinylidene pathway shown in blue, ethylidene/ethylidyne/vinylidene pathway shown in red, and ethylidene/vinyl/acetylene pathway shown in black.....	31

Figure 3.1: The three possible pathways for adsorbed ethene with Pt(111) energies. BOLD is the thermodynamic change in energy and <i>italic</i> is the kinetic barrier in eV. 0	55
Figure 3.2: Binding site preferences of carbon atoms on three categories of alloying elements: post-transition (P-T) metals, non-preferred transition (NT) metals, and carbon-preferred transition (CT) metals.	58
Figure 3.3: A relationship between methyl binding energy (BE_{CH_3}) and desorption energy of ethene (ΔE_{des}) at a) $\frac{1}{4}$ ML and b) $\frac{1}{2}$ ML coverage. NT alloys in blue, P-T alloys in black, and CT alloys in red.	72
Figure 3.4: A linear relationship between the methylidyne dehydrogenation reaction energy (ΔE_{CH}) plus the methyl binding energy (BE_{CH_3}) verses ethene dehydrogenation barrier ($E_{a,ethene}$) for alloys at $\frac{1}{4}$ ML coverage. NT alloys in blue, and P-T alloys in black.	74
Figure 4.1 Anatase (101) unit cell used in calculations a) side view with near-surface unique atoms numbered and b) top view. Titanium atoms (grey) are labelled with two digits and oxygen atoms (red) by three digits. Edges of calculation unit cell are shown by black borders. Oxygen atoms O#100, O#101 and O#110 are accessible from the surface and O#100 is coordinatively unsaturated. Titanium atoms Ti#10 and Ti#11 are accessible from the surface with Ti#10 coordinatively unsaturated. Each unique atom repeats four times per unit cell.	86
Figure 4.2 Best binding orientations of adsorbates on anatase (101), including physisorbed water, $H_2O_{(p)}$, and chemisorbed water, $H_2O_{(c)}$ water. Reduced Ti^{3+} center	

is labelled in H _{#1000} . H adsorbs as a proton, H ₂ O _(c) as a proton/hydroxide anion pair, OH and O as radicals, and H ₂ O _(p) adsorbs molecularly.	93
Figure 4.3 Best binding orientations of CH _x O _y species on anatase (101). Reduced Ti ³⁺ centers are labelled where present. CHO and CO ₂ H adsorb as cations, HCOO adsorbs as an anion and is coadsorbed with a proton, and CO and CO ₂ adsorb molecularly. 95	
Figure 4.4 Reaction pathways for direct CO oxidation (blue), associative carboxyl (red), and associative formate (purple) pathways. Common steps (CO and H ₂ O physisorption, water activation to form H ₂ O _(c) , and CO ₂ and H ₂ desorption) are shown in black. All species are surface species at infinite separation except gases as indicated and as follows: H ₂ O _(c) is OH+H coadsorbed on the same slab, HCOO+H are coadsorbed on the same slab, and CHO+OH are coadsorbed on the same slab.	101
Figure 4.5 CO hydrogenation mechanism unassisted (without participation of a cocatalytic water molecule) and with cocatalytic water. The physisorbed water molecule acts as a hydrogen donor, bridging the spatial gap between donor and acceptor and reducing the activation energy barrier relative to the unassisted case. IS is the initial coadsorbed state, TS is the transition state, and FS is the final coadsorbed state.	105
Figure 4.6 Reaction pathways including the effect of cocatalytic water for direct CO oxidation (blue), associative carboxyl (red), and associative formate (purple) pathways. Common steps (CO and H ₂ O physisorption, water activation to form H ₂ O _(c) , and CO ₂ and H ₂ desorption) are shown in black. All species are surface species at infinite separation except gases as indicated and as follows: H ₂ O _(c) is	

OH+H coadsorbed on the same slab, HCOO+H are coadsorbed on the same slab, and CHO+OH are coadsorbed on the same slab.	109
Figure 5.1 Side view of the best binding orientations of water on anatase (101) in its physisorbed and chemisorbed states. Chemisorbed water is bound as an OH ⁻ /H ⁺ anion/cation pair from the heterolytic cleavage of the O-H bond in physisorbed water.	
	118
Figure 5.2 Best binding orientations of CH _x species on anatase (101). Reduced Ti ³⁺ centers are labelled where present. CH ₃ , CH, and C adsorb as cations, and CH ₂ adsorbs as a neutral species.	
	123
Figure 5.3 Best binding orientations of CH _x O species on anatase (101). Reduced Ti ³⁺ centers are labelled where present. CH ₂ OH, CHOH, CHO and COH adsorb as cations, CH ₃ O adsorbs as an anion and is coadsorbed with a proton, and CH ₃ OH, CH ₂ O, CO and CO ₂ adsorb molecularly.	
	128
Figure 5.4 Potential energy surfaces for methane steam reforming mechanisms on anatase TiO ₂ (101). Elementary steps include dehydrogenation (blue), oxidation by O (red), and OH addition (yellow). Additional steps include water physisorption (purple), chemisorption (green), and water-gas shift reaction (black). WGS mechanism not shown in detail except for CHO/HCOO pathway. State of any water molecules present indicated by (g) gaseous, (p) physisorbed, (c) chemisorbed. Surface hydrogen atoms as products omitted for clarity, and associative desorption as H ₂ included with final CO and CO ₂ desorption steps. All species are surface species at infinite separation except for gaseous species and coadsorbed species as follows: H ₂ O _(c) or	

OH+H, and CH₃O+H which are coadsorbed as anions and protons on the same slab.

..... 132

Figure 5.5 Methane hydrogenation mechanism unassisted (without participation of a cocatalytic water molecule) and with cocatalytic water. IS is the initial coadsorbed state, TS is the transition state, and FS is the final coadsorbed state. 138

Figure 5.6 Reaction pathways without (A) and with (B) the effect of cocatalytic water on dehydrogenation barriers. Reaction steps common in all pathways shown in black, methoxyl pathway in green, direct methylene pathway in blue, indirect methylene (hydroxymethyl) pathway in yellow, CO/carboxyl WGS pathway in red, and formate WGS pathway in purple. See Figure 5.4 for labelling conventions. The energy to chemisorb water, +0.22 eV, is included in the barrier heights for reactions which utilize cocatalytic water in B. 142

Table of Tables

Table 1.1 MSR and Water Splitting: A Thermodynamic Comparison	4
Table 2.1 Structure of Pt(111) and platinum-tin substitutional surface alloys used in this study. Grey spheres: Pt; Green spheres: Sn	11
Table 2.2 Binding energies and site preferences of reaction intermediates on (111) surfaces at $\frac{1}{4}$ ML adsorbate coverage.....	12
Table 2.3 Comparison of binding energies and site preferences of reaction intermediates on Pt ₃ Sn/Pt with no coordination to Sn (preferred) and the best possible binding with at least one bond between C and Sn at $\frac{1}{4}$ ML adsorbate coverage.....	15
Table 2.4 Activation energy and heat of reaction for all elementary steps. All species are surface species except for gaseous species as noted.....	19
Table 2.5 Binding energies of C ₂ H _x species on Pt and PtSn alloys	22
Table 2.6 Binding energies (in eV) of C ₂ H _x species in the presence of a hydrogen observer: $BE = E_{\text{slab}}(\text{H} + \text{C}_x\text{H}_y) - E_{\text{slab}}(\text{H}) - E_{\text{C}_x\text{H}_y}$	24
Table A.1 Initial, final, and transition state structures for each elementary reaction step for dehydrogenation of CH _x species on Pt(111), Pt ₃ Sn/Pt, and PtSn/Pt.	38
Table A.2 Initial, final, and transition state structures for each elementary reaction step for C ₂ H _x species on Pt(111).	40
Table A.3 Initial, final, and transition state structures for each elementary reaction step for C ₂ H _x species on Pt ₃ Sn/Pt	43
Table A.4 Initial, final, and transition state structures for each elementary reaction step for C ₂ H _x species on PtSn/Pt 0	46

Table 3.1 Binding Energies and Site Preferences for H & CH _x species on various (111) Surfaces	60
Table 3.: Best binding geometries for CH _x and H species on Pt and alloy surfaces. PtIn alloy shows the binding locations for all P-T and NT alloys. PtRe alloy shows the binding locations for CT alloys.....	62
Table 3.3: C ₂ H _x BE & locations on Pt alloy	65
Table 3.4 Best binding geometries of C ₂ H _x species on Pt, NT, and P-T alloys. b) Expanded table for vinyl on PtM alloys	66
Table 3.5: Activation Energy ^a and Reaction Energy ^a for ethene dehydrogenation (in eV), CH ₂ CH ₂ * + * → CH ₂ CH* + H*	68
Table 3.6: The DFT-calculated selectivity descriptor values on Pt alloys (in eV)	70
Table 3.7 Selectivity Predictors and descriptors for ethene dehydrogenation for ¼ ML coverage alloys.	75
Table 4.1 Hydrogen binding energies in eV, and localized charge on adjacent Ti atoms.	90
Table 4.2 Binding energies of molecular and WGS intermediate species on anatase (101) in eV	94
Table 4.3 Oxygen vacancy formation energies in eV, identified by the O atom removed. Oxygen is removed as ½O ₂ (g).	97
Table 4.4 Binding energy of chemisorbed water with and without water on the both sides of the slab	98
Table 4.5 Reaction energies and activation energy barriers for elementary steps in WGS reaction mechanism where water acts as a cocatalyst.	107
Table 5.1 Binding energies of MSR intermediates species on anatase (101) in eV.	126

Table 5.2 Reaction energies for elementary steps in MSR mechanism.....	130
--	-----

Table 5.3 Reaction energies and activation energy barriers in eV for elementary steps in MSR.	137
---	-----

_Toc507882866

Chapter 1: Background and General Introduction

Hydrogen gas has received much acclaim as a clean-burning energy carrier that can be used in fuel cells. Not only do hydrogen fuel cells not produce carbon dioxide, they can be used in both mobile and stationary systems with a higher thermodynamic efficiency than conventional internal combustion engines. In this work we have included hydrogen formation as a primary and by-product.

Light alkanes such as ethane are common products of industrial hydrocarbon processing including petroleum cracking, Fischer-Tropsch synthesis, and ethane hydrocracking. Light alkane dehydrogenation has gained increased interest due to the recent development of shale deposits in North America, which are ‘wet,’ i.e. contain considerable amounts of natural gas liquids.¹ In North America, this influx of light alkanes has displaced naphtha cracking as the major source of light alkenes. One of the primary methods of obtain these light alkenes is through light alkane dehydrogenation which produces both the light alkene and hydrogen gas.

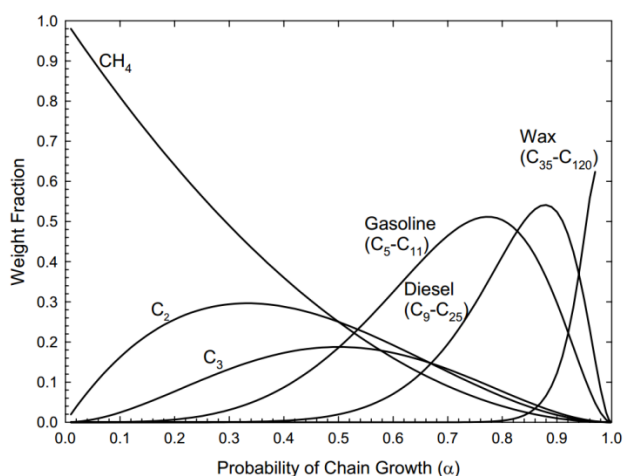


Figure 1.1 Fischer-Tropsch Synthesis, a process that produces hydrocarbons of varying length. When producing maximum gasoline about 25% is C1-C3. **0-1.0-2**

Many reaction systems for the dehydrogenation of light alkanes have been developed, including steam cracking, catalytic oxidative dehydrogenation, and catalytic dehydrogenation.¹⁻⁸ The high temperatures in steam cracking generate large amounts of carbonaceous deposits on reactor walls, requiring periodic reactor downtime for coke removal. Oxidative dehydrogenation removes hydrogen from the alkane as water by reacting with oxygen. A significant selectivity challenge exists however between the oxidative dehydrogenation of the alkane and the even faster combustion of the alkene product. Catalytic dehydrogenation requires lower temperatures than steam cracking, potentially leading to lower overall coke formation. Without oxygen, combustion is not a concern, and usable H₂ gas is generated as a valuable byproduct instead of water vapor.

Despite these advantages, catalytic dehydrogenation is still an endothermic reaction, requiring relatively high temperatures above 700 K. Consequently, coke formation is still a major drawback for the process.⁷⁻⁹ Additionally, coke deposits in catalyst pores or on active sites of a heterogeneous catalyst are especially problematic as they may block mass transport of products and reactants to and from the catalyst surface. Coke buildup is typically removed at high temperature under oxygen flow, though exposure of catalysts to very high temperatures may cause changes in metal nanoparticle size by sintering. As a common cause of catalyst deactivation in a number of reactions and industrial chemical processes, coke formation has received extensive attention in the literature.¹⁰⁻¹²

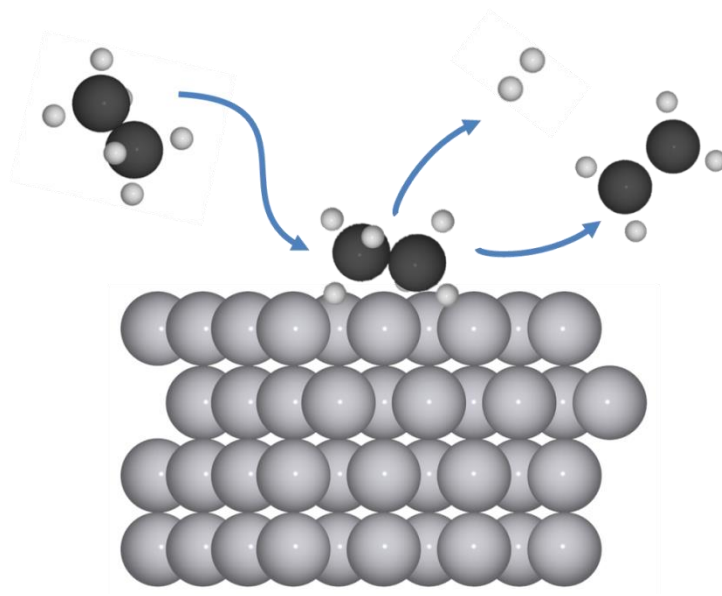


Figure 1.2: Catalytic ethane dehydrogenation: Light alkane dehydrogenation produces both the olefin and hydrogen gas byproduct 0-3

Water and methane are the two commonly investigated reactants for hydrogen production. Water splitting is appealing because it is carbon neutral and the abundance of water, however this reaction is extremely endothermic and endergonic. Methane steam reforming (MSR) is a process used industrially and converts fossil methane to hydrogen gas and carbon monoxide. While MSR is less endothermic and endergonic than water splitting, it still operates at fairly high temperatures (1000°C) and requires a large amount of energy to maintain this temperature. This leads to at least 50% of the methane being burned to generate heat which also produces carbon dioxide. Using sunlight, photocatalysis can be used to produce hydrogen gas and reduce the amount of methane used for heating.

The water gas shift (WGS) reaction is a process that often used in conjunction with the manufacturing of ammonia, hydrocarbon, methanol and hydrogen. The WGS reaction is a critical reaction in Fischer-Tropsch synthesis to regulate the CO and H₂

ratio. Paired with MSR, the WGS reaction is a process used to maximize hydrogen gas formation from methane. Additionally when used in fuel cells, the WGS reaction can be used to minimize CO released which can damage the fuel cell.¹³ By utilizing both the MSR and WGS, a separations process of CO can also be avoided.

Table 1.1 MSR and Water Splitting: A Thermodynamic Comparison **0-1**

Reaction	ΔG° (kJ mol ⁻¹)	ΔH° (kJ mol ⁻¹)	ΔS° (J mol ⁻¹ K ⁻¹)	$T_{\Delta G=0}^b$ (K)
MSR ^a $\text{CH}_4 + 2 \text{H}_2\text{O} \rightarrow \text{CO}_2 + 4 \text{H}_2$	113	165	173	954
Water Splitting $\text{H}_2\text{O} \rightarrow \frac{1}{2} \text{O}_2 + \text{H}_2$	229	242	45	5434

^aIncludes water gas shift reaction, $\text{CO} + \text{H}_2\text{O} \rightarrow \text{CO}_2 + \text{H}_2$, ^bTemperature at which $\Delta G = \Delta H^\circ - T\Delta S^\circ = 0$

Density Functional Theory (DFT) has been used to provide fundamental insight into the properties and catalyst function of many reactions such as methane steam reforming^{14,15} and alkane dehydrogenation.^{16–19} DFT calculations have corroborated and predicted many experimental results. For example, DFT has confirmed that the adsorption energy for alkenes is less on platinum-tin alloys as compared to pure Pt, and is in good agreement with experiment.

Chapter 2: Light alkane dehydrogenation over Pt and PtSn

2.1 Introduction

Light alkanes such as ethane and propane are produced in a number of industrial processes. They are often found as byproducts of hydrocarbon processing, including petroleum cracking, Fischer-Tropsch synthesis, and are minority components of natural gas. The recent shale gas boom has greatly increased the supply of these light alkanes as a significant fraction of North American shale gas deposits are “wet,” i.e. contain significant quantities of natural gas liquids (NGL).²⁰ The price of ethane in particular has fallen considerably as a result of this increased supply,²¹ so much so that much of it is flared rather than recovered. Diverting this source of CO₂ emissions by producing higher value chemicals from these light hydrocarbons would add considerable value to and reduce the carbon footprint of shale gas extraction.

These alkanes themselves have limited value as chemicals and are too light to blend with liquid fuels. The corresponding alkenes, ethene and propene, by contrast have high value as chemical precursors for a wide range of chemical and polymer products.

Catalytic dehydrogenation requires lower temperatures than steam cracking, leading to lower overall coke formation. Without oxygen, combustion is not a concern, and usable H₂ gas is generated as a valuable byproduct instead of water vapor. Despite the advantages catalytic dehydrogenation has over its alternatives, it is still an endothermic reaction, requiring relatively high temperatures above 700 K. Consequently, coke formation is still a major drawback for the process.^{7,8,22} Additionally, coke deposits in catalyst pores or on active sites of a heterogeneous catalyst are especially problematic

as they may block mass transport of products and reactants to and from the catalyst surface. Coke buildup is typically removed at high temperature under oxygen flow, though exposure of catalysts to very high temperatures may cause changes in metal nanoparticle size by sintering. As a common cause of catalyst deactivation in a number of reactions and industrial chemical processes, coke formation has received extensive attention in the literature.^{23–25}

Supported Pt particles are the preferred catalysts for light alkane dehydrogenation.^{7,8,26} Pt is the most active pure metal for light alkane dehydrogenation and shows high selectivity at short reaction times. The alkenes formed from dehydrogenation bind strongly to the Pt surface, making desorption difficult and facilitating subsequent further dehydrogenation or C-C bond cleavage – leading to the formation of carbonaceous surface species.^{27–29} Consequently, catalyst deactivation is rapid and correlates with large deposits of coke.

Reductions in both catalyst deactivation and coke formation relative to pure Pt have been achieved by alloying Pt with Sn.^{8,30–34} Alloying with Sn weakens the interaction of the alkenes with the alloy surface, which allows the product to desorb from the catalyst surface more readily as compared to pure Pt.^{27–32} The rates of further dehydrogenation and C-C bond cleavage are reduced as a result as desorption of the alkene competes with dissociation. However, the activation energy barriers for dehydrogenation of ethyl radicals (derived from ethane) to revert to ethane doubled on platinum-tin alloys as compared to pure Pt,²⁸ so a reduction of activity may be expected over the alloys. Deactivation was reduced by 60% for ethene dehydrogenation relative to pure Pt by alloying with Sn while total carbon formation was reduced by 50%.³⁴ Propane

dehydrogenation activity fell by 39% due to coke formation after two hours, while ethane dehydrogenation fell by only 2% in the same time, even though less total coke was formed in propane dehydrogenation.

Density Functional Theory (DFT) has been used to provide fundamental insight into the properties and catalyst function of alkane dehydrogenation catalysts. DFT calculations confirm that the adsorption energy for alkenes is less on platinum-tin alloys as compared to pure Pt,¹⁶⁻¹⁹ in good agreement with experiment.²⁷⁻³² Stepped sites on Pt(211) are more active than Pt(211) or Pt (111) terraces, but are also less selective towards the alkene in ethane dehydrogenation³⁵⁻³⁶ and propane dehydrogenation.³⁷ Under-coordinated step and edge sites have also been implicated in methane activation on Pt.³⁸ Calculations on Pt(111) suggest that alkynes are the precursor stage for C-C bond cleaving reactions on the path towards alkene cracking and possible coke formation,³⁹ so suppression of alkyne formation or promotion of the conversion of alkynes back to alkenes is suggested as an important step towards reducing coke formation. The activation energy barrier for propene dehydrogenation (which is the first step towards propyne and eventually to coke) is larger on platinum-tin alloys than for propene desorption.⁴⁰ The difference in energy between these key steps increased with increasing Sn content, in good agreement with the experimentally observed trend in less carbon formation over catalysts with greater Sn content.⁴¹ At the same time, the alloying eliminates some of the most unselective reaction sites at the step edges of Pt. In platinum-tin alloys, Sn atoms decorate these edge sites, rendering them inert towards the undesirable dehydrogenation of propene.⁴² The properties of platinum-tin alloys have

also been studied using DFT for ethylene epoxidation,^{17,43} ethanol dehydrogenation,⁴⁴ CO oxidation,^{45–47} and reactions of cyclic ketones.⁴⁸

From prior DFT investigation on Pt and platinum-tin alloys, the competition between desorption and dehydrogenation of the alkene has been implicated as the primary selectivity-determining step, implying that surfaces with more facile desorption and more difficult C-H bond cleavage may show enhanced selectivity. The binding and bond-dissociation energies of the alkenes have been explained in terms of electronic and geometric effects. The electronic effect arises from the change in electronic properties at the binding site of the catalyst due to the neighboring alloying element, without directly affecting the binding geometry. The geometric effect describes the additional effect when the alloying element is present at the binding site, leading to different binding site geometries or different binding modes. At low alloy element coverages, binding geometries may remain unchanged relative to pure Pt, i.e. di- σ binding with each carbon bonded to a different Pt atom.¹⁷ Both electronic and geometric effects may contribute when this binding geometry is not possible at higher alloying ratios when there are no adjacent Pt atoms.

To date, computational studies have only considered low coverages of tin in platinum-tin alloys, and then only to compare the dehydrogenation of the alkene with its desorption. These studies have not looked at further dehydrogenation or C-C bond cleavage steps, and have not provided insight into the mechanism of coke formation on platinum-tin alloys.

In this chapter, we have calculated the complete reaction network from ethane to all dehydrogenated and C-C bond cleaved derivatives, including ethene, and compared the reaction energies and activation energy barriers for all elementary reaction steps. We compare the potential energy surfaces for the pure Pt(111) surface to a low tin Pt₃Sn/Pt(111) surface and a high tin PtSn/Pt(111) surface, and predict selectivity to coke and ethene as a function of tin coverage.

2.2 Methods

Periodic, self-consistent DFT calculations were performed using the VASP code^{49,50} within the generalized gradient approximation (GGA-PW91)⁵¹ using projector-augmented wave (PAW)^{52, 53} potentials. The single-electron wave functions were expanded using plane waves with an energy cutoff of 400eV. All metal slabs were based on the (111) surface of fcc Pt, and modeled by a (2 × 2) surface unit cell with four atomic layers for a total of 16 metal atoms (Pt or Sn). A larger (3 × 3) unit cell was tested for periodic image interaction effects, but these effects were small (<0.05 eV) and were consistent between adsorbates of different sizes (e.g. 0.006 eV difference between ethyl and methyl adsorbates). The choice of a smaller unit cell size therefore has a small effect on reported binding energies and a negligible effect on reaction energies.

To generate the surface substitutional alloys, surface Pt atoms were substituted by Sn and the surface structure was reoptimized by relaxation. Substituting one Pt atom by Sn in the surface layer gives ¼ monolayer (ML) Sn coverage, and substituting two Pt atoms gives ½ ML coverage. The lattice constant of Pt was calculated to be 3.98 Å, in good agreement with experimental value of 3.92 Å.⁵⁴ A vacuum layer of 12 Å was used to separate any two successive slabs in the *z* direction (normal to the surface), and a

dipole correction was applied and the electrostatic potential was adjusted to ensure that interaction between the surface slab and its periodic images was negligible.⁵⁵ The Brillouin zone was sampled using a (6x6x1) Gamma-centered Monkhorst-Pack k-point mesh⁵⁶ following a convergence test for adsorbate binding energies with respect to sampling mesh size. The bottom two layers of each metal slab were fixed in their bulk positions while the top two layers were allowed to relax in all calculations. Binding energy is defined as $BE = E_{ads} - E_{slab} - E_{gas}$, where E_{ads} , E_{slab} , E_{gas} are the total energies calculated for the slab with the adsorbate on it, the clean slab, and the adsorbate in the gas phase, respectively. The addition of a single adsorbate molecule to a metal slab with a (2 × 2) surface until cell corresponds to ¼ ML adsorbate coverage. The climbing image nudged elastic band (CINEB) method⁵⁷ was used to calculate transition state and activation energy barriers. All transition states were verified by identifying a single imaginary frequency along the reaction coordinate. Direction and magnitude of electronic charge transfer between Sn and Pt upon alloying was calculated using Bader charge analysis^{58–61}. All calculated energies were extrapolated to 0 K without zero point energy corrections.

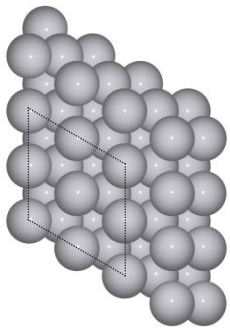
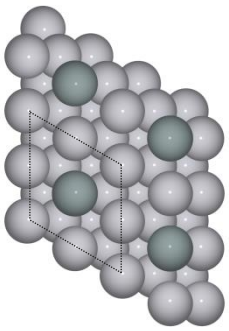
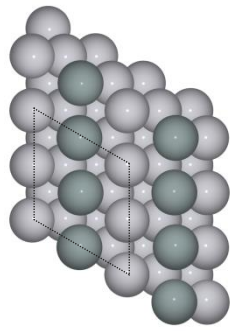
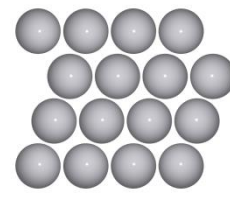
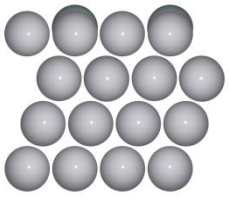
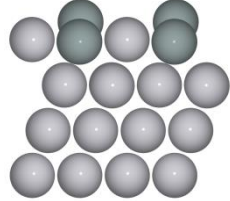
2.3 Results and Discussion

2.3.1 Model Pt_xSn/Pt(111) Surfaces

The phase diagram of platinum-tin alloys includes a number of bulk compositions, including Pt₃Sn, PtSn, and PtSn₂.^{62,63} Two types of models for these surfaces have been reported previously in the literature: bulk alloys, where Sn is found throughout all layers of the alloy,^{17,19,40,42,44–47} and surface substitutional alloys, where Sn replaces Pt atoms in the surface layer only.^{18–19,40,43,45,48} In those studies which compared

results between substitutional surface alloys and bulk alloys, the composition of the subsurface (solely Pt atoms in a Pt(111) fcc structure in surface substitutional alloys, and Pt and Sn atoms in a bulk alloy) was far less important than the composition of the surface layer.^{19,40,45} For this reason, the use of surface substitutional alloys was chosen to model platinum-tin alloys of different alloy compositions. Experimental single-crystal studies have shown that surface substitutional alloys with the same or similar structures reported here form for the platinum-tin system.^{27–32,43,48} Using a (2×2) unit cell of fcc Pt(111) with four atomic layers, the model alloy surfaces employed in the current study consist of Pt₃Sn/Pt(111) and PtSn/Pt(111), with $\frac{1}{4}$ ML and $\frac{1}{2}$ ML of the surface layer Pt atoms substituted by Sn respectively (Table 2.1).

Table 2.1 Structure of Pt(111) and platinum-tin substitutional surface alloys used in this study. Grey spheres: Pt; Green spheres: Sn 0-1

	Pt(111)	Pt ₃ Sn/Pt(111)	PtSn/Pt(111)
top view			
side view			
Sn coverage	0 ML	$\frac{1}{4}$ ML	$\frac{1}{2}$ ML

In the Pt₃Sn/Pt surface, the Sn atoms are isolated from one another, with regions of uninterrupted Pt between them. Most importantly, the Pt ensembles form three-fold hollow sites (hcp and fcc sites) consisting of only Pt neighbors that are geometrically similar to those found on pure Pt(111). In the higher Sn alloy, PtSn/Pt, the Sn atoms are adjacent to one another (the lines formed are an artifact of the relatively small (2×2) surface unit cell), and the Pt ensembles are no longer arranged trigonally, such that all three-fold hollow sites consisting of three Pt atoms are eliminated. In this way, the two alloy surfaces used in this study illustrate the differences between low-Sn alloys, where trigonal Pt atom ensembles exist, and high-Sn alloys, where these ensembles do not exist. Surface segregation has been reported for the Pt-Sn alloy system,^{64,65} such that Sn is enriched in the surface layer and depleted from the interior of the alloy particle.

2.3.2 Binding of CH_x & H species

Table 2.2 gives the binding site preferences and binding energies of the hydrogen atom and CH_x species (x = 0 to 4) on the Pt and alloy surfaces.

Table 2.2 Binding energies and site preferences of reaction intermediates on (111) surfaces at ¼ ML adsorbate coverage.0-2

Adsorbate		Pt		Pt ₃ Sn/Pt			PtSn/Pt		
		Site	BE	Site	BE	CN _{Sn}	Site	BE	CN _{Sn}
H	hydrogen	Fcc ^a	-2.76	Fcc	-2.72	0	Top	-2.44	0
H ₂	dihydrogen	*	-0.02	*	-0.02		*	-0.02	
C	carbon	Fcc	-6.97	Fcc	-6.28	0	Fcc	-5.69 ^b	1
CH	methylidyne	Fcc	-6.70	Fcc	-6.07	0	Fcc	-5.28	1
CH ₂	methylene	Bridge	-4.14	Bridge	-3.79	0	Bridge	-3.57	0
CH ₃	methyl	Top	-2.07	Top	-1.85	0	Top	-1.71	1 ^c
CH ₄	methane	*	-0.03	*	-0.04		*	0.04	

BE is the binding energy in eV. **CN_{Sn}** is the coordination numbers of the adsorbate to Sn at the binding site.

*CH₄ and H₂ physisorb weakly with no site preferences.

^a Hydrogen shows a weak preference for binding to higher coordinated sites, with binding to a top site being only 0.06 eV less favorable.

^b In this binding geometry, the Sn, Pt, and C atoms are nearly coplanar, with a Sn-Pt-Pt-C dihedral angle of only 8.9°

^c Binding to the top site of Pt is only 0.02 eV less favorable to binding to the top site of Sn.

The binding site preferences and energies calculated here for H and CH_x species on Pt and on the ¼ ML Sn alloy are consistent with previous reports.^{44,66–69} Binding preferences for methyl, methylene, and methylidyne radicals are consistent with *sp*³-hybridized tetravalent carbon: the number of metal-carbon bonds is 4 – *x*, where *x* is the number of C-H bonds in the radical. Methyl, with three C-H bonds, binds to the surface through a single metal-carbon bond at a top site. Methylene binds to the surface through two metal-carbon bonds at a bridge site. Methylidyne binds to the surface through three metal-carbon bonds at an fcc site. The binding energies for these three species increase with increasing number of metal-carbon bonds on each surface studied here. Following this trend, the carbon atom should form four metal carbon bonds but this is not possible on the (111) surface of Pt or its alloys, and so binds to a three-fold hollow site with three metal-carbon bonds. Consequently, the binding energies for carbon and methylidyne are within 0.5 eV of each other, while the binding energy per carbon-metal bond in each species is roughly 2 eV. Closed-shell species such as CH₄ and H₂ have weak interactions with the surface (physisorption), and consequently the binding energies calculated are small (<0.05 eV) and binding site preferences are negligible.

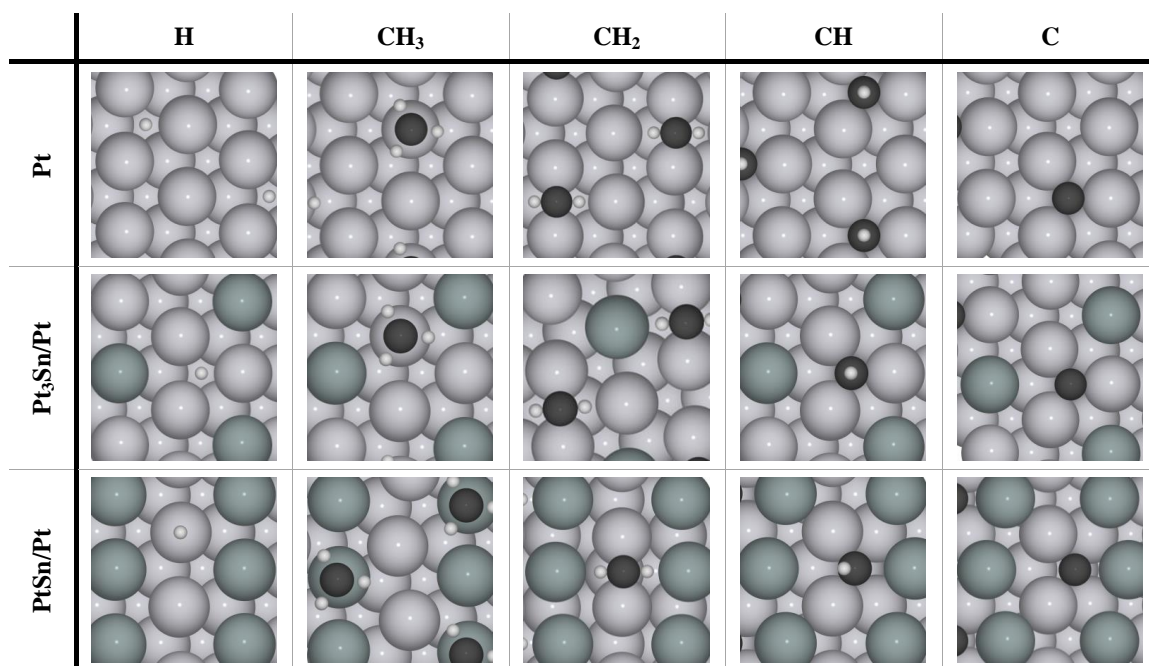


Figure 2.1: Best binding geometries of H and CH_x species on Pt and alloy surfaces.⁰⁻¹

The addition of Sn to the Pt surface contributes to two different effects on the binding of adsorbates on the metal surface, an electronic or ligand effect and a geometric effect.⁷⁰ Here, we use the term electronic effect to account for the increase in electron density of the Pt atoms surrounding Sn as seen through Bader charge analysis. A surface Sn atom substituted into Pt(111) enriches the surrounding surface Pt atoms with +0.22 e⁻ per Pt atom while two Sn atoms enrich the adjacent Pt atoms by +0.43 e⁻. This effect can be termed “indirect” if the adsorbate does not bind to the Sn atoms itself, as the effect is only to influence the strength of the platinum-carbon bonds. The electronic effect dominates the difference in binding energies between Pt(111) and the Pt₃Sn/Pt surfaces. On the Pt₃Sn/Pt surface, all adsorbates strongly prefer binding to sites that avoid interaction with Sn atoms, with identical coordination numbers to platinum as seen on Pt(111). In Figure 2.1, the binding similarity of binding geometries between the two surfaces can also be seen. With no significant changes in binding geometries, the

weakening of binding energies is attributed to a purely electronic effect from the neighboring Sn atoms. This weakening increases with the number of metal-carbon bonds, ranging from 0.22 eV for methyl to 0.69 eV for atomic carbon. As shown in Table 2.3, binding sites that require coordination to Sn are significantly weaker (0.8-1.0 eV) compared to similar sites with no Sn atoms. The exception is for methyl on a top site, where the difference is smaller, only 0.5 eV between binding to Pt and binding to Sn.

Table 2.3 Comparison of binding energies and site preferences of reaction intermediates on Pt₃Sn/Pt with no coordination to Sn (preferred) and the best possible binding with at least one bond between C and Sn at ¼ ML adsorbate coverage.0-3

Adsorbate		Best Binding Site			C-Sn Bonding Sites				
		Site	BE	CN _{Sn}	C-Pt ^a	Site	BE	CN _{Sn}	C-Sn ^a
C	carbon	fcc	-6.28	0	1.96	fcc	-5.33	1	2.39
CH	methylidyne	fcc	-6.07	0	2.02	fcc	-5.21	1	2.22
CH ₂	methylene	bridge	-3.79	0	2.07	bridge	-2.98	1	2.08
CH ₃	methyl	top	-1.85	0	2.09	top	-1.36	1	2.21

BE is the binding energy in eV. **CN_{Sn}** is the coordination numbers of the adsorbate to Sn at the binding site.

^aC-M bond distance in Å.

On the higher Sn-loading ½ ML surface, a distinct contribution from the geometric effect could be seen that was absent on the ¼ ML surface. With the elimination of three-fold Pt sites, methylidyne and carbon prefer to bind to sites consisting of two Pt atoms and one Sn atom. In Figure 2.1, it can be seen that the tin-carbon bond is greatly elongated relative to the platinum-carbon bonds on the same surface, and compared to the platinum-carbon bonds seen on any of the surfaces. Together, the geometric effect and the increased electronic effects arising from higher Sn content in the surface layer lead to binding energies that are even weaker on PtSn/Pt surfaces as compared to Pt₃Sn/Pt surfaces. However, the additional effect on the binding energy was quantitatively similar to the effect of adding a smaller amount of Sn to the Pt surface – i.e. the additional weakening of the binding energies observed between the ¼ ML Sn and ½ ML Sn surfaces were comparable to the difference between Pt(111) and the ¼ ML Sn alloy. The

sole exception was for the H atom where the electronic effects of adding $\frac{1}{4}$ ML of Sn to Pt(111) were minimal (0.04 eV), but the geometric effects when adding $\frac{1}{2}$ ML increased the difference to 0.32 eV. On Pt(111) and Pt₃Sn/Pt, H prefers to bind to a three-fold Pt site, but the elimination of all such sites on the PtSn/Pt leads to a top site over a Pt atom to be the preferred binding site. Carbon and methyldyne bind to three-fold hollow sites; the very weak interaction between carbon and tin leads to elongated C-Sn bonds (2.39 Å and 2.22 Å respectively), as compared to the C-Pt bonds (1.96 Å and 2.02 Å). On the PtSn/Pt surface, methyl shows a slight preference for binding to a Sn top site over Pt with a difference in binding energy of 0.02 eV.

2.3.3 C-H bond-breaking steps in CH_x species

The potential energy surfaces for the successive dehydrogenation of CH_x species, beginning with CH_{4(g)}, on each catalyst surface are given in Figure 2.2. The reaction and activation energies for each elementary step are given in Table 2.4. On Pt(111), the breaking of the first C-H bond in methane is essentially thermoneutral (with an activation barrier of 0.91 eV) and the second C-H bond is slightly uphill (0.18 eV, similar barrier). The subsequent dehydrogenation of methylene is downhill by 0.53 eV, as the formation of methyldyne and the migration of the CH species to a three-fold hollow site has a stabilizing effect on the binding energy. Removing the final hydrogen to reach atomic carbon is both the most endothermic and highest barrier step. The addition of Sn makes each elementary reaction in this pathway more endothermic, and increases the activation energy barrier of each reaction. The effect is monotonic with Sn content – the greater the tin content in the alloy the greater the reaction endothermicity and activation energy barrier for each individual step. On Pt(111) the total reaction energy from

methane to atomic carbon is 0.28 eV while on PtSn/Pt it is tenfold larger at 2.82 eV. The highest barrier to fully dehydrogenate methane to atomic carbon is 1.07 eV on Pt(111) and 3.44 eV on PtSn/Pt. The C-H cleavage of methylene to methylidyne, -0.54 eV on Pt(111), becomes less exothermic (-0.23 eV) on the low-Sn Pt₃Sn/Pt alloy, and becomes endothermic (+0.55 eV) on the high-Sn PtSn/Pt alloy.

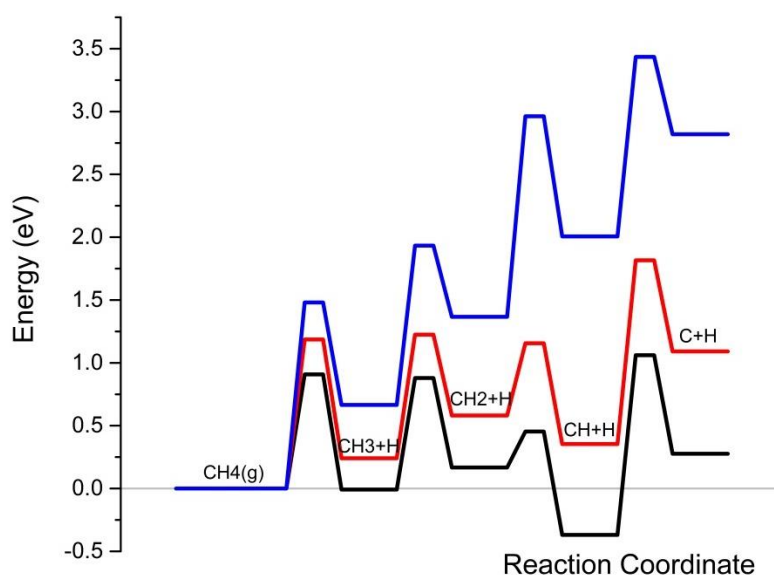


Figure 2.2: Two-dimensional potential energy surfaces for successive dehydrogenation of CH_x species beginning with CH_{4(g)} on Pt(111) and Pt/Sn alloys. Ordinate is energy relative to CH₄ in the gas phase. Gaseous species are indicated; all others are adsorbed on the metal surface. All species are at infinite separation. Hydrogen atoms remain on surface at infinite separation, and are omitted from labels for clarity. Potential energy surface on Pt(111) shown in **black**, on Pt₃Sn/Pt shown in **red**, and on PtSn/Pt shown in **blue**.⁰⁻²

As was seen with the best binding geometries, the reaction pathways for the dehydrogenation steps on the Pt(111) and Pt₃Sn/Pt surfaces are geometrically equivalent. The initial and final state structures for each elementary step (Table A.1) for these two surfaces are very similar. Once again, as the three-fold hollows of Pt atoms are preserved, this is reasonable. Perhaps more remarkable is that this is also true for the transition state structures. For each of the elementary reaction transition state structures on these two surfaces, the metal-carbon and carbon-hydrogen bond lengths are nearly the same.

Taking the dehydrogenation of methylidyne as an example, methylidyne starts in a three-fold hollow consisting of only Pt atoms. The C-H bond scission begins with the hydrogen approaching the top site of an adjacent Pt atom where the bond is cleaved, followed by diffusion of the free hydrogen atom away from the carbon. The similar mechanisms imply the increase in the dehydrogenation activation energy barrier is due to the indirect electronic effects of the neighboring Sn atom only.

With the elimination of three-fold hollow sites consisting only of Pt atoms on the PtSn/Pt surface, the pathways for the dehydrogenation steps differ from the pure Pt and low Sn surfaces, both energetically and geometrically. Once again using methylidyne as an example, the initial state is no longer geometrically equivalent. On the PtSn/Pt surface, methylidyne initially adsorbs to a three-fold hollow site consisting of two Pt atoms and one Sn atom. The C-H bond scission proceeds via elongation of the C-H bond over the top site of a Pt atom, but the surface rearranges such that the carbon atom occupies a bridge site between two Pt atoms, including the Pt atom over which the bond is breaking. This is in sharp contrast to the Pt(111) and low Sn-coverage surfaces, where the carbon atom is more closely associated with the two Pt atoms not directly participating in the C-H bond cleavage. The transition state on the high-Sn coverage surface only directly involves Pt atoms, just as with the other surfaces. However, only two Pt atoms are available to bind carbon and break the C-H bond, unlike the other surfaces. The final state for this elementary step also differs, in that the best binding site for the coadsorbed H atom is atop a Sn atom as all the Pt atoms are bonded to carbon in the CH species.

Table 2.4 Activation energy and heat of reaction for all elementary steps. All species are surface species except for gaseous species as noted.0-4

	Reaction	Pt(111)			Pt ₃ Sn/Pt(111)			PtSn/Pt(111)		
		E_a	ΔE	∞ FS	E_a	ΔE	∞ FS	E_a	ΔE	∞ FS
1	$\text{H}_{2(\text{g})} + 2^* \rightarrow 2\text{H}^*$	0.05	-0.86	-0.94	0.15	-0.76	-0.87	0.38	-0.38	-0.31
2	$\text{CH}_{4(\text{g})} + 2^* \rightarrow \text{CH}_3^* + \text{H}^*$	0.91	0.12	0.03	1.19	0.42	0.28	1.48	0.49	0.63
3	$\text{CH}_3^* + ^* \rightarrow \text{CH}_2^* + \text{H}^*$	0.89	0.35	0.18	0.98	0.45	0.34	1.27	0.96	0.70
4	$\text{CH}_2^* + ^* \rightarrow \text{CH}^* + \text{H}^*$	0.29	-0.35	-0.54	0.58	0.07	-0.23	1.60	0.74	0.64
5	$\text{CH}^* + ^* \rightarrow \text{C}^* + \text{H}^*$	1.43	0.86	0.64	1.46	1.08	0.74	1.43	1.13	0.81
6	$\text{CH}_3\text{CH}_{3(\text{g})} + 2^* \rightarrow \text{CH}_3\text{CH}_2^* + \text{H}^*$	0.91	0.13	0.02	1.19	0.40	0.28	1.58	0.59	0.71
7	$\text{CH}_3\text{CH}_2^* + ^* \rightarrow \text{CH}_3\text{CH}^* + \text{H}^*$	0.91	0.27	0.11	1.04	0.38	0.27	1.28	0.84	0.69
8	$\text{CH}_3\text{CH}_2^* + ^* \rightarrow \text{CH}_2\text{CH}_2^* + \text{H}^*$	0.89	0.06	-0.16	1.07	0.15	0.01	1.28	0.66	0.36
9	$\text{CH}_3\text{CH}^* + ^* \rightarrow \text{CH}_3\text{C}^* + \text{H}^*$	0.24	-0.55	-0.74	0.49	-0.20	-0.36	1.53	0.73	0.63
10	$\text{CH}_3\text{CH}^* + ^* \rightarrow \text{CH}_2\text{CH}^* + \text{H}^*$	0.82	0.06	-0.14	0.94	0.19	0.00	1.23	0.52	0.52
11	$\text{CH}_3\text{C}^* + ^* \rightarrow \text{CH}_2\text{C}^* + \text{H}^*$	1.42	0.65	0.41	1.33	0.81	0.34	^a 1.77	^a 0.74	^a 0.74
12	$\text{CH}_2\text{CH}_2^* + ^* \rightarrow \text{CH}_2\text{CH}^* + \text{H}^*$	0.90	0.32	0.13	1.01	0.45	0.26	1.48	0.85	0.85
13	$\text{CH}_2\text{CH}^* + ^* \rightarrow \text{CH}_2\text{C}^* + \text{H}^*$	0.68	0.05	-0.19	0.82	0.45	-0.01	1.23	0.68	0.52
14	$\text{CH}_2\text{CH}^* + ^* \rightarrow \text{CHCH}^* + \text{H}^*$	1.04	0.38	0.00	1.12	0.49	0.16	1.35	0.88	0.42
15	$\text{CH}_2\text{C}^* + ^* \rightarrow \text{CHC}^* + \text{H}^*$	1.67	1.43	1.10	2.00	1.43	1.13	1.47	1.03	0.96
16	$\text{CHCH}^* + ^* \rightarrow \text{CHC}^* + \text{H}^*$	1.68	1.24	0.91	1.79	1.25	0.95	1.96	1.14	1.07
17	$\text{C}_2\text{H}^* + ^* \rightarrow \text{C}_2^* + \text{H}^*$	1.69	1.15	0.98	1.88	1.53	1.12	1.56	0.99	0.33
18	$\text{CH}_3\text{CH}_{3(\text{g})} + 2^* \rightarrow \text{CH}_3^* + \text{CH}_3^*$	3.26	0.73	0.19	2.82	1.06	0.62	2.45	1.19	0.95
19	$\text{CH}_3\text{CH}_2^* + ^* \rightarrow \text{CH}_3^* + \text{CH}_2^*$	1.89	0.80	0.35	1.98	1.07	0.69	2.30	0.95	0.91
20	$\text{CH}_3\text{CH}^* + ^* \rightarrow \text{CH}_3^* + \text{CH}^*$	1.48	0.08	-0.29	1.51	0.46	0.19	2.40	0.39	0.87
21	$\text{CH}_3\text{C}^* + ^* \rightarrow \text{CH}_3^* + \text{C}^*$	2.21	1.41	1.10	2.23	1.30	1.29	2.10	0.76	1.04
22	$\text{CH}_2\text{CH}_2^* + ^* \rightarrow \text{CH}_2^* + \text{CH}_2^*$	2.24	1.24	0.69	2.10	1.20	1.02	1.93	1.43	1.23
23	$\text{CH}_2\text{CH}^* + ^* \rightarrow \text{CH}_2^* + \text{CH}^*$	1.70	0.70	0.03	2.15	0.76	0.53	1.72	1.54	1.02
24	$\text{CH}_2\text{C}^* + ^* \rightarrow \text{CH}_2^* + \text{C}^*$	2.89	1.34	0.87	2.22	1.52	1.28	1.96	1.90	1.31
25	$\text{CHCH}^* + ^* \rightarrow \text{CH}^* + \text{CH}^*$	1.36	0.27	-0.50	2.47	0.73	0.14	3.09	1.58	1.24
26	$\text{CHC}^* + ^* \rightarrow \text{CH}^* + \text{C}^*$	1.23	0.30	-0.77	1.84	0.91	-0.08	3.77	2.26	0.99
27	$\text{C}_2^* + ^* \rightarrow \text{C}^* + \text{C}^*$	1.23	0.32	-1.10	1.60	0.99	-0.46	3.42	3.03	1.47
28	$\text{CH}_3\text{CH}^* \rightarrow \text{CH}_2\text{CH}_2^*$	2.00	-0.26	-0.26	2.09	-0.26	-0.26	2.21	-0.33	-0.33

* following a surface species indicates a species bound to the surface, by itself denotes an empty adsorption site

E_a is the activation energy barrier in eV. ΔE is the energy of reaction in eV. ∞ FS is the energy of reaction at infinite separation in eV.

^a Not an elementary step. Reaction proceeds via isomerization of ethylidyne to vinyl followed by dehydrogenation of vinyl to vinylidene. Values given are net of both steps. Isomerization barrier is the higher of the two and is the reported barrier.

Using the values in Table 2.4, the contributions of the purely electronic effect of Sn in Pt₃Sn/Pt(111) to raising reaction energy barriers and increasing the endothermicity of the elementary reaction can be compared to the electronic and geometric effects found in the PtSn/Pt(111) alloy. For most C-H bond breaking steps, the increase in reaction energy was greater than the increase in activation energy for each addition of Sn to the

alloy surface. Additionally, these increases were greater for the increase in Sn loading between the low-Sn and high-Sn alloys, and smaller between the pure Pt and low-Sn alloy surfaces. This suggests that the geometric perturbation of surface binding sites has a larger impact on the thermodynamics and barriers for these dehydrogenation steps as compared to the purely electronic effect of the Sn atoms on their neighboring Pt atoms.

2.3.4 Binding of C_2H_x species

The binding site preferences and binding energies of the C_2H_x species ($x = 0$ to 6) on the Pt and alloy surfaces are given in Table 2.5, and the structures are depicted in Figure 2.3. The binding geometries and C-C bond lengths for the best binding sites for these species are generally consistent with sp^3 -hybridized carbon, with both carbons in the adsorbates centered in tetrahedral binding geometries with four bonds (C-H, C-Pt, or C-Sn), just as seen with the CH_x species. In all cases, Sn weakens the binding energy as compared to binding on pure Pt(111), with a more pronounced effect at higher Sn content. Closed-shell species such as ethene and acetylene bind to all alloy surfaces more weakly than the molecular fragment radicals, and the binding energies of all species generally increase with the number of carbon-metal bonds, as seen previously with CH_x species.

In most C_2H_x adsorbates, both carbons are unsaturated in hydrogen atoms and therefore bind to surface metals atoms, occupying two neighboring binding sites. In CH_3CH_x species, one of the carbons is saturated and does not interact with the surface, and so binding modes are similar to those seen for CH_x species, with the $-CH_3$ group replacing $-H$. For example, ethyl (CH_3CH_2) preferentially binds to top sites and displays minimal preference between binding to top sites over Pt and over Sn (<0.01 eV

difference on the PtSn/Pt alloy). Ethene forms a di- σ bond with two top sites atop Pt atoms, regardless of Sn loading, with tetrahedral geometry around each carbon, consistent with sp^3 hybridization. Ethylidyne adsorbs to a three-fold hollow site even when this forces a C-Sn bond to form on PtSn/Pt, just as seen with methylidyne. Vinyl has a unique binding geometry as the -CH end of the molecule binds to a bridge site on Pt(111) and Pt₃Sn/Pt surfaces, while the -CH₂ end of the molecule binds to a Pt top site. The adsorbate thus occupies a three-fold hollow of three Pt atoms, with both carbons sp^3 hybridized. With no such sites available on the PtSn/Pt surface, vinyl takes on a very different binding geometry. The -CH end of the molecule binds to a top site atop Pt and takes on a perpendicular-tilted orientation to the surface plane of the slab. In this orientation, the -CH₂ end of the molecule does not interact with the surface, and both carbons display sp^2 -hybridization and planar geometry. This suggests that the energetic penalty for sp^2 -hybridization is less than that for forming C-Sn bonds. Vinylidene takes on a similar orientation and hybridization as vinyl. On the surfaces of Pt and Pt₃Sn/Pt, vinylidene binds to three-fold hollows through the -C end of the molecule while the -CH₂ group binds to an adjacent top site. On PtSn/Pt, vinylidene takes a perpendicular orientation with the -C group binding to a site bridging two Pt atoms and with the -CH₂ group pointing away from the surface. Once again, a carbon-carbon double bond with sp^2 hybridization is favored over binding to Sn. When three-fold hollow sites of only Pt atoms are available, acetylene attaches to two adjacent bridge sites surrounding a three-fold hollow site of Pt atoms, approximating a tetrahedral geometry around each carbon atom. For the PtSn/Pt surface, acetylene binds to two adjacent top sites with a double bond between the carbon atoms and planar geometry. Acetylidyne is a species that

displays geometric changes between the Pt and Pt₃Sn/Pt surfaces. On Pt(111), the –C of acetylidene rests in a three-fold hollow site of Pt atoms with the –CH on an adjacent bridge site. On the Pt₃Sn/Pt surface, the –C of acetyildene again rests in a three-fold hollow site of Pt atoms but with the –CH binding to a top site. The site preference between these two geometries is only 0.06 eV on the Pt(111) surface, and given the small difference in site preference between these sites, the orientation that places a larger C-Sn distance is slightly favored energetically on the low-Sn alloy. On the high-Sn alloy, acetylidene takes the same geometry as adsorbed acetylene with both carbon atoms atop Pt atoms.

Table 2.5 Binding energies of C₂H_x species on Pt and PtSn alloys **0-5**

Adsorbate		Pt		Pt ₃ Sn/Pt			PtSn/Pt		
		Site	BE	Site	BE	CN _{Sn}	Site	BE	CN _{Sn}
CH ₃ CH ₃	Ethane	*	-0.07	*	-0.06	0	*	-0.06	0
CH ₃ CH ₂	Ethyl	Top	-1.89	Top	-1.65	0	Top	-1.50	1
CH ₃ CH	Ethylidene	Brg	-3.85	Brg	-3.48	0	Brg	-3.20	0
CH ₃ C	Ethylidyne	Fcc	-5.92	Fcc	-5.20	0	Fcc	-4.21	1
CH ₂ CH ₂	Ethene	Top-top	-1.01	Top-top	-0.64	0	Top-top	-0.42	0
CH ₂ CH	Vinyl	Brg-top	-3.10	Brg-top	-2.63	0	Top	-2.10	0
CH ₂ C	Vinylidene	Fcc-top	-4.35	Fcc-top	-3.72	0	Brg	-2.95	0
CHCH	Acetylene	Brg-brg	-2.19	Brg-brg	-1.58	0	Top-top	-1.09	0
C ₂ H	Acetylidene	Fcc-brg	-4.54	Fcc-top	-3.92	0	Brg-top	-3.60	0
C ₂	Dicarbon	Fcc-hcp	-5.94	Fcc-hcp	-5.20	1	^a Fcc	-5.96	1

BE is the binding energy in eV. **CN_{Sn}** is the coordination numbers of the adsorbate to Sn at the binding site.

*C₂H₆ physisorbs weakly with no site preferences.

^a Dicarbon enlarges the fcc site through the displacement of the Sn atom, 2.4 Å up from the surface and 1.7 Å in the lateral direction away from the dicarbon

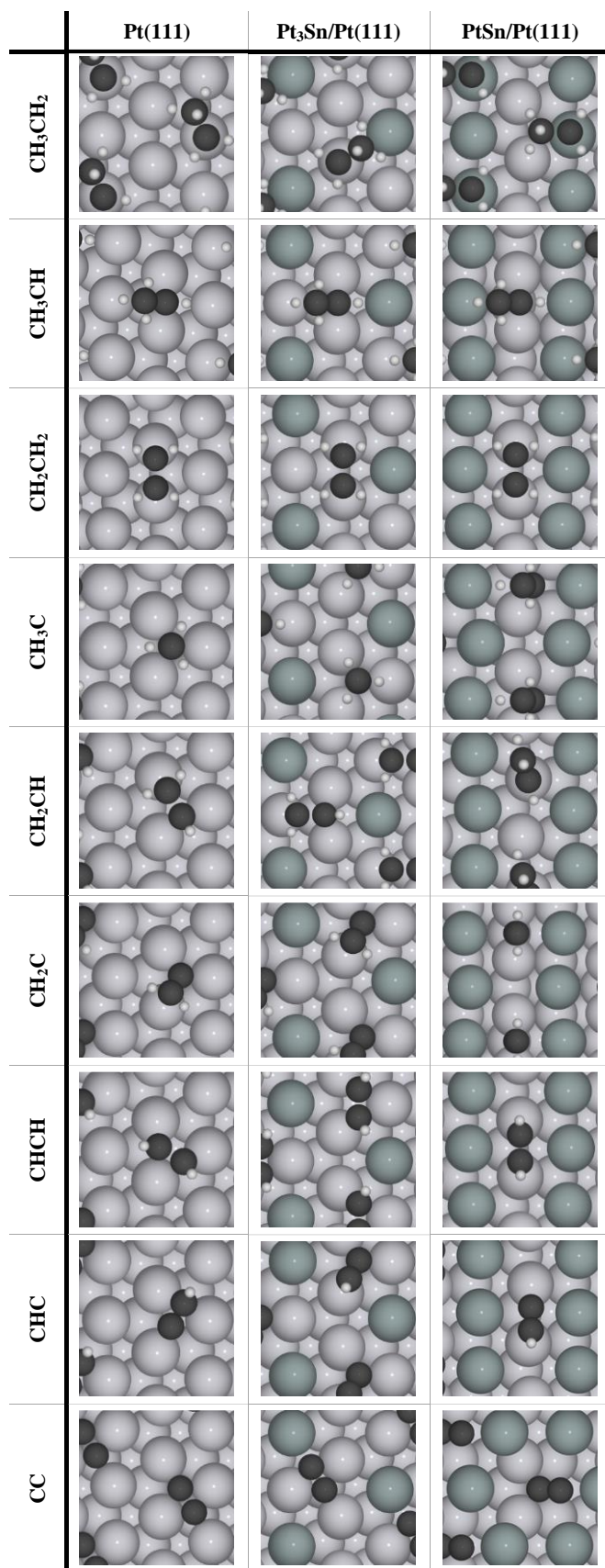


Figure 2.3: Best binding geometries of H and CH_x species on Pt and alloy surfaces.0-3

The binding energy of dicarbon on the PtSn/Pt alloy is stronger than expected, as the binding energies of all other species were calculated to be weaker on the PtSn/Pt alloy than on the Pt₃Sn alloy, except for dicarbon, which has a stronger binding energy on the higher tin alloy. This discrepancy arises due to the species displacing a Sn atom and partly binding to the subsurface Pt layer rather than solely to the surface layer. The large displacement of the Sn atom is not seen with other adsorbates, and may be an artifact of adjacent images interacting across the periodic boundary conditions used in these calculations. The next-best binding geometry, in which dicarbon binds to the surface layer of PtSn/Pt in a similar geometry as

on Pt₃Pt/Pt, is 0.70 eV weaker in binding energy, and is also weaker than the binding energy on the lower-Sn alloy, consistent with the trends seen for the other adsorbates.

2.3.5 Hydrogen coadsorption with C_xH_y species

Experimental studies have indicated that catalyst deactivation during alkane dehydrogenation can be reduced by adding H₂ gas to the feed stream.^{34,71,72} To investigate the source of this effect, the binding energies of hydrogen atoms coadsorbed with the C_xH_y species were calculated (Table 2.6). Typically, hydrocarbon adsorbates did not change their preferred binding geometries in the presence of coadsorbed hydrogen.

Hydrogen coadsorption had minimal impact on C_xH_y binding geometries. The exceptions were acetylidene and ethene on PtSn/Pt. Acetylidene has numerous binding geometries on all observed surfaces that are similar in binding energy (a total of 12 orientations ± 0.12 eV on all surfaces), so the slight perturbation of nearby spectator hydrogen atoms causes some of these structures to be destabilized relative to others, resulting in apparently different best binding geometries, with similarly weak preferences in the presence of a hydrogen atom (± 0.12 eV).

Table 2.6 Binding energies (in eV) of C₂H_x species in the presence of a hydrogen observer: $BE = E_{\text{slab}}(\text{H} + \text{C}_x\text{H}_y) - E_{\text{slab}}(\text{H}) - E_{\text{C}_x\text{H}_y}$ **0-6**

Surface	Pt(111)	Pt ₃ Sn	PtSn
CH ₃ CH ₂ +H	-1.77	-1.52	-1.62
CH ₃ CH+H	-3.69	-3.37	-3.05
CH ₃ C+H	-5.73	-5.04	-4.12
CH ₂ CH ₂ +H	-0.79	-0.5	-0.12
CH ₂ CH+H	-2.91	-2.43	-2.11
CH ₂ C+H	-4.1	-3.26	-2.79
CHCH+H	-1.81	-1.25	-0.63
C ₂ H+H	-4.21	-3.62	-3.53
C ₂ +H	-5.76	-4.78	-5.29

For coadsorption with C_xH_y species, hydrogen binds to an empty site several angstroms away from the carbon species. It has a fairly strict binding priority depending on available sites: beginning with a three-fold Pt site as the most stable, Pt top, Pt bridge, and finally with Sn top as the least stable. The binding energy difference between Pt adsorption locations is relatively small (<0.06 eV) while the Sn top location is significantly more unfavorable at 0.59 eV uphill on PtSn/Pt above the top site of a Pt atom.

Noteworthy is the case of hydrogen coadsorption with ethene on PtSn/Pt. Ethene has a weak binding energy, even on Pt(111), which is further decreased by the presence of Sn. The weak binding of ethene, a closed-shell molecular species, makes desorption relatively facile. Both hydrogen and ethene prefer binding to Pt top sites on PtSn/Pt. Coadsorbing ethene and hydrogen at $\frac{1}{4}$ ML coverage on the (2×2) surface unit cell used in these calculations leads to competition between the two adsorbate species for the preferred binding sites atop Pt atoms. Because hydrogen's binding energy at a Pt top site is twice as strong as that of ethene while requiring half as many adsorbate-Pt bonds, H outcompetes with ethene, and ethene is forced to desorb from the surface rather than bind to Sn atoms. Together with the experimental observations that have been reported, this suggests that hydrogen atoms compete with ethene for binding sites, and thereby promote desorption of the desired ethene product. This in turn improves the selectivity of the reaction by decreasing the rate of subsequent dehydrogenation of ethene and therefore the quantity of coke formed, which also reduces catalyst deactivation.

2.3.6 C-H bond-breaking steps in C_2H_x species and ethene formation

The stepwise dehydrogenation of ethane to diatomic carbon increases in activation energy barrier and endothermicity with increasing Sn content as seen in the potential energy surfaces in Figure 2.4. There are several different dehydrogenation pathways, which branch whenever a C-H bond may be cleaved on either end of an asymmetric C_2H_x adsorbate, and the paths intersect when C-H cleavage of different species leads to the same product. The three main pathways can be described by the key intermediates that distinguish them, and are the ethene/vinyl/vinylidene pathway, the ethylidene/ethylidyne/vinylidene pathway, and the ethylidene/vinyl/acetylene pathway. The reaction energies and barriers for all C-H bond-breaking steps are given in Table 2.4, and the transition state structures are given in Tables A.2-A.4.

On Pt(111), several C-H bond cleavage steps are nearly thermoneutral and several intermediates are nearly as stable as gas-phase ethane (with hydrogen atoms coadsorbed at infinite separation included in the product state energy). The activation energy barriers for most of the C-H bond cleavage steps are similarly close to one another (0.88 ± 0.20 eV). The most stable species, ethylidyne, is 0.68 eV below ethane gas, and represents the thermodynamic global minimum on the potential energy surface on Pt(111). Ethylidyne has high surface coordination making it highly stable when located at three-fold Pt sites. The reaction energy to form ethylidyne is consequently exothermic and the barrier is much smaller than the other dehydrogenation steps. The highly dehydrogenated products acetylide and diatomic carbon are significantly uphill in energy (>1 eV) and have high barriers for their formation (>1.5 eV). This is due to the lower extent of coordination (and therefore hybridization) in these products, making their formation highly unfavorable.

Based on the potential energy surface in Figure 2.4a, the formation of gaseous ethene is unfavorable compared to the formation of more highly dehydrogenated species such as ethylidyne, which is also the thermodynamic minimum for the system and may therefore be expected to be the most abundant surface intermediate. Looking at the selectivity for adsorbed ethene species, the desorption energy of ethene (1.01 eV) is larger than the ethene dehydrogenation barrier (0.90 eV). Together, these point to pure Pt(111) being an unselective ethene formation catalyst, making coke formation more favorable.

The addition of a small amount of Sn in the Pt₃Sn/Pt alloy improves the predicted performance of the catalyst slightly. The general trends are very similar to Pt(111), except each step is slightly more endothermic with slightly higher activation energy barriers. These increases are due to electronic effects, as the geometries and structures of the reactants, intermediates, and transition states are largely unchanged relative to Pt(111). The higher endothermicity of the dehydrogenation steps shifts the global thermodynamic minimum to an earlier species in the reaction sequence – adsorbed ethane. Ethylidyne, due to its highly favorable binding to three-fold Pt sites on the Pt₃Sn/Pt alloy, occupies a local thermodynamic minimum and is more effectively stabilized than other dehydrogenated species. The activation barriers also increase compared to pure Pt (1.03 ± 0.21 eV). The increased dehydrogenation barriers favor the formation of gaseous ethene, as ethene desorption (0.64 eV) is now competitive with the barrier for ethene dehydrogenation (1.01 eV), though the transition state energy for ethylidyne formation from ethylidene is still comparable to ethene desorption (Figure 2.4b). The high thermodynamic stability of ethylidyne and the relatively low barrier to its

formation remain as challenges to obtaining high selectivity towards ethene at low Sn coverage.

As before, the elimination of three-fold hollow sites of Pt atoms has a large effect on the potential energy surface for ethane dehydrogenation (Figure 2.4c). At 50% Sn coverage in PtSn/Pt, the geometries of intermediates and transition states (Table A.4) differ significantly from lower (Table A.3) and zero Sn coverage (Table A.2). Every dehydrogenation step is significantly more difficult, being more energetically uphill and having a larger activation energy barrier (1.37 ± 0.21 eV). The greatest effect is the destabilization of ethylidyne, which rests at a highly distorted three-fold hollow with two short Pt-C bonds and one long Pt-Sn bond. This unfavorable geometry leads to the formation of ethylidyne becoming endothermic (+0.63 eV) only on the PtSn/Pt surface, while on Pt (-0.74 eV) and Pt₃Sn/Pt (-0.36 eV) the formation of ethylidyne was exothermic, and a large barrier for its formation (1.53 eV) on the PtSn/Pt surface. The destabilization of the ethylidyne intermediate causes the mechanism of ethylidyne dehydrogenation to differ significantly on PtSn/Pt as compared to the other surfaces. On PtSn/Pt, no direct pathway for ethylidyne dehydrogenation is feasible, so ethylidyne first isomerizes to vinyl, which then undergoes C-H bond cleavage (forming either vinylidene or acetylene). The large barrier for this isomerization reaction (1.77 eV) places the transition state higher in energy compared to those for the subsequent dehydrogenation steps, as noted in Table 2.4.

Nearly all dehydrogenation step barriers increase with increasing Sn content, except for vinylidene dehydrogenation, where the barrier increases upon the addition of some Sn, but decreases between the low-Sn and high-Sn alloys. The decrease in the

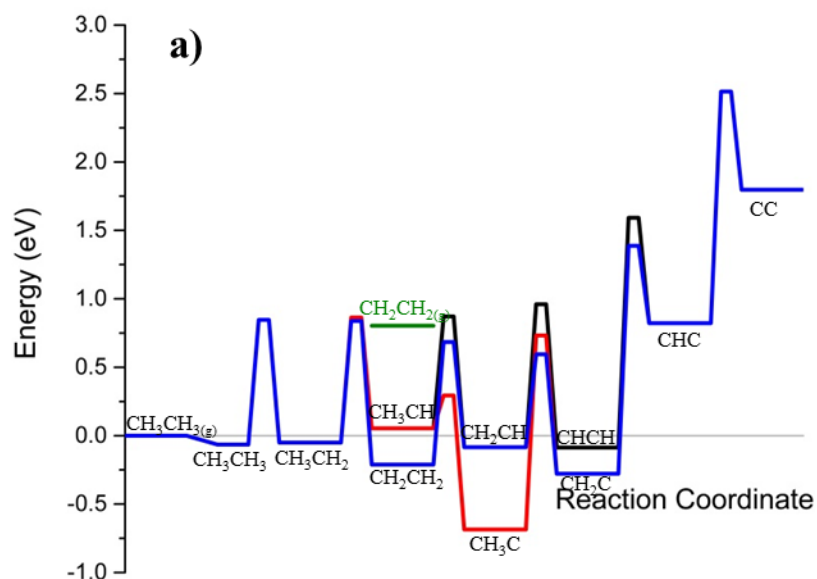
barrier at the higher Sn coverage arises due to the low-stability π bonded geometry that vinylidene is forced to take on the crowded high-Sn surface. On the lower Sn surfaces, the availability of three-fold Pt sites allows vinylidene to bind more strongly with only σ bonds, giving a more stable reactant state, and therefore a larger barrier.

The destabilization of ethynidyne and the more difficult C-H bond cleavage reactions favors the formation of the desirable ethene product on PtSn/Pt. Adsorbed ethane remains the global minimum on the potential energy surface, but now with a significant thermodynamic advantage, making it a good candidate for most abundant surface intermediate. The desorption of ethene is relatively facile (0.42 eV) compared to ethene dehydrogenation (1.48 eV), so the higher Sn content is predicted to improve ethene selectivity.

From the transition state geometries in Tables A.2-A.4, the similarity in the C-H bond cleavage mechanism in all C_xH_y species can be seen. Every C-H bond cleavage step for both CH_x and C_2H_x species, regardless of the surface, involves the leaving-hydrogen atom moving to a top site over an adjacent Pt atom in the transition state. This affinity for hydrogen atoms for top sites over Pt provides a stabilizing effect, effectively lowering the activation barrier for the dehydrogenation reaction. Due to less crowding around Pt coordination sites, the transition state structures for these steps on Pt(111) and Pt₃Sn/Pt exhibit further stabilization as compared to PtSn/Pt, where both daughter species of a C-H bond cleavage reaction occupy sites on the same Pt atom with short Pt-C bonds due to the smaller Pt atom ensembles.

It should be noted that both isomers formed from ethyl dehydrogenation are roughly equally likely to form, with no difference in kinetic ($\Delta E_a < 0.05$ eV) driving forces and little difference in thermodynamic driving forces ($\Delta \Delta E \sim 0.29$ eV) between the formation of ethene and ethylidene on any of the three surfaces studied here. Neither Pt nor its alloys are selective for the formation of ethylene over ethylidene.

Ethylidene dehydrogenation can also form two isomers: vinyl and ethylidyne. Ethylidyne, on Pt(111), is likely more prevalent than vinyl as the activation energy barrier for its formation is 0.57 eV lower and the reaction energy is 0.60 eV lower. Ethylidene dehydrogenation to ethylidyne also has a lower barrier on Pt₃Sn/Pt. However when there are no three-fold Pt sites on PtSn/Pt, ethylidyne formation is disrupted and ethylidene dehydrogenation to vinyl is favored. This preference is noteworthy as vinyl can undergo hydrogenation to ethene, while ethylidyne cannot.



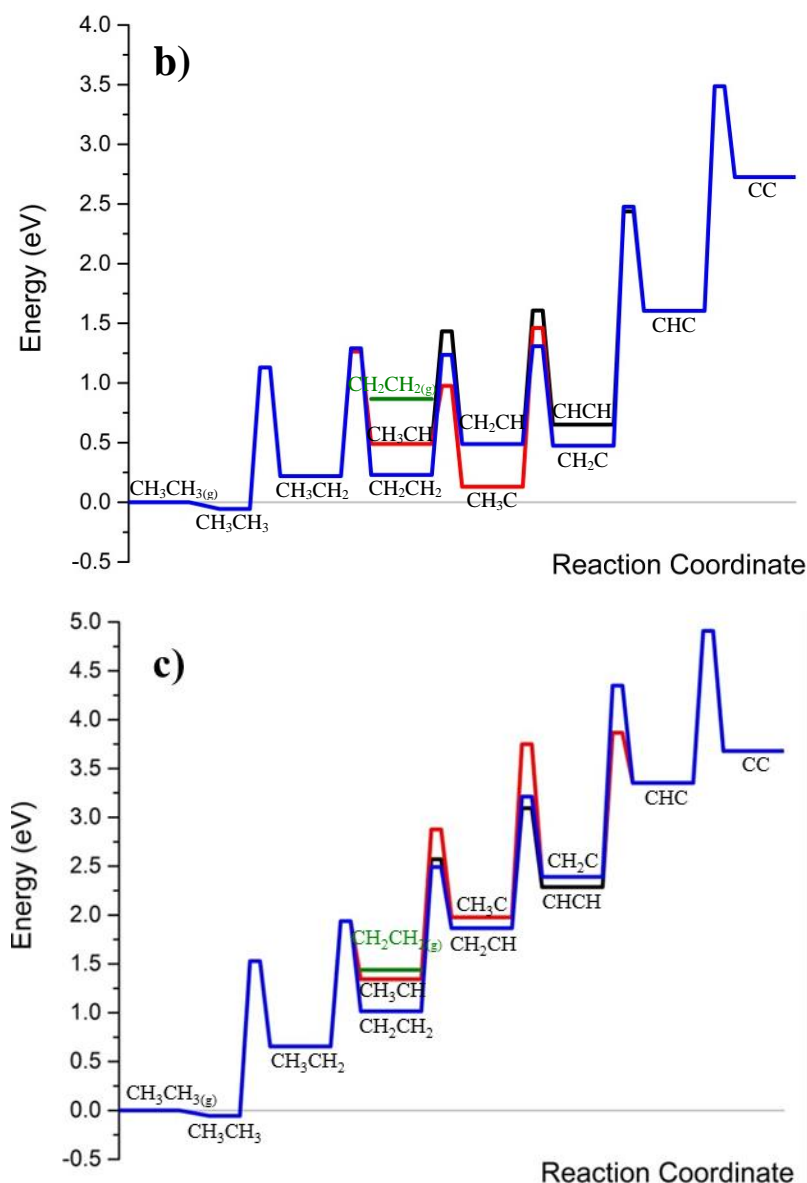


Figure 2.4: Two-dimensional potential energy surfaces for successive dehydrogenation of C_2H_x species beginning with $C_2H_6(g)$ on a) Pt(111), b) Pt₃Sn/Pt, and c) PtSn/Pt. Ordinate is energy relative to C_2H_6 in the gas phase. Gaseous species are indicated; all others are adsorbed on the metal surface. All species are at infinite separation. Hydrogen atoms remain on surface at infinite separation, and are omitted from labels for clarity. Ethene/vinyl/vinylidene pathway shown in blue, ethylidene/ethylidyne/vinylidene pathway shown in red, and ethylidene/vinyl/acetylene pathway shown in black.

Given the importance of isomerization in the dehydrogenation mechanism for ethylidyne on PtSn/Pt, the isomerization of other C_2H_x species was studied. The isomerization mechanism involved a hydride migration from one carbon to the other within a given surface intermediate. The barriers for these isomerization reactions were

calculated, but were found to be significantly larger than the C-H cleavage barriers in all cases. The only case where direct isomerization is likely to have any kinetic relevance is in the case of ethynidyne due to the elimination of a direct C-H cleavage pathway for this intermediate.

Direct isomerization can further be eliminated from consideration, as indirect isomerization has lower barriers in all cases. For example, the isomerization of ethynidyne to ethene has a higher activation energy barrier than most dehydrogenation steps on all surfaces explored in this study. A lower energy pathway to the same overall isomerization is the hydrogenation of ethynidyne, forming ethyl, followed by the subsequent dehydrogenation to ethene. The highest barrier in this multi-step pathway is 1.09 eV, 1.02 eV, and 0.93 eV for Pt(111), Pt₃Sn/Pt, and PtSn/Pt respectively. This is in contrast to the direct isomerization barriers of 2.00 eV, 2.09 eV, and 2.31 eV. As such, direct isomerization is not a predominant part of the ethene production pathway.

2.3.7 C-C bond-breaking steps in C₂H_x species

The reaction energies and activation barriers for C-C bond cleavage is considerably more varied in magnitudes and trends on Pt(111) and the Pt-Sn alloys than for the C-H bond cleavage reactions reported above (Table 2.4). The activation energy barriers to break C-C bonds (1.23 – 3.26 eV on Pt, up to 3.77 eV on the alloys) are significantly larger than those for C-H bonds. However, the trend with increasing Sn coverage depends on the specific reaction intermediate whose C-C bond is undergoing cleavage. For example, the barrier to break the C-C bond in adsorbed ethane is highest on Pt(111) (3.26 eV) and lowest on PtSn/Pt (2.45 eV), while C-C cleavage in ethyl follows the opposite trend – 1.89 eV on Pt(111) and 2.30 eV on PtSn/Pt. Still other species do not

follow monotonic trends, such as vinyl, where the barrier is largest for the Pt₃Sn/Pt surface. For acetylene and further dehydrogenated species (acetylidene and dicarbon) on Pt(111), C-C bond cleavage has a lower activate energy barrier than C-H bond cleavage.

The variation in C-C bond breaking energies is in part due to the influence of surface corrugation. When adsorbates and transition states interact with the metal atoms of the model surfaces used in this study, they may induce the movement of one or more metal atoms perpendicular to the metal surface. Atoms that move “upwards” in this way have less interaction with their neighbors, and greater interaction with the adsorbate or transition state to which they are bonded. No significant surface corrugation was observed on the Pt(111) surface in any of the reactions studied here, but the behavior was different for the alloys. In the presence of Sn atoms, the neighboring Pt atoms became more mobile and able to displace by up to 0.5 Å normal to the surface in the presence of C₂H_x adsorbates. These effectively lower-coordinate Pt atoms were involved in several C-C cleavage mechanisms (but played little or no role in C-H cleavage), especially in the transition state where the degree of corrugation is exaggerated. For example, the C-C cleavage in adsorbed ethane takes place over a Pt atom that is displaced vertically by 1.16 Å and 1.87 Å in the transition state on the Pt₃Sn/Pt and PtSn/Pt surfaces respectively, effectively reducing the barrier for breaking the C-C bond as compared to Pt(111) where the corrugation displacement of Pt was only 0.29 Å in the transition state. However, since these transition state energies were very high, the effect of Pt atom corrugation on these C-C bond cleavage reactions may be of little more than academic interest.

At high Sn coverage, both Pt atoms and Sn atoms were able to undergo significant vertical displacement, with Sn displacement apparently more prevalent in the calculations

performed in this study. The vertical displacement of Sn atoms, when observed, was always ~ 1.5 Å, regardless of the adsorbate inducing the surface corrugation. Binding energies for these species with corrugation were ~ 0.2 eV stronger than in the absence of significant Sn atom displacement. The Sn atom corrugation also served to stabilize the product of many C-C bond cleavage steps, as methyl groups showed equal preference to top sites over Pt and Sn atoms (Table 2.2). In C-C cleaving reactions that produced a methyl product, the reaction energies to coadsorbed products were lower on the PtSn/Pt alloy than on the lower-Sn alloy, while the reaction energies for reactions without methyl products were significantly larger. The effect is not observed when considering the species at infinite separation, which eliminates the effects of competition for optimal binding sites and repulsion between adsorbates. In these cases where a methyl group was coadsorbed at a top site over Sn, the Sn atoms displacement normal to the surface was ~ 1.5 Å.

2.3.8 Minimum energy pathway to atomic carbon

Without a priori information, atomic carbon seems a reasonable candidate as a coke precursor during high temperature alkane reactions under reducing conditions. One can imagine a combination of C-H and C-C cleavage steps that would lead to the formation of atomic carbon on a catalyst that would then oligomerize and aromatize to form graphitic coke. On the Pt and Pt-Sn alloy surfaces studied here, dicarbon was found to be very energetically unfavorable, such that it is unlikely to be a coke precursor via dehydrogenation of ethane.

To produce atomic carbon on Pt(111), the minimum energy pathway is to dehydrogenate ethane to acetylene (independent of which isomeric intermediate is used)

before breaking the C-C bond. The highest barrier in the pathway is 1.27 eV (relative to gaseous ethane) to cleave the acetylene C-C bond to form two methylidyne species. The subsequent C-H cleavage in methylidyne is lower in barrier than the C-C cleavage step. The overall process to atomic carbon is essentially thermo-neutral (+0.06 eV). With a low barrier and minimal required energy, atomic carbon is possibly found on Pt(111).

Due to the increased endothermicity for each C-H bond cleavage step on Pt₃Sn/Pt, the minimum energy pathway to atomic carbon cleaves the C-C bond earlier (fewer C-H bond-breaking steps before breaking the C-C bond). The preferred pathway cleaves the C-C bond in ethylidene, and the highest energy transition state in the pathway (final C-H cleavage in methylidyne) is 2.14 eV higher in energy than gaseous ethane. The net reaction energy is 1.42 eV uphill.

On PtSn/Pt, the pathway to carbon cleaves the C-C bond immediately in adsorbed ethane, followed by successive dehydrogenation steps. The highest barrier is once again to remove hydrogen from methylidyne to form atomic carbon, 3.61 eV higher than gas-phase ethane, with a net reaction energy of 3.00 eV, even at high alkane dehydrogenation temperatures.

On both alloys, the formation of atomic carbon is much less favorable than on pure Pt. On the higher Sn-content alloy, the energetics of atomic carbon formation have become so unfavorable that atomic carbon is not expected to be relevant to the pathway to forming coke.

In the experiments, the addition of Sn has been shown to significantly decrease coke formation, perhaps consistent with the elimination of atomic carbon formation

predicted in these calculations. However, the formation of coke is not eliminated on Pt-Sn alloys. This suggests that a different coke formation mechanism may operate on the alloys (possible also on pure Pt alongside or instead of an atomic carbon-based mechanism). The high formation energies and barriers to form dicarbon eliminate dicarbon as a viable intermediate as well, and acetylene has never been reported as a gas phase product, suggesting that the key coke precursors are less dehydrogenated species than acetylene. A possible mechanism for coke formation may involve the partial dehydrogenation of ethane to C_2H_x species, which themselves oligomerize and thereafter aromatize and dehydrogenate to yield the graphitic coke observed in experiment.

2.4 Conclusions

Density functional theory calculations have been performed to investigate the effect of alloying Pt with Sn on selectivity to ethene and coke during ethane dehydrogenation. The complete dehydrogenation pathway potential energy surface on Pt(111) was compared to Pt-Sn surface substitutional alloys with Sn coverage levels of $\frac{1}{4}$ and $\frac{1}{2}$ ML (Pt_3Sn/Pt and $PtSn/Pt$), including every C-H and C-C bond scission step. With the addition of $\frac{1}{4}$ ML Sn to the Pt surface, there was no disruption of three-fold Pt sites, so there was no change in preferred binding geometries and minimal changes to the reaction pathways. For the $\frac{1}{2}$ ML Sn loading, the elimination of these sites caused significant changes to the binding geometries, transition state structures, and elementary reaction step pathways.

Both alloy surfaces experienced an electron donating effect of Sn atoms to neighboring Pt atoms. This electronic modification decreased binding energies of adsorbates to Pt and increased the endothermicity and reaction barrier of each elementary

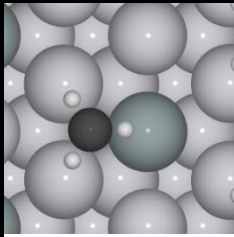
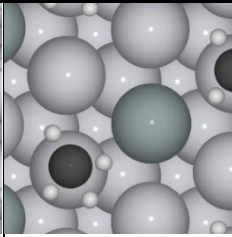
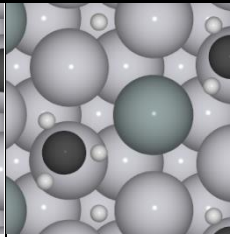
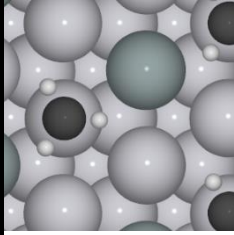
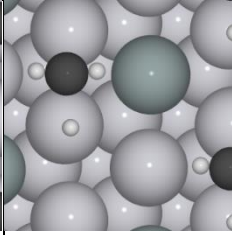
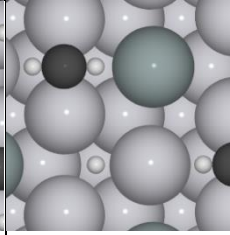
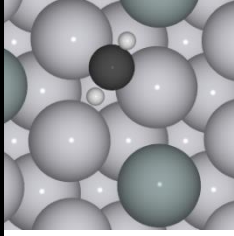
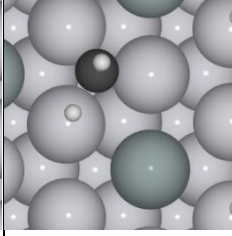
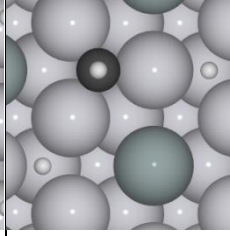
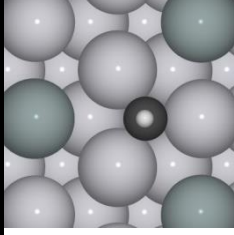
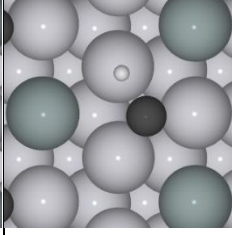
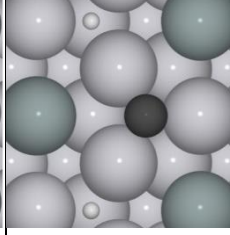
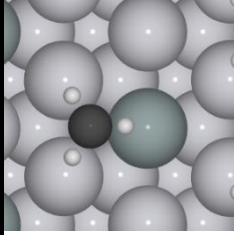
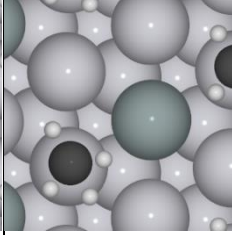
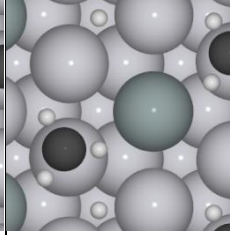
C-H and C-C bond breaking step. This increase favors ethene selectivity over unselective coke formation, as desorption of the product is more facile, and subsequent bond-cleavage reactions are more unfavorable.

The selectivity to the desired product ethylene and to coke (as atomic carbon) were compared on the basis of the net reaction energy and highest activation energy barrier (both relative to gaseous ethane) to each product on the three surfaces. On Pt(111), the reaction energy to form ethene is 0.80 eV and the highest barrier is 0.85 eV. The reaction energy to atomic carbon from ethane is 0.06 eV with a barrier of 1.06 eV. Poor selectivity to ethene over atomic carbon is expected on Pt(111), as is seen in experiments. On the Pt₃Sn/Pt surface, both reaction pathways are more endothermic (0.87 eV and 1.42 eV for ethene and carbon formation respectively) and have higher barriers (1.29 eV and 2.14 eV), but the impact is greater on the carbon pathway so that ethene formation is more favorable than on the pure Pt surface, increasing predicted selectivity on the alloy. On the highest Sn-loading PtSn surface, the formation of ethene further increases to 1.44 eV uphill with a 1.94 eV barrier, while the formation of carbon is severely thermodynamically and kinetically hindered (3.00 eV and 3.61 eV respectively). These results point to increasing selectivity towards ethene with increasing Sn loading as well as suggesting that the coke-forming mechanism switches from an atomic carbon-mediated mechanism to some other mechanism, as some coke formation is still observed experimentally over high Sn alloys.

2.A Supporting Information: Pictorial Mechanisms for C_xH_y dehydrogenation on Pt and PtSn alloys

Table A.1 Initial, final, and transition state structures for each elementary reaction step for dehydrogenation of CH_x species on Pt(111), Pt₃Sn/Pt, and PtSn/Pt.0-7

	Pt(111)		
Reaction	Reactant state	Transition state	Product state
$\text{CH}_4^* + * \rightarrow$ $\text{CH}_3^* + \text{H}^*$			
$\text{CH}_3^* + * \rightarrow$ $\text{CH}_2^* + \text{H}^*$			
$\text{CH}_2^* + * \rightarrow$ $\text{CH}^* + \text{H}^*$			
$\text{CH}^* + * \rightarrow$ $\text{C}^* + \text{H}^*$			
	Pt ₃ Sn/Pt(111)		
Reaction	Reactant state	Transition state	Product state

$\text{CH}_4^* + * \rightarrow$ $\text{CH}_3^* + \text{H}^*$			
$\text{CH}_3^* + * \rightarrow$ $\text{CH}_2^* + \text{H}^*$			
$\text{CH}_2^* + * \rightarrow$ $\text{CH}^* + \text{H}^*$			
$\text{CH}^* + * \rightarrow$ $\text{C}^* + \text{H}^*$			
	PtSn/Pt(111)		
Reaction	Reactant state	Transition state	Product state
$\text{CH}_4^* + * \rightarrow$ $\text{CH}_3^* + \text{H}^*$			

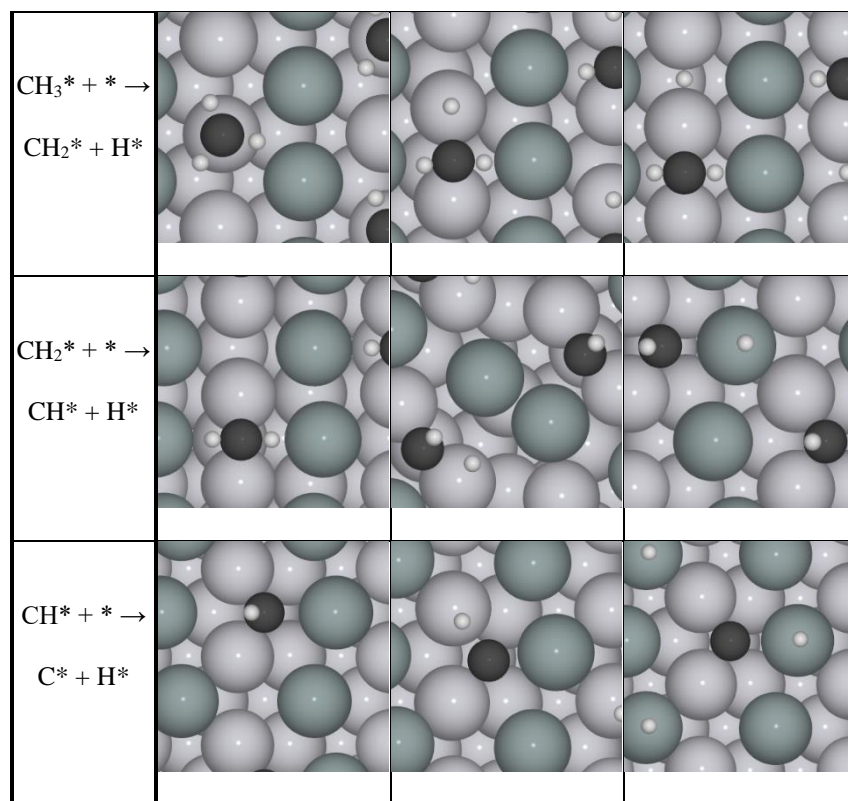
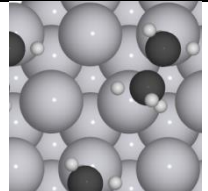
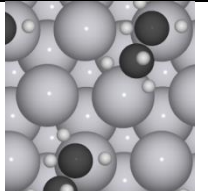
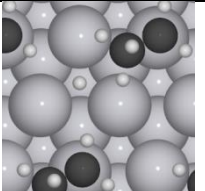
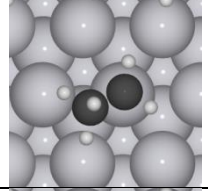
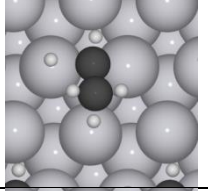
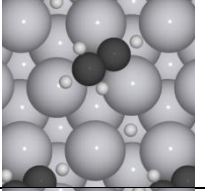
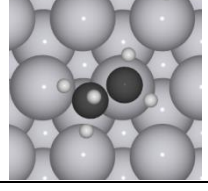
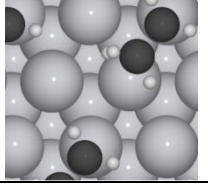
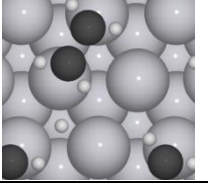
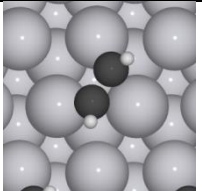
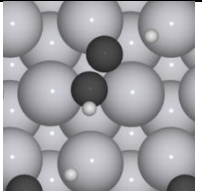
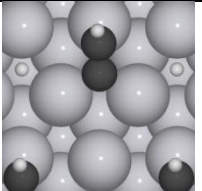
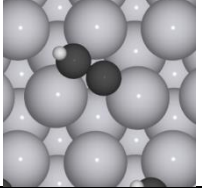
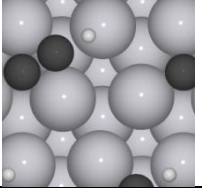
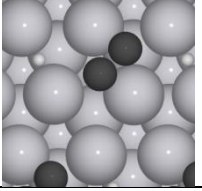
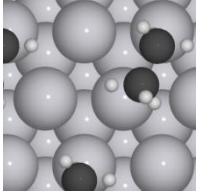
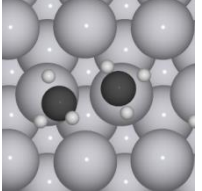
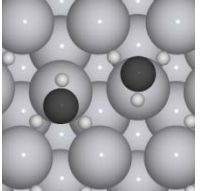
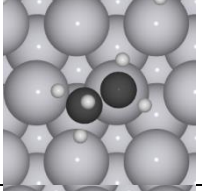
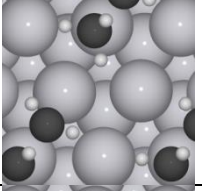
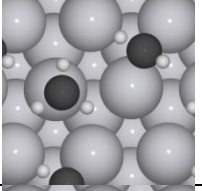
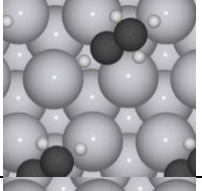
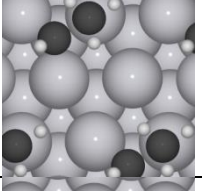
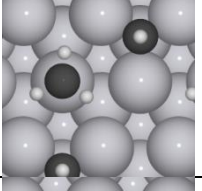
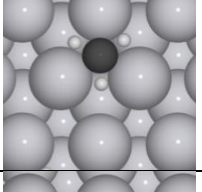
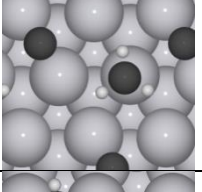
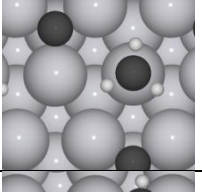
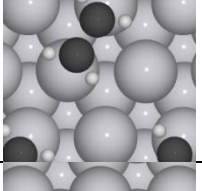
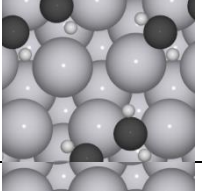
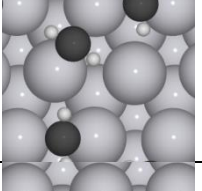
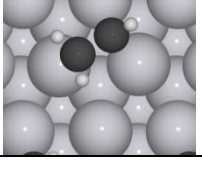
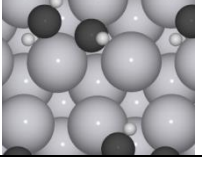
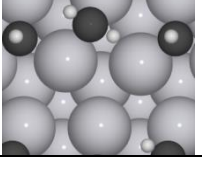


Table A.2 Initial, final, and transition state structures for each elementary reaction step for C_2H_x species on Pt(111).0-8

Dehydrogenation (reactant)	Reaction	Initial State	Transition State	Final State
Ethane	$\text{CH}_3\text{CH}_3^* + * \rightarrow$ $\text{CH}_3\text{CH}_2^* + \text{H}^*$			
Ethyl	$\text{CH}_3\text{CH}_2^* + * \rightarrow$ $\text{CH}_3\text{CH}^* + \text{H}^*$			
Ethyl	$\text{CH}_3\text{CH}_2^* + * \rightarrow$ $\text{CH}_2\text{CH}_2^* + \text{H}^*$			

Ethylidene	$\text{CH}_3\text{CH}^* + * \rightarrow \text{CH}_3\text{C}^* + \text{H}^*$	
Ethylidene	$\text{CH}_3\text{CH}^* + * \rightarrow \text{CH}_2\text{CH}^* + \text{H}^*$	
Ethylidene (isomerization)	$\text{CH}_3\text{CH}^* \rightarrow \text{CH}_2\text{CH}_2^*$	
Ethylidyne	$\text{CH}_3\text{C}^* + * \rightarrow \text{CH}_2\text{C}^* + \text{H}^*$	
Ethene	$\text{CH}_2\text{CH}_2^* + * \rightarrow \text{CH}_2\text{CH}^* + \text{H}^*$	
Vinyl	$\text{CH}_2\text{CH}^* + * \rightarrow \text{CH}_2\text{C}^* + \text{H}^*$	
Vinyl	$\text{CH}_2\text{CH}^* + * \rightarrow \text{CHCH}^* + \text{H}^*$	
Vinylidene	$\text{CH}_2\text{C}^* + * \rightarrow \text{CHC}^* + \text{H}^*$	

Acetylene	$\text{CHCH}^* + * \rightarrow \text{CHC}^* + \text{H}^*$			
Acetylidene	$\text{CHC}^* + * \rightarrow \text{C}_2^* + \text{H}^*$			
C-C Cleavage (reactant)	Reaction	Initial State	Transition State	Final State
Ethane	$\text{CH}_3\text{CH}_3^* + * \rightarrow \text{CH}_3^* + \text{CH}_3^*$			
Ethyl	$\text{CH}_3\text{CH}_2^* + * \rightarrow \text{CH}_3^* + \text{CH}_2^*$			
Ethylidene	$\text{CH}_3\text{CH}^* + * \rightarrow \text{CH}_3^* + \text{CH}^*$			
Ethylidyne	$\text{CH}_3\text{C}^* + * \rightarrow \text{CH}_3^* + \text{C}^*$			
Ethene	$\text{CH}_2\text{CH}_2^* + * \rightarrow \text{CH}_2^* + \text{CH}_2^*$			
Vinyl	$\text{CH}_2\text{CH}^* + * \rightarrow \text{CH}_2^* + \text{CH}^*$			

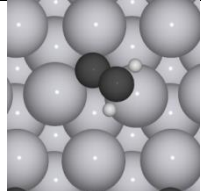
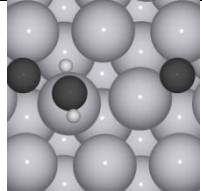
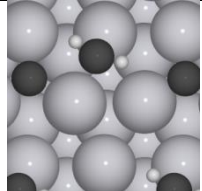
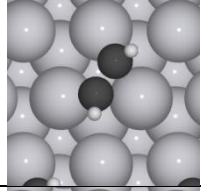
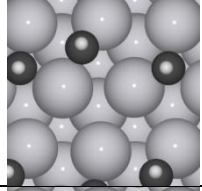
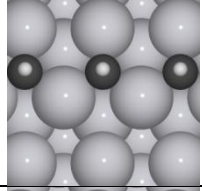
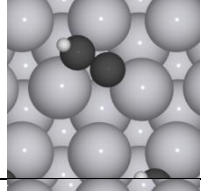
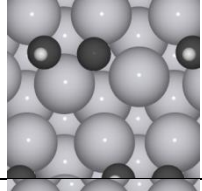
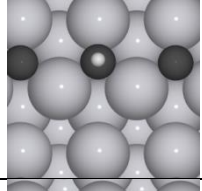
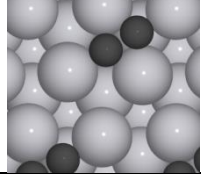
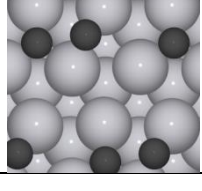
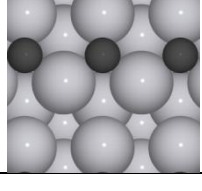
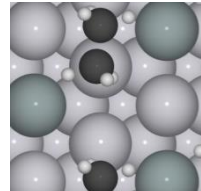
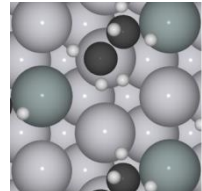
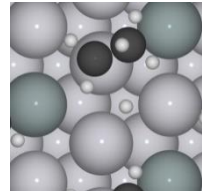
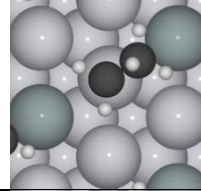
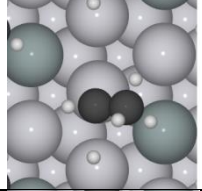
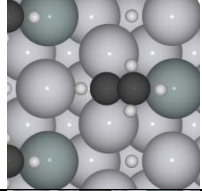
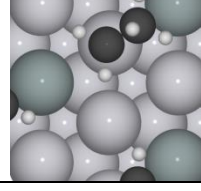
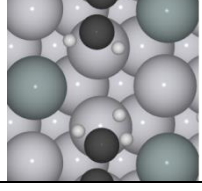
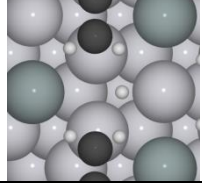
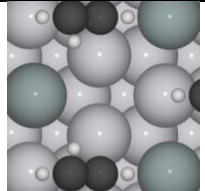
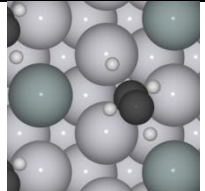
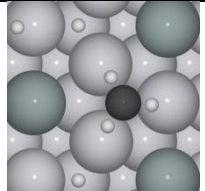
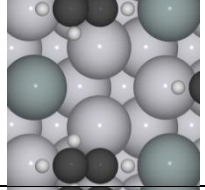
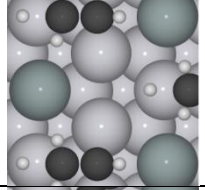
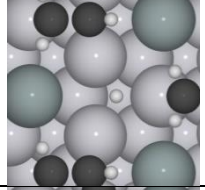
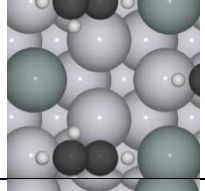
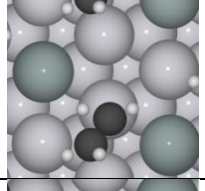
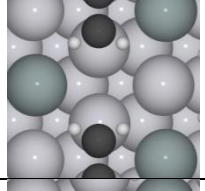
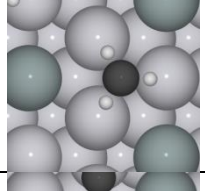
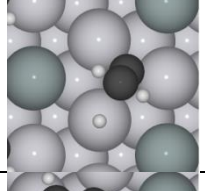
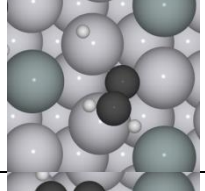
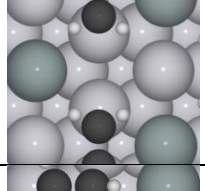
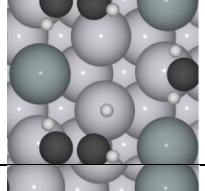
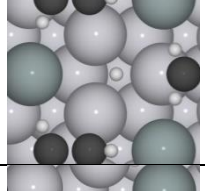
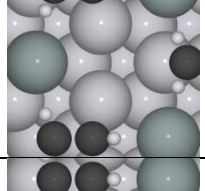
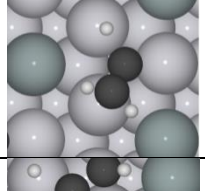
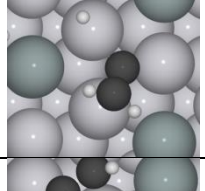
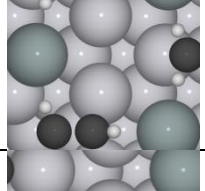
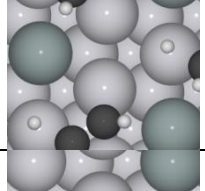
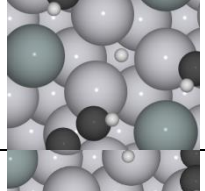
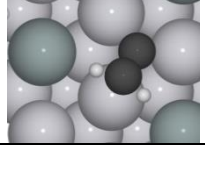
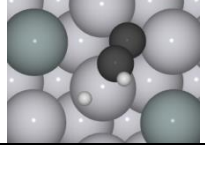
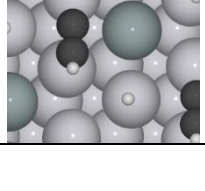
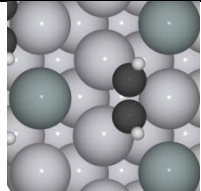
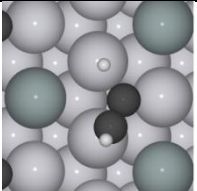
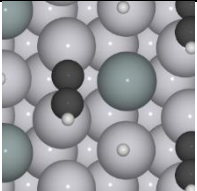
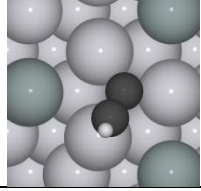
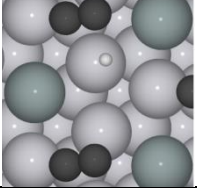
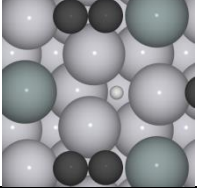
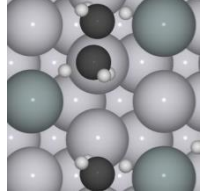
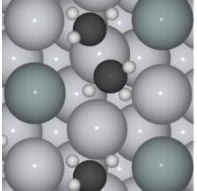
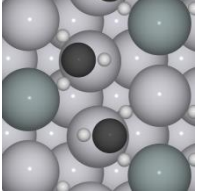
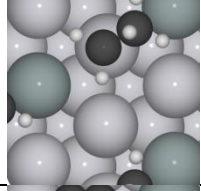
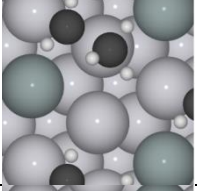
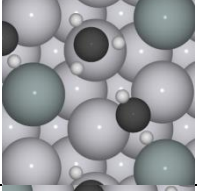
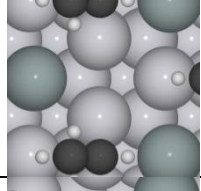
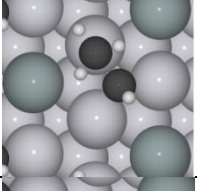
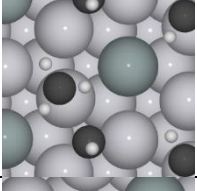
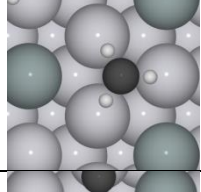
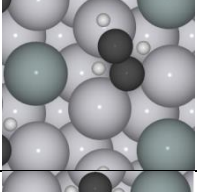
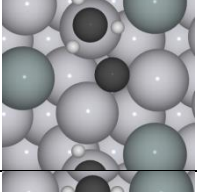
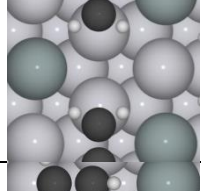
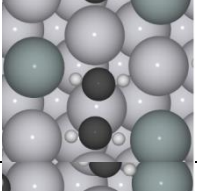
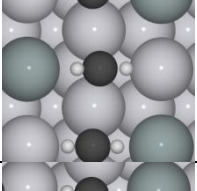
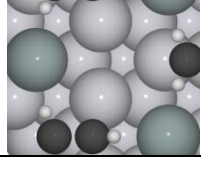
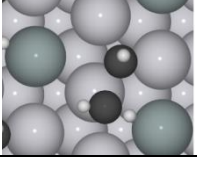
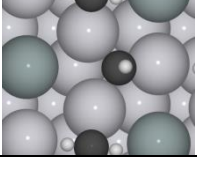
Vinylidene	$\text{CH}_2\text{C}^* + * \rightarrow \text{CH}_2^* + \text{C}^*$			
Acetylene	$\text{CHCH}^* + * \rightarrow \text{CH}^* + \text{CH}^*$			
Acetylidene	$\text{CHC}^* + * \rightarrow \text{CH}^* + \text{C}^*$			
Dicarbon	$\text{C}_2^* + * \rightarrow \text{C}^* + \text{C}^*$			

Table A.3 Initial, final, and transition state structures for each elementary reaction step for C_2H_x species on $\text{Pt}_3\text{Sn}/\text{Pt}$ 0-9

Dehydrogenation (reactant)	Reaction	Initial State	Transition State	Final State
Ethane	$\text{CH}_3\text{CH}_3^* + * \rightarrow \text{CH}_3\text{CH}_2^* + \text{H}^*$			
Ethyl	$\text{CH}_3\text{CH}_2^* + * \rightarrow \text{CH}_3\text{CH}^* + \text{H}^*$			
Ethyl	$\text{CH}_3\text{CH}_2^* + * \rightarrow \text{CH}_2\text{CH}_2^* + \text{H}^*$			

Ethylidene	$\text{CH}_3\text{CH}^* + * \rightarrow \text{CH}_3\text{C}^* + \text{H}^*$			
Ethylidene	$\text{CH}_3\text{CH}^* + * \rightarrow \text{CH}_2\text{CH}^* + \text{H}^*$			
Ethylidene (isomerization)	$\text{CH}_3\text{CH}^* \rightarrow \text{CH}_2\text{CH}_2^*$			
Ethylidyne	$\text{CH}_3\text{C}^* + * \rightarrow \text{CH}_2\text{C}^* + \text{H}^*$			
Ethene	$\text{CH}_2\text{CH}_2^* + * \rightarrow \text{CH}_2\text{CH}^* + \text{H}^*$			
Vinyl	$\text{CH}_2\text{CH}^* + * \rightarrow \text{CH}_2\text{C}^* + \text{H}^*$			
Vinyl	$\text{CH}_2\text{CH}^* + * \rightarrow \text{CHCH}^* + \text{H}^*$			
Vinylidene	$\text{CH}_2\text{C}^* + * \rightarrow \text{CHC}^* + \text{H}^*$			

Acetylene	$\text{CHCH}^* + * \rightarrow \text{CHC}^* + \text{H}^*$			
Acetylidene	$\text{CHC}^* + * \rightarrow \text{C}_2^* + \text{H}^*$			
C-C Cleavage (reactant)	Reaction	Initial State	Transition State	Final State
Ethane	$\text{CH}_3\text{CH}_3^* + * \rightarrow \text{CH}_3^* + \text{CH}_3^*$			
Ethyl	$\text{CH}_3\text{CH}_2^* + * \rightarrow \text{CH}_3^* + \text{CH}_2^*$			
Ethylidene	$\text{CH}_3\text{CH}^* + * \rightarrow \text{CH}_3^* + \text{CH}^*$			
Ethylidyne	$\text{CH}_3\text{C}^* + * \rightarrow \text{CH}_3^* + \text{C}^*$			
Ethene	$\text{CH}_2\text{CH}_2^* + * \rightarrow \text{CH}_2^* + \text{CH}_2^*$			
Vinyl	$\text{CH}_2\text{CH}^* + * \rightarrow \text{CH}_2^* + \text{CH}^*$			

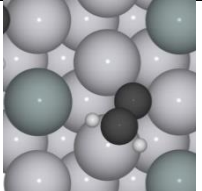
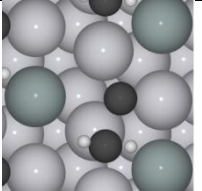
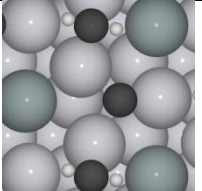
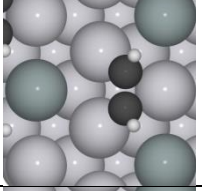
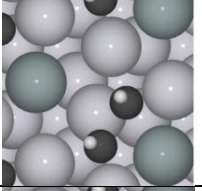
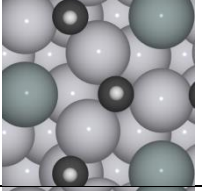
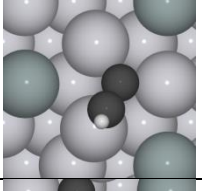
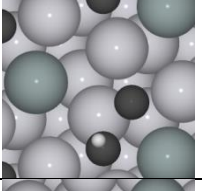
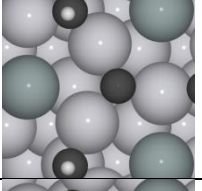
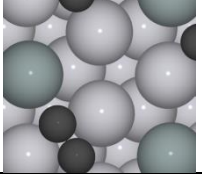
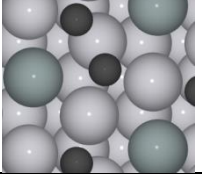
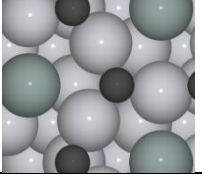
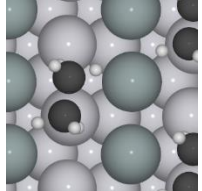
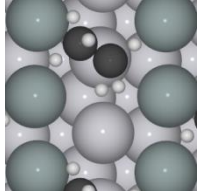
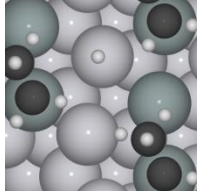
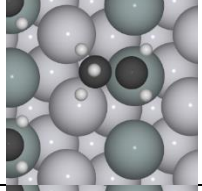
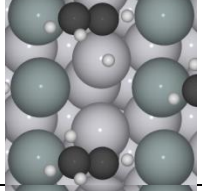
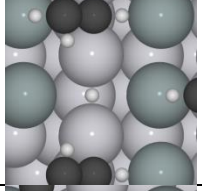
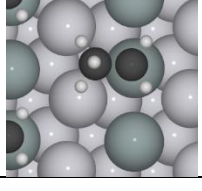
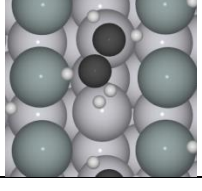
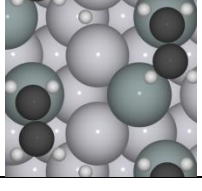
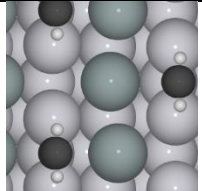
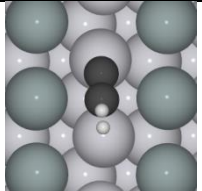
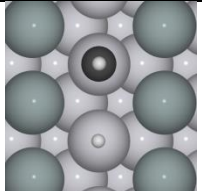
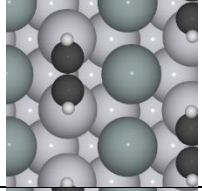
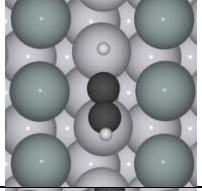
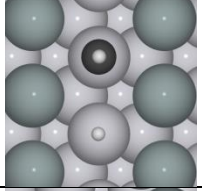
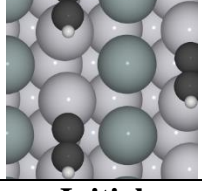
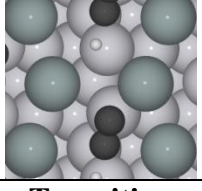
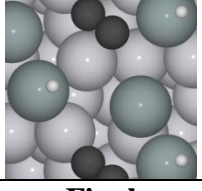
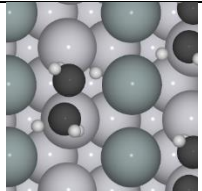
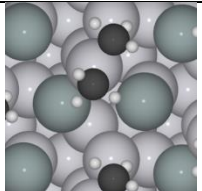
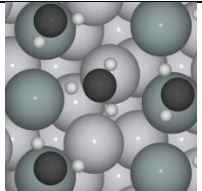
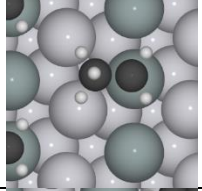
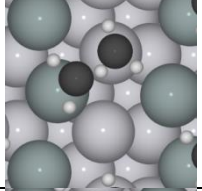
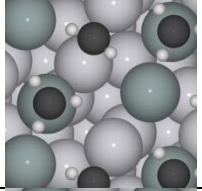
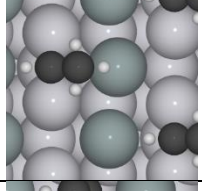
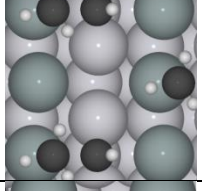
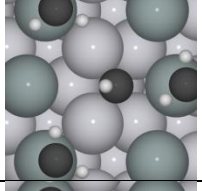
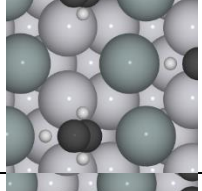
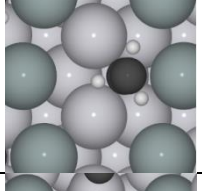
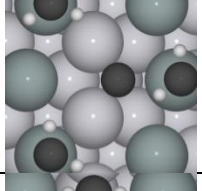
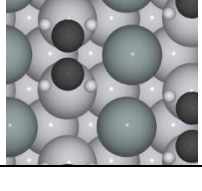
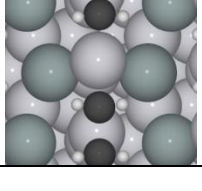
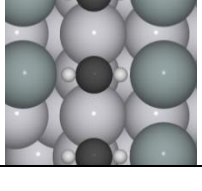
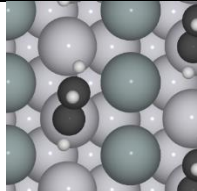
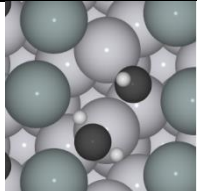
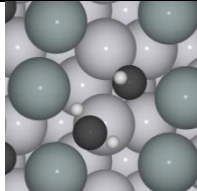
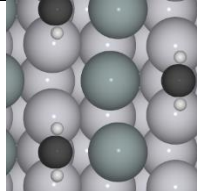
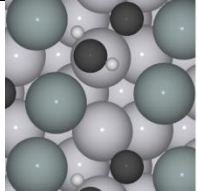
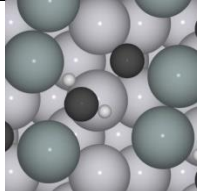
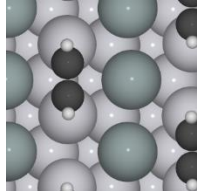
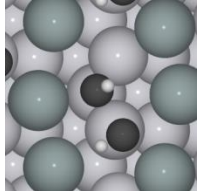
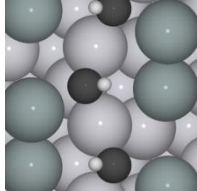
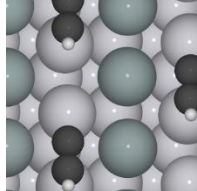
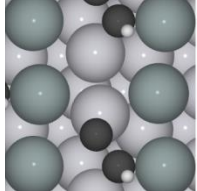
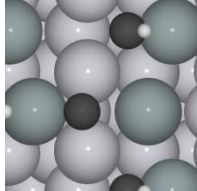
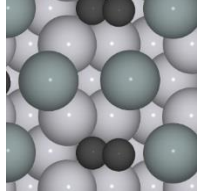
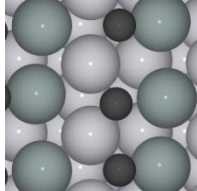
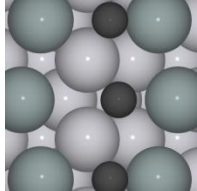
Vinylidene	$\text{CH}_2\text{C}^* + * \rightarrow \text{CH}_2^* + \text{C}^*$			
Acetylene	$\text{CHCH}^* + * \rightarrow \text{CH}^* + \text{CH}^*$			
Acetylidene	$\text{CHC}^* + * \rightarrow \text{CH}^* + \text{C}^*$			
Dicarbon	$\text{C}_2^* + * \rightarrow \text{C}^* + \text{C}^*$			

Table A.4 Initial, final, and transition state structures for each elementary reaction step for C_2H_x species on PtSn/Pt 0-10

Dehydrogenation (reactant)	Reaction	Initial State	Transition State	Final State
Ethane	$\text{CH}_3\text{CH}_3^* + * \rightarrow \text{CH}_3\text{CH}_2^* + \text{H}^*$			
Ethyl	$\text{CH}_3\text{CH}_2^* + * \rightarrow \text{CH}_3\text{CH}^* + \text{H}^*$			
Ethyl	$\text{CH}_3\text{CH}_2^* + * \rightarrow \text{CH}_2\text{CH}_2^* + \text{H}^*$			

Ethylidene	$\text{CH}_3\text{CH}^* + * \rightarrow \text{CH}_3\text{C}^* + \text{H}^*$			
Ethylidene	$\text{CH}_3\text{CH}^* + * \rightarrow \text{CH}_2\text{CH}^* + \text{H}^*$			
Ethylidene (isomerization)	$\text{CH}_3\text{CH}^* \rightarrow \text{CH}_2\text{CH}_2^*$			
Ethylidyne	$\text{CH}_3\text{C}^* + * \rightarrow \text{CH}_2\text{C}^* + \text{H}^*$		proceeds via isomerization and then dehydrogenation	
Ethylidyne (isomerization)	$\text{CH}_3\text{C}^* \rightarrow \text{CH}_2\text{CH}^*$			
Ethene	$\text{CH}_2\text{CH}_2^* + * \rightarrow \text{CH}_2\text{CH}^* + \text{H}^*$			
Vinyl	$\text{CH}_2\text{CH}^* + * \rightarrow \text{CH}_2\text{C}^* + \text{H}^*$			
Vinyl	$\text{CH}_2\text{CH}^* + * \rightarrow \text{CHCH}^* + \text{H}^*$			

Vinylidene	$\text{CH}_2\text{C}^* + * \rightarrow \text{CHC}^* + \text{H}^*$			
Acetylene	$\text{CHCH}^* + * \rightarrow \text{CHC}^* + \text{H}^*$			
Acetylidene	$\text{CHC}^* + * \rightarrow \text{C}_2^* + \text{H}^*$			
C-C Cleavage (reactant)	Reaction	Initial State	Transition State	Final State
Ethane	$\text{CH}_3\text{CH}_3^* + * \rightarrow \text{CH}_3^* + \text{CH}_3^*$			
Ethyl	$\text{CH}_3\text{CH}_2^* + * \rightarrow \text{CH}_3^* + \text{CH}_2^*$			
Ethylidene	$\text{CH}_3\text{CH}^* + * \rightarrow \text{CH}_3^* + \text{CH}^*$			
Ethylidyne	$\text{CH}_3\text{C}^* + * \rightarrow \text{CH}_3^* + \text{C}^*$			
Ethene	$\text{CH}_2\text{CH}_2^* + * \rightarrow \text{CH}_2^* + \text{CH}_2^*$			

Vinyl	$\text{CH}_2\text{CH}^* + * \rightarrow \text{CH}_2^* + \text{CH}^*$			
Vinylidene	$\text{CH}_2\text{C}^* + * \rightarrow \text{CH}_2^* + \text{C}^*$			
Acetylene	$\text{CHCH}^* + * \rightarrow \text{CH}^* + \text{CH}^*$			
Acetylidene	$\text{CHC}^* + * \rightarrow \text{CH}^* + \text{C}^*$			
Dicarbon	$\text{C}_2^* + * \rightarrow \text{C}^* + \text{C}^*$			

Chapter 3: Light alkane dehydrogenation over various Pt Alloys

3.1 Introduction

Ethane is a common product of industrial hydrocarbon processing including petroleum cracking, Fischer-Tropsch synthesis, and ethane hydrocracking. Interest in obtaining ethene from ethane dehydrogenation has increased due to the recent development of shale deposits in North America, which are ‘wet,’ i.e. contain considerable amounts of natural gas liquids¹. In North America, this influx of light alkanes has displaced naphtha cracking as the major source of light alkenes.

There are many methods to dehydrogenate light alkanes from steam cracking to dehydrogenation to oxidative dehydrogenation.¹⁻⁸ High temperature steam cracking generates significant amounts of carbonaceous deposits coating the reactor walls, thus requiring periodic reactor shutdowns to remove coke. Oxidative dehydrogenation eliminates hydrogen gas as a byproduct due to the water formation. It also suffers from a significant selectivity issue due to the competition between the oxidative dehydration reaction and the extremely fast combustion of the alkene product. Catalytic dehydrogenation requires lower temperatures than steam cracking, which lowers the coke formation. Without oxygen, the dehydrogenation process does not compete with the combustion reaction and forms the valuable byproduct, hydrogen gas.

Among pure metal catalysts, Pt exhibits the highest activity, selectivity, and thermal stability for light alkane dehydrogenation,^{7,8,26} but still suffers from significant deactivation due to coke formation,²⁷⁻²⁹ and exhibits undesired C-C bond cleavage activity leading to methane⁷³ in addition to olefin products. Alloying Pt with Sn has been practiced industrially as a means to decrease catalyst deactivation by 60% and reduce

deactivation by 50%³⁴ as compared to Pt alone. Research has also shown that alloying main group elements such as Ga and In^{8,30-34,74-76} show even less deactivation than Sn. Transition metal alloys such as Au,⁷⁷ Cu,⁷⁸ and Re⁷⁹ have also been investigated as potentially useful alloys. The effect of Sn has been explained as a weakening of the bonding between the catalyst surface and the product alkene when compared to the pure Pt case, facilitating alkene desorption.²⁷⁻³² In addition to weakening the ethene binding energy, the rates of dehydrogenation and C-C bond scission were also decreased. The activation energy barrier for dehydrogenation (of ethyl radicals derived from ethane) increased, suggesting that the alloy catalysts exhibit a reduction in activity along with an increase in selectivity.²⁸

Computationally, Density Functional Theory (DFT) has been a useful tool for explaining trends in the experimental data in light alkane dehydrogenation. DFT calculations of decreased alkene binding energy PtSn alloys as compared to pure Pt¹⁶⁻¹⁹ are in good agreement with experimental measurements.²⁷⁻³² DFT has shown evidence that coke formation precursors on Pt(111) are likely formed through the C-C bond cleavage of alkynes,³⁹ which is highly unfavored on PtSn alloys.⁸⁰ In addition, the activation energy barrier for ethene⁸⁰ and propylene⁴⁰ dehydrogenation, are higher on PtSn alloys than the alkene desorption step, which leads to higher alkene selectivity and less coke formation due to alkene dehydrogenation. Calculations on PtAu alloys have shown that Au functions as an electron donor,⁸¹ and enriching Pt with electrons decreases its capability to break C-H bonds.⁸²

Previously, we have investigated the effect of Sn coverage in PtSn alloys on the predicted selectivity towards ethene and coke during ethane dehydrogenation using DFT

calculations.⁸⁰ Our calculations showed that at $\frac{1}{4}$ ML Sn coverage, the alloy effect was entirely electronic, as three-fold hollow sites of Pt atoms were preserved from the pure Pt surface. Nonetheless, the barriers for C-H and C-C bond cleavage were significantly increased, and the binding energy of ethene was significantly reduced, suggesting an improvement in selectivity. At a higher Sn coverage of $\frac{1}{2}$ ML, the geometric ensembles of Pt atoms were disrupted and three-fold binding to Pt atoms was no longer possible, leading to both geometric and electronic effects. The higher Sn coverage was predicted to have an even greater improvement in selectivity. This predicted selectivity difference is in good agreement with experimentally observed trends of lower coke formation with increasing Sn content.^{34,31,41,74, 75} We also found that both hydrogen and ethene compete for the same binding site, leading to enhanced ethene desorption, which is in good agreement with the experimental practice of cofeeding hydrogen during alkane dehydrogenation experiments to reduce coke formation.^{29,34,75}

In this work, we have expanded the scope of electronic structure calculations in alkane dehydrogenation to other Pt-alloy compositions. We have considered twenty-seven Pt-transition metal alloys for metals from Groups 7-11, and Pt-post-transition metal alloys for metals from 12-15. Binding energies of C_1 and C_2 species derived from methane and ethane were calculated on low ($\frac{1}{4}$ ML) and high ($\frac{1}{2}$ ML) coverage surfaces of these alloys, and the alloys grouped according to their preferred binding modes. The key selectivity descriptor for ethane dehydrogenation is the competition of ethene desorption (desired) with ethene dehydrogenation (undesired). The activation energy barrier for ethene dehydrogenation was calculated and compared to the ethene desorption energy to predict which alloys would potentially show enhanced selectivity to ethene at

low and high alloy coverages. The optimal alloy composition was predicted to be coverage dependent. A general approach to predicting the selectivity descriptor – itself an expensive calculation - was developed using a linear scaling relation with the computationally inexpensive calculation of the binding energies simple adsorbates.

3.2 Methods

Periodic, self-consistent DFT calculations were performed using the VASP code^{49,50} within the generalized gradient approximation (GGA-PW91)⁵¹ using projector-augmented wave (PAW)^{52,53} potentials. The single-electron wave functions were expanded using plane waves with an energy cutoff of 400 eV. All metal slabs were based on the (111) surface of fcc Pt, and modeled by a (2×2) surface unit cell with four atomic layers for a total of 16 metal atoms (Pt or Sn). A larger (3×3) unit cell was tested for periodic image interaction effects, but these effects were small (< 0.05 eV) and were consistent between adsorbates of different sizes (e.g. 0.006 eV difference between ethyl and methyl adsorbates). The choice of a smaller unit cell size therefore has a small effect on reported binding energies and a negligible effect on reaction energies.

To generate the surface substitutional alloys, surface Pt atoms were substituted by Sn and the surface structure was reoptimized by relaxation. Substituting one Pt atom with the alloying element, M, in the surface layer creating a $\frac{1}{4}$ monolayer (ML) coverage alloy, and substituting two Pt atoms gives $\frac{1}{2}$ ML coverage. The lattice constant of Pt was calculated to be 3.98 Å, in good agreement with experimental value of 3.92 Å.⁵⁴ A vacuum layer of 12 Å was used to separate any two successive slabs in the z direction (normal to the surface), and a dipole correction was applied and the electrostatic potential was adjusted to ensure that interaction between the surface slab and its periodic images

was negligible.⁵⁵ The Brillouin zone was sampled using a $(6 \times 6 \times 1)$ Gamma-centered Monkhorst-Pack k-point mesh⁵⁶ following a convergence test for adsorbate binding energies with respect to sampling mesh size. The bottom two layers of each metal slab were fixed in their bulk positions while the top two layers were allowed to relax in all calculations. Binding energy is defined as $BE = E_{ads} - E_{slab} - E_{gas}$, where E_{ads} , E_{slab} , E_{gas} are the total energies calculated for the slab with the adsorbate on it, the clean slab, and the adsorbate in the gas phase, respectively. The addition of a single adsorbate molecule to a metal slab with a (2×2) surface until cell corresponds to $\frac{1}{4}$ ML adsorbate coverage. The climbing image nudged elastic band (CINEB) method⁵⁷ was used to calculate transition state and activation energy barriers. All transition states were verified by identifying a single imaginary frequency along the reaction coordinate.

3.3. Results and Discussion

In the dehydrogenation pathway from ethane to ethene, the first C-H bond cleavage step results in ethyl species. Being an asymmetric species, dehydrogenation of ethyl leads to two possible products: ethylidene and ethylene. Our previous work on Pt and PtSn alloys has shown that ethylidene isomerization is energetically unfavorable.⁸⁰ Further, the introduction of Sn increased the ethyl dehydrogenation barriers to both ethylidene and ethene by similar amounts due to the similarities in the C-H bond cleavage mechanisms. As such, it is unlikely that any alloy will alter the selectivity between ethylidene and ethyl in any significant way. Alloying with Sn also increased C-C bond cleavage barriers – as C-C cleavage in ethene was uncompetitive with respect to other reactions of ethene, it will similarly not be considered further here. The remaining reactions of primary interest are the dehydrogenation of ethene to form vinyl, and the

desorption of ethene. The reactions described above are summarized in Figure 3.1, with the reaction and activation energy barriers on the Pt(111) surface shown.

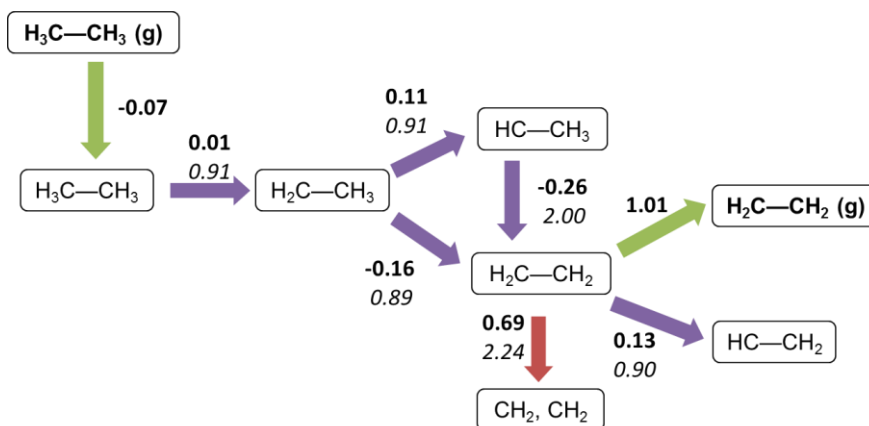


Figure 3.1: The three possible pathways for adsorbed ethene with Pt(111) energies. BOLD is the thermodynamic change in energy and *italic* is the kinetic barrier in eV.

As described in previous computational and experimental work, the key to improving dehydrogenation selectivity is loosening the interaction of the ethene with the catalyst surface, permitting its desorption prior to undergoing further reaction via dehydrogenation.⁸³ Therefore the difference between the desorption energy of ethene (ΔE_{des}) and the activation energy for ethene dehydrogenation ($E_{\text{a,ethene}}$) is a key reactivity descriptor that will be useful to capture the intrinsic selectivity of a particular alloy, and in particular for comparing the predicted selectivities of different alloys. Here we define the **selectivity descriptor** as this difference (eq 3.1). ΔE_{des} is equal to absolute value of the binding energy of ethene.

$$\text{Selectivity Descriptor} = E_{\text{a,ethene}} - \Delta E_{\text{des}} \quad \text{Eq 3.1}$$

The selectivity descriptor defined above appears as the exponential argument of the instantaneous selectivity ($S_{D/U}$) calculated as the rate of desorption divided by the rate of dehydrogenation of ethene. r_i and A_i are the rate and pre-exponential factors for

reaction i, A_0 is the ratio of pre-exponential factors, θ_j is the surface coverage of species j, and * is a surface site.

$$S_{D/U} = \frac{r_{\text{desorption}}}{r_{\text{dehydrogenation}}} = \frac{A_{\text{desorption}} e^{\frac{-\Delta E_{\text{des}}}{RT}} \cdot \theta_{C_2H_4^*}}{A_{\text{dehydrogenation}} e^{\frac{-E_{a,\text{ethene}}}{RT}} \cdot \theta_{C_2H_4^*} \cdot \theta_*} = A_0 e^{\frac{E_{a,\text{ethene}} - \Delta E_{\text{des}}}{RT}} \cdot \frac{1}{\theta_*} \quad \text{Eq 3.2}$$

3.3.1 Model $Pt_xM/Pt(111)$ Surfaces

The phase diagrams of Pt alloys form numerous different bulk compositions. Following our previous work,⁸⁰ we have modeled various alloys using a surface substitutional alloy model. A (2×2) unit cell of fcc Pt(111) with four layers was used as basis for the metal surface. The alloys were created by substitution of one surface Pt atom with the alloying element M in the case of $Pt_3M/Pt(111)$, giving a surface with $\frac{1}{4}$ ML coverage by M, and substitution of two surface Pt atoms with the alloying element M in the case of $PtM/Pt(111)$, giving a surface with $\frac{1}{2}$ ML coverage. The created surfaces are virtually identical in general appearance to the model PtSn alloys from earlier work.⁸⁰

On $Pt_3M/Pt(111)$ surfaces, the guest M atoms are isolated from each other. This allows for two distinct types of three-fold hollow sites. Small clusters of Pt atoms form three-fold hollow sites consisting of three Pt atoms. Around the M atom, the three-fold hollow sites consist of two Pt atoms and one M atom. At higher alloy coverage, $PtM/Pt(111)$, the three-fold Pt-only sites are removed, and all three-fold binding sites consist of one or two M atoms.

The selection of alloying element M was made to include all experimentally reported alloys investigated for selective alkane dehydrogenation, common alloys of Pt used in catalysis, and elements from groups adjacent to these. The 27 elements selected for this study comprise the transition metals from Groups 7-11 and the post-transition

metals and from Groups 12-15. The post-transition metals (**P-T**) metals included Zn, Cd, Hg, Al, Ga, In, Tl, Ge, Sn, Pb, Sb, and Bi. The transition metals were further classified according to preferred binding site for a carbon atom. Those transition metal alloys where a carbon atom placed on a Pt₃M/Pt(111) surface preferred to bind (larger absolute binding energy) to a three-fold hollow with 3 Pt atoms were labelled non-preferred transition (**NT**) metals, because carbon preferentially avoids the guest metal atom M. Conversely, transition metal alloys where the carbon atom preferred binding to a three-fold hollow with two Pt atoms and one guest M atom instead were labelled carbon-preferred transition (**CT**) metals.

The preferred binding mode for carbon atoms on Pt₃M/Pt(111) alloy surfaces for all alloys investigated in this study are summarized in Figure 3.2. All the P-T metal alloys and the NT metal alloys showed the same best binding site, where the carbon atom prefers binding to Pt-only hollow sites. The NT metals included Mn, Fe, Co, Ni, Pd, (Pt), Cu, Ag, and Au. The binding geometry similarity between P-T and NT alloys permitted simple comparison of the electronic effect of the metal atoms, as binding geometries were largely unaltered between these alloys as compared to pure Pt at ¼ ML coverage. Nearly all the alloys considered at the low coverage were also considered at ½ ML coverage except the three largest atoms, Bi, Tl, and Pb. These three tended to rearrange their surfaces at high coverage in some calculations, and so these results were not considered further. The CT metals included Tc, Re, Ru, Os, Rh, and Ir. For all alloys, the preferred binding geometry for carbon atoms followed roughly the guest metal atom's reactivity relative to platinum. Due to the different preferred binding sites for carbon atoms relative

to pure Pt and the P-T and NT alloys, the results on the C-T alloys comprise both geometric and electronic effects at $\frac{1}{4}$ ML coverage.

Those transition metals more reactive than platinum (roughly those falling to the right of Pt in Groups 7-9) were CT alloys. The noble transition metals in Groups 11 and palladium were NT alloys. The first-row transition metals were a major exception to this general rule. Mn, Fe, Co, and Ni would be expected to be more reactive than Pt under normal circumstances – yet the preferred binding sites for carbon atoms were consistent with NT alloys. On these surfaces, carbon atoms prefer to avoid the guest metal atoms due to their high-spin electronic configurations (maximized unpaired electrons in the d orbitals of the guest metal atoms). When these four alloy surfaces were calculated without spin polarization, the electronic structure of the metals converged to low-spin solutions (maximizing paired electrons in the d orbitals), and carbon preferred to bind to the guest atom, similar to the CT alloys.

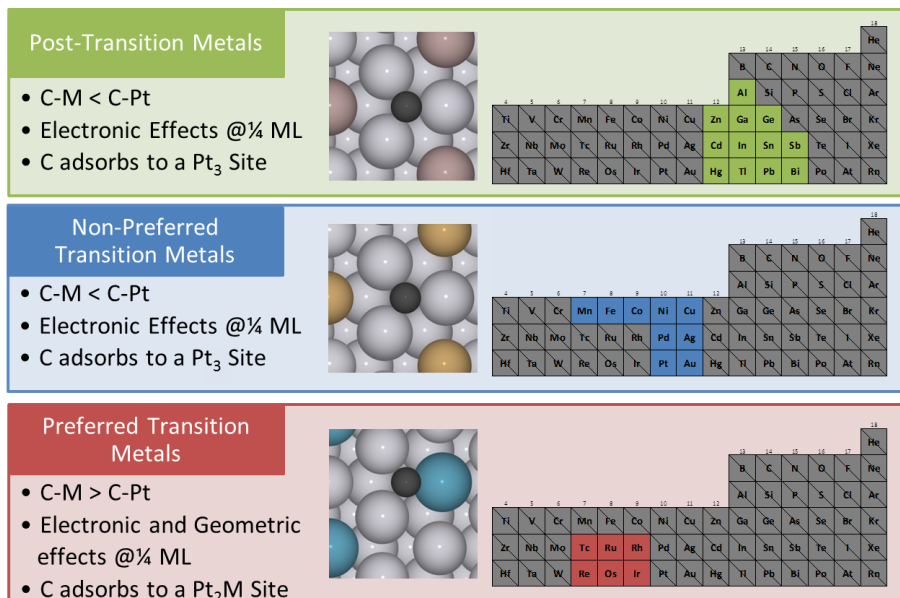


Figure 3.2: Binding site preferences of carbon atoms on three categories of alloying elements: post-transition (P-T) metals, non-preferred transition (NT) metals, and carbon-preferred transition (CT) metals.

3.3.2 Binding of CH_x & H species

For $\frac{1}{4}$ ML and $\frac{1}{2}$ ML coverage alloys, the binding energies and site preferences of CH_x and H species are listed in Table 3.1, Table 3.2 shows the resulting structures. The binding geometries of all NT and P-T surfaces were nearly identical to one another, so Table 3.2 shows the Pt₃In/Pt(111) surface as a representative example. The binding geometries of all CT surfaces were also nearly identical to one another, and so are represented by Pt₃Re/Pt(111) in Table 3.2.

The binding preferences of CH_x and H species followed a similar trend to that of atomic carbon. These species bind preferentially to binding that maximize bonding to Pt atoms on the P-T and NT alloys, and maximize bonding to sites with M atoms on the CT alloys. Additionally, the binding site preference for CH_x species is to sites that allow sp³ hybridization at the carbon atom, and carbon and hydrogen atoms prefer three-fold hollow sites. Following these rules, the binding site preferences in Tables 1 and 2 can be summarized rather concisely. On P-T and NT alloys H, C, and methylidyne (CH) prefer to bind to three-fold Pt hollows (Pt₃) at $\frac{1}{4}$ ML coverage, and three-fold Pt₂M hollows at $\frac{1}{2}$ ML coverage. Methyl (CH₃) prefers to bind to Pt top sites at both coverages. On CT alloys H, C, and CH prefer to bind to three-fold Pt₂M at $\frac{1}{4}$ ML coverage, and three-fold PtM₂ hollows at $\frac{1}{2}$ ML coverage. Methyl (CH₃) prefers to bind to M top sites at both coverages.

Alloys from the P-T and NT groupings generally weakened binding relative to Pt(111), while CT alloys generally strengthened binding. The P-T alloys had a larger effect on the binding energies than the NT alloys. These effects were more pronounced at higher alloy coverages than at lower coverages – CT alloys bound these species even

more strongly and P-T alloys bound these species even more weakly. PtMn alloys did not fit neatly in this trend, with much weaker binding energies at low coverage and much stronger binding at higher coverage. As stronger binding affinity for these species may be expected to correlate with stronger binding of other carbonaceous species as established for PtSn,⁸⁰ this already suggests that P-T alloys will be preferable for higher selectivity during ethane dehydrogenation. Alloy compositions for which binding energies for CH_x species were stronger than on Pt(111) at ¼ ML coverage were not calculated at the higher coverage. This eliminated PtZn among the P-T alloys, and all the NT and CT alloys except for PtMn. PtRe, PtCu, and PtAu were also calculated at the higher coverage as examples of NT and CT alloys for later calculations.

Table 3.1 Binding Energies and Site Preferences for H & CH_x species on various (111) Surfaces **0-1**

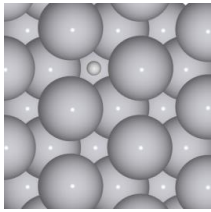
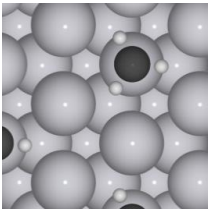
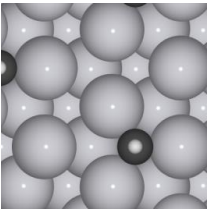
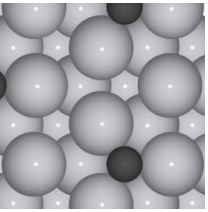
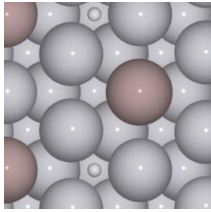
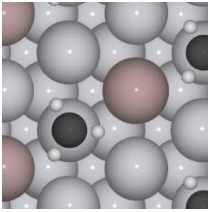
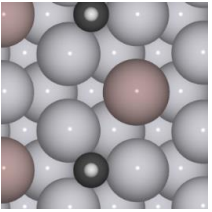
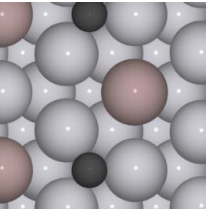
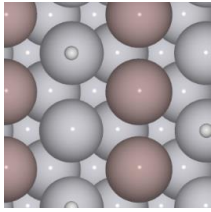
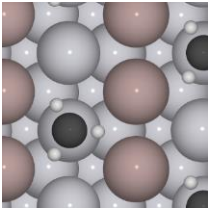
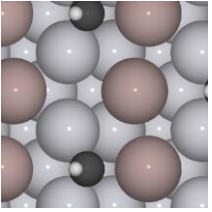
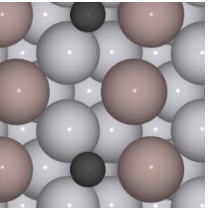
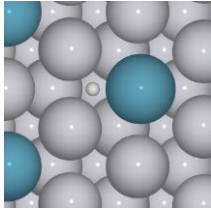
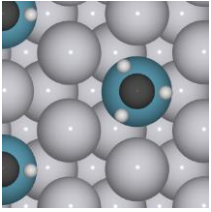
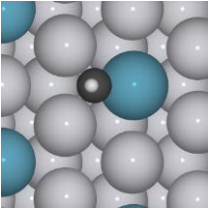
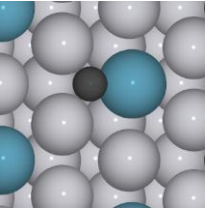
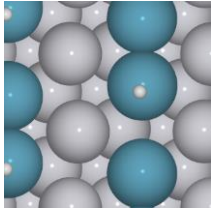
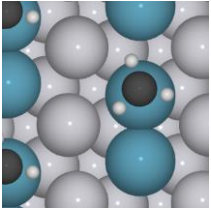
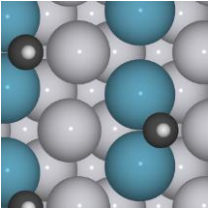
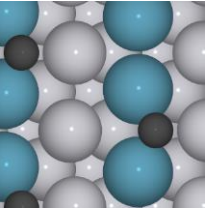
¼ ML Surface		Adsorbate BE (eV)			
		H	C	CH	CH ₃
P-T (¼ ML)	Binding Site ^a	fcc (Pt ₃)	fcc (Pt ₃)	fcc (Pt ₃)	Top (Pt)
	Pt ₃ Zn/Pt	-2.88	-7.10	-6.78	-2.08
	Pt ₃ Cd/Pt	-2.83	-6.90	-6.62	-1.94
	Pt ₃ Hg/Pt	-2.77	-6.67	-6.42	-1.85
	Pt ₃ Al/Pt	-2.86	-6.89	-6.59	-2.05
	Pt ₃ Ga/Pt	-2.83	-6.90	-6.50	-2.02
	Pt ₃ In/Pt	-2.79	-6.55	-6.31	-1.88
	Pt ₃ Tl/Pt	-2.73	-6.58	-6.20	-1.68
	Pt ₃ Ge/Pt	-2.79	-6.84	-6.39	-2.13
	Pt ₃ Sn/Pt	-2.72	-6.28	-6.08	-1.85
	Pt ₃ Pb/Pt	-2.68	-6.51	-6.29	-1.64
	Pt ₃ Sb/Pt	-2.67	-6.26	-6.03	-1.88
	Pt ₃ Bi/Pt	-2.62	-6.24	-5.97	-1.67
NT (¼ ML)	Binding Site ^a	fcc (Pt ₃)	fcc (Pt ₃)	fcc (Pt ₃)	Top (Pt)
	Pt ₃ Mn/Pt	-2.86	-5.27	-6.79	-2.08
	Pt ₃ Fe/Pt	-2.82	-8.34	-8.04	-3.39
	Pt ₃ Co/Pt	-2.83	-7.09	-6.78	-2.10
	Pt ₃ Ni/Pt	-2.86	-7.25	-6.93	-2.14
	Pt ₃ Pd/Pt	-2.79	-7.18	-6.87	-2.10
	Pt ^b	-2.75	-6.97	-6.70	-2.07

	Pt ₃ Cu/Pt	-2.88	-7.29	-6.95	-2.12
	Pt ₃ Ag/Pt	-2.84	-7.20	-6.87	-2.05
	Pt ₃ Au/Pt	-2.78	-7.02	-6.74	-2.02
<hr/>					
CT (¼ ML)	Binding Site ^a	fcc (Pt ₂ M)	fcc (Pt ₂ M)	fcc (Pt ₂ M)	Top (M)
	Pt ₃ Tc/Pt	-2.79	-7.26	-6.96	-2.07
	Pt ₃ Re/Pt	-2.72	-7.31	-7.11	-2.02
	Pt ₃ Ru/Pt	-2.80	-7.38	-7.00	-2.09
	Pt ₃ Os/Pt	-2.78	-7.53	-7.22	-2.06
	Pt ₃ Rh/Pt	-2.84	-7.27	-6.88	-2.13
	Pt ₃ Ir/Pt	-2.80	-7.38	-7.06	-2.09
<hr/>					
½ ML Surface		H	C	CH	CH₃
<hr/>					
P-T (½ ML)	Binding Site ^a	fcc (Pt ₂ M)	fcc (Pt ₂ M)	fcc (Pt ₂ M)	Top (Pt)
	PtCd/Pt	-2.76	-5.83	-5.46	-1.84
	PtHg/Pt	-2.57	-5.91	-5.46	-1.64
	PtAl/Pt	-2.81	-6.01	-5.87	-2.03
	PtGa/Pt	-2.75	-5.90	-5.75	-2.01
	PtIn/Pt	-2.57	-5.38	-5.29	-1.69
	PtGe/Pt	-2.68	-5.68	-5.53	-2.02
	PtSn/Pt	-2.44	-5.69	-5.28	-1.69
	PtSb/Pt	-2.58	-6.21	-5.78	-1.80
<hr/>					
NT (½ ML)	Binding Site ^a	fcc (Pt ₂ M)	fcc (Pt ₂ M)	fcc (Pt ₂ M)	Top (Pt)
	PtMn/Pt	-5.68	-9.44	-9.16	-4.91
	PtCu/Pt	-2.81	-6.86	-6.48	-2.15
	PtAu/Pt	-2.67	-6.29	-6.04	-1.94
<hr/>					
CT (½ ML)	Binding Site ^a	fcc (PtM ₂)	fcc (PtM ₂)	fcc (PtM ₂)	Top (M)
	PtRe/Pt	-2.74	-7.53	-7.24	-2.08

^a Pt_xM_y indicates a three-fold hollow site (x+y=3) consisting of x Pt atoms and y guest metal M atoms.

^b Calculations on pure Pt(111) given for comparison

Table 3.0-2: Best binding geometries for CH_x and H species on Pt and alloy surfaces. PtIn alloy shows the binding locations for all P-T and NT alloys. PtRe alloy shows the binding locations for CT alloys

	H	CH_3	CH	C
Pt				
$\text{Pt}_3\text{In}/\text{Pt}$				
PtIn/Pt				
$\text{Pt}_3\text{Re}/\text{Pt}$				
PtRe/Pt				

3.3.3 Binding of C_2H_x

The selectivity descriptor (eq 3.1) and the reaction pathway to ethene involve three C_2H_x species, ethyl (C_2H_5), ethene (C_2H_4), and vinyl (C_2H_3), whose binding energies and site preferences on select alloy surfaces are given in Table 3.3. The choice of alloys investigated here was partly influenced by the results of the scaling relations in Section 3.3.6, and so only a subset of those alloys in Table 3.1 appear here. As with CH_x

species, the C_2H_x species were generally more stable when their carbon atoms were in sp^3 hybridization geometries regardless of alloy and alloy coverage. Also, the binding geometries avoided C-M bonds for P-T and NT alloys, and maximized C-M bonds in CT alloys regardless of coverage. Ethyl and ethene species showed little variability in their binding geometries across all surfaces (Table 3.4a). Both carbon atoms were in sp^3 hybridization with a single-bond character to the C-C bond. Ethyl bound to the surface via a top site above Pt atoms for P-T and NT alloys, and a top site above the guest metal atom for CT alloys regardless of coverage – binding modes consistent with the carbon atom binding preferences discussed in Section 3.3.1 above. Ethene bound to two top sites on Pt atoms on P-T and NT alloys regardless of alloying element coverage. On CT alloys, ethene bound to top site pairs above Pt and M atoms at low coverage of M, but at higher coverage were able to bind to two M atom top sites due to the proximity of M atoms. These binding structures are given in Table 3.4a.

The vinyl species showed more variability in binding modes than the other species, particularly at $\frac{1}{2}$ ML coverage. On P-T and NT alloys at low coverage, vinyl species bound to the surface with sp^3 hybridization with the CH_2 group on a Pt top site and the CH group in a bridging geometry between two Pt atoms. On CT alloys, the binding mode was similar, with the CH group bridging between a Pt atom and an M atom, and the CH_2 group atop Pt at low coverage and atom M at high coverage. On P-T and NT alloys at $\frac{1}{2}$ ML coverage, the binding geometries varied significantly, as seen in Table 4b. Several alloys maintained the sp^3 hybridization, and varied the orientation of the molecule. On PtMn, the CH_2 group bonded to the guest metal atom, while the CH group bridged two Pt atoms. The much stronger binding energy on this alloy compared to

the other alloys is attributed to the high-spin electronic structure. PtGa adopted a similar binding geometry to PtMn, but with a binding energy similar to the other, low-spin alloys. On PtCu, PtAu, PtCd, PtAl, and PtGe, the CH₂ group preferred a Pt atom instead, forcing the CH group to bridge a Pt-M atom pair, leading to a distorted geometry and a shortened C-C bond, indicating more double-bond character. In contrast to all the preceding examples, where vinyl bound in a bidentate η^2 mode, on PtHg, PtIn, PtSn, and PtSb, vinyl bound in an η^1 fashion where the carbon atoms retained sp² hybridization and a Pt atom took the place of the missing H atom on the CH group. This binding geometry led to significantly weakened binding energy. As the geometric ensembles in the surface layer of the alloy were identical, a significant ligand effect of the guest M atoms was responsible for the changes in binding geometries.

As PtSn alloys are commercially relevant light alkane dehydrogenation catalysts, and PtIn has been reported to be of significant interest in experimental studies,⁷⁵ the binding energy and binding geometry of the vinyl species can be expected to have a significant role in determining the ultimate selectivity of the catalyst at high alloy coverage. Since dehydrogenation is energetically uphill (Table 3.5), a late transition state – one more resembling the final state than the initial state in an elementary reaction – may be expected. For the ethene dehydrogenation reaction (Section 3.3.4), this suggests that the structure of adsorbed vinyl will influence the activation energy barrier, $E_{a, \text{ethene}}$, and therefore the selectivity descriptor (eq 3.1). It should be noted that the binding energy of ethene ($\text{BE}_{\text{C}_2\text{H}_4}$) = $-\Delta E_{\text{des}}$.

Table 3.3: C₂H_x BE & locations on Pt alloy **0-3**

1/4 ML Surface		Adsorbate BE (eV)					
		CH ₃ CH ₂		CH ₂ CH ₂		CH ₂ CH ^b	
P-T (1/4 ML)	Pt ₃ Cd/Pt	Top(Pt)	-1.71	Top(Pt)-Top(Pt)	-0.79	Top(Pt)-Brg(Pt&Pt)	-2.85
	Pt ₃ Hg/Pt	Top(Pt)	-1.63	Top(Pt)-Top(Pt)	-0.65	Top(Pt)-Brg(Pt&Pt)	-2.67
	Pt ₃ Al/Pt	Top(Pt)	-1.85	Top(Pt)-Top(Pt)	-1.00	Top(Pt)-Brg(Pt&Pt)	-3.04
	Pt ₃ Ga/Pt	Top(Pt)	-1.84	Top(Pt)-Top(Pt)	-0.99	Top(Pt)-Brg(Pt&Pt)	-3.07
	Pt ₃ In/Pt	Top(Pt)	-1.65	Top(Pt)-Top(Pt)	-0.67	Top(Pt)-Brg(Pt&Pt)	-2.69
	Pt ₃ Tl/Pt	Top(Pt)	-1.43	Top(Pt)-Top(Pt)	-0.35	Top(Pt)-Brg(Pt&Pt)	-2.32
	Pt ₃ Ge/Pt	Top(Pt)	-1.94	Top(Pt)-Top(Pt)	-0.99	Top(Pt)-Brg(Pt&Pt)	-3.01
	Pt ₃ Sn/Pt	Top(Pt)	-1.65	Top(Pt)-Top(Pt)	-0.64	Top(Pt)-Brg(Pt&Pt)	-2.63
	Pt ₃ Pb/Pt	Top(Pt)	-1.35	Top(Pt)-Top(Pt)	-0.25	Top(Pt)-Brg(Pt&Pt)	-2.22
	Pt ₃ Sb/Pt	Top(Pt)	-1.67	Top(Pt)-Top(Pt)	-0.71	Top(Pt)-Brg(Pt&Pt)	-2.72
	Pt ₃ Bi/Pt	Top(Pt)	-1.41	Top(Pt)-Top(Pt)	-0.35	Top(Pt)-Brg(Pt&Pt)	-2.30
NT (1/4 ML)	Pt ₃ Mn/Pt	Top(Pt)	-1.87	Top(Pt)-Top(Pt)	-1.05	Top(Pt)-Brg(Pt&Pt)	-3.14
	Pt ^c	Top(Pt)	-1.89	Top(Pt)-Top(Pt)	-1.01	Top(Pt)-Brg(Pt&Pt)	-3.10
	Pt ₃ Cu/Pt	Top(Pt)	-1.94	Top(Pt)-Top(Pt)	-1.16	Top(Pt)-Brg(Pt&Pt)	-3.28
	Pt ₃ Au/Pt	Top(Pt)	-1.82	Top(Pt)-Top(Pt)	-0.94	Top(Pt)-Brg(Pt&Pt)	-3.02
CT (1/4 ML)	Pt ₃ Re/Pt	Top(M)	-1.92	Top(M)-Top(Pt)	-1.12	Top(Pt)-Brg(M&Pt)	-3.38
	Pt ₃ Os/Pt	Top(M)	-1.98	Top(M)-Top(Pt)	-1.20	Top(Pt)-Brg(M&Pt)	-3.46
1/2 ML Surface		CH ₃ CH ₂		CH ₂ CH ₂		CH ₂ CH	
P-T (1/2 ML)	PtCd/Pt	Top(Pt)	-1.59	Top(Pt)-Top(Pt)	-0.61	Top(Pt)-Brg(Pt&Pt) ^a	-2.36
	PtHg/Pt	Top(Pt)	-1.39	Top(Pt)-Top(Pt)	-0.32	Top(Pt)	-2.10
	PtAl/Pt	Top(Pt)	-1.81	Top(Pt)-Top(Pt)	-0.93	Top(Pt)-Brg(Pt&Pt) ^a	-2.79
	PtGa/Pt	Top(Pt)	-1.79	Top(Pt)-Top(Pt)	-0.93	Top(M)-Brg(Pt&Pt)	-2.44
	PtIn/Pt	Top(Pt)	-1.46	Top(Pt)-Top(Pt)	-0.38	Top(Pt)	-2.15
	PtGe/Pt	Top(Pt)	-1.81	Top(Pt)-Top(Pt)	-0.91	Top(Pt)-Brg(Pt&Pt) ^a	-2.62
	PtSn/Pt	Top(Pt)	-1.50	Top(Pt)-Top(Pt)	-0.42	Top(Pt)	-2.10
	PtSb/Pt	Top(Pt)	-1.20	Top(Pt)-Top(Pt)	-0.29	Top(Pt)	-1.83
NT (1/2 ML)	PtMn/Pt	Top(Pt)	-4.68	Top(Pt)-Top(Pt)	-3.88	Top(M)-Brg(Pt&Pt)	-5.57
	PtCu/Pt	Top(Pt)	-1.96	Top(Pt)-Top(Pt)	-1.24	Top(Pt)-Brg(Pt&Pt) ^a	-3.37
	PtAu/Pt	Top(Pt)	-1.74	Top(Pt)-Top(Pt)	-0.83	Top(Pt)-Brg(Pt&Pt) ^a	-2.50
CT (1/2 ML)	PtRe/Pt	Top(M)	-1.88	Top(M)-Top(M)	-1.08	Top(M)-Brg(M&Pt)	-3.67

^aAdjacent top and bridge sharing one Pt atom

Table 3.4 Best binding geometries of C_2H_x species on Pt, NT, and P-T alloys. b) Expanded table for vinyl on PtM alloys 0-4

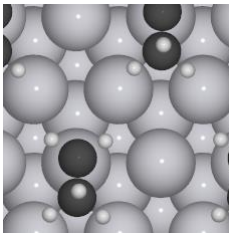
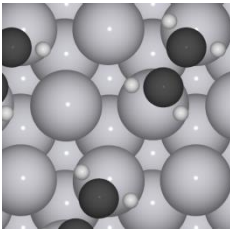
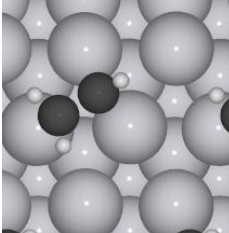
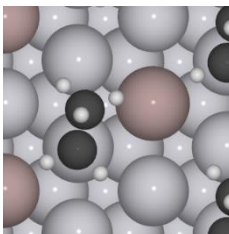
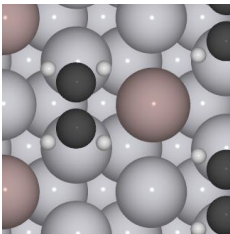
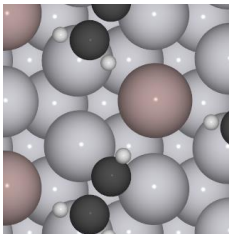
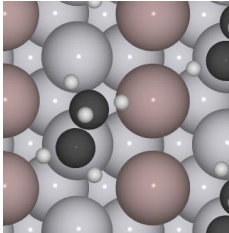
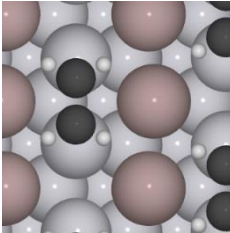
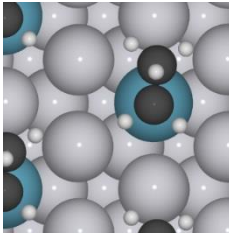
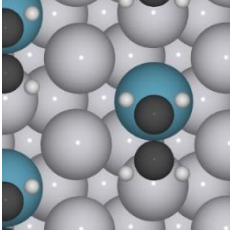
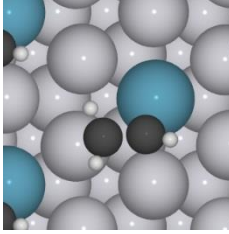
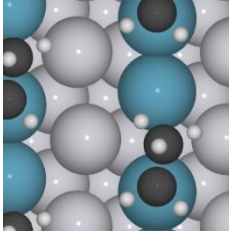
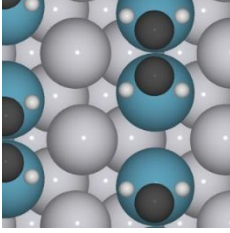
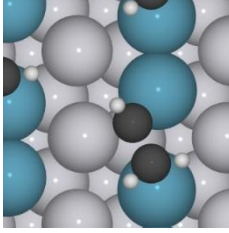
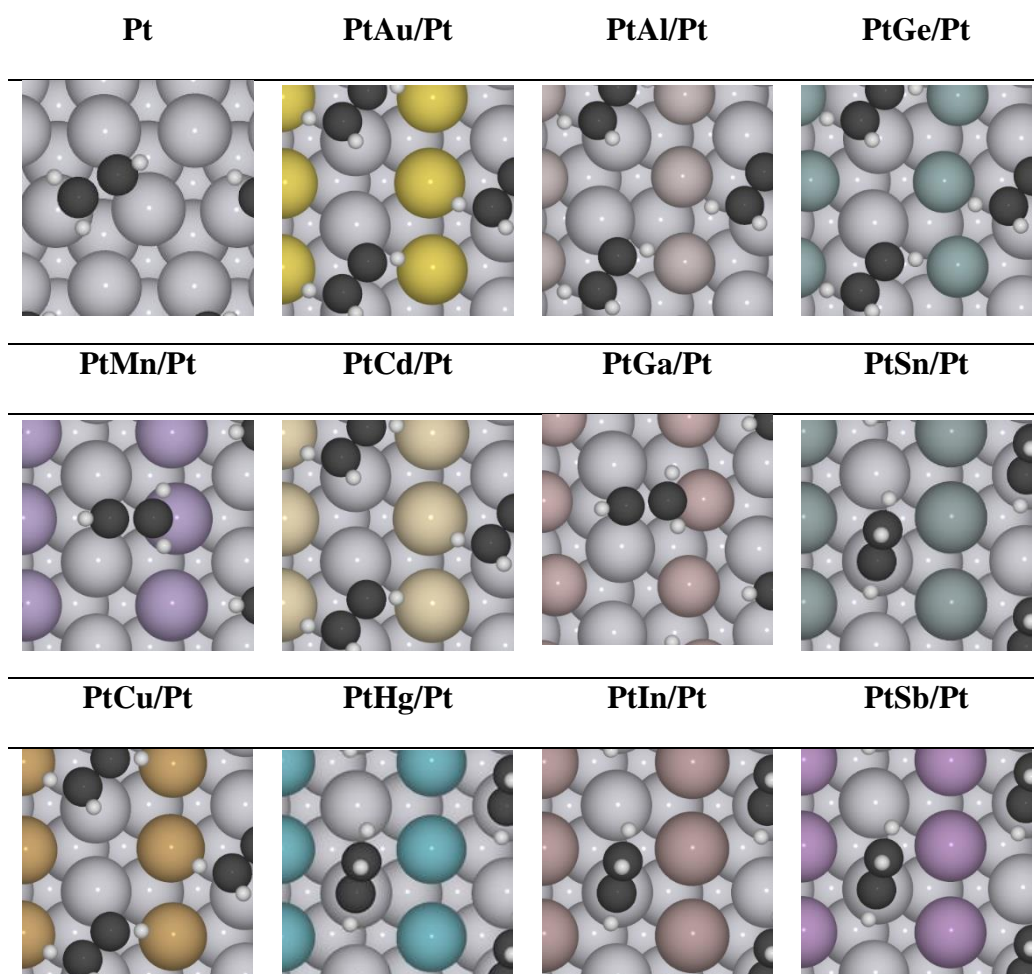
	Ethyl CH_3CH_2	Ethene CH_2CH_2	Vinyl CH_2CH
Pt			
Pt ₃ In/Pt			
PtIn/Pt			*Vinyl sites listed in Table 3.4b
Pt ₃ Re/Pt			
PtRe/Pt			

Table 3.4b Expanded table for vinyl on PtM alloys

3.3.4 Ethene Dehydrogenation Mechanism

The selectivity (and selectivity descriptor) of a particular surface is a strong function of how much more difficult it is to remove hydrogen from ethene than it is to remove ethene from the surface. The C-H bond cleavage barriers for ethene, $E_{a,\text{ethene}}$, on select alloys at high and low coverage were calculated and are given in Table 3.5. Due to the higher computational cost of nudged elastic band calculations for computing barriers relative to structure optimization calculations reported throughout the rest of this work the number of alloy surfaces considered here was kept small, and the alloys tested were in

part selected from the analysis in Section 3.3.6. Since the high binding energies observed on CT alloys in Sections 3.3.2-3.3.3 suggested poor selectivity for CT alloys, they were not considered here.

Table 3.5: Activation Energy^a and Reaction Energy^a for ethene dehydrogenation (in eV), $\text{CH}_2\text{CH}_2^* + ^* \rightarrow \text{CH}_2\text{CH}^* + \text{H}^*$ 0-5

¹ / ₄ ML Surface		Ethene Dehydrogenation		
		$E_{\text{a,ethene}}$	ΔE	$\infty\text{FS}^{\text{b}}$
P-T (¹/₄ ML)	Pt ₃ Hg/Pt	0.98	0.43	0.18
	Pt ₃ Ga/Pt	0.76	0.27	0.05
	Pt ₃ In/Pt	0.96	0.40	0.17
	Pt ₃ Tl/Pt	1.05	0.51	0.32
	Pt ₃ Sn/Pt	1.01	0.45	0.26
	Pt ₃ Pb/Pt	1.09	0.59	0.28
	Pt ₃ Sb/Pt	0.99	0.51	0.28
	Pt ₃ Bi/Pt	1.12	0.68	0.39
NT (¹/₄ ML)	Pt ^c	0.90	0.32	0.13
	Pt ₃ Au/Pt	0.86	0.40	0.12
¹ / ₂ ML Surface		$E_{\text{a,ethene}}$	ΔE	∞FS
P-T (¹/₂ ML)	PtHg/Pt	1.41	0.71	0.62
	PtGa/Pt	1.43	0.97	0.73
	PtIn/Pt	1.49	0.70	0.63
	PtSn/Pt	1.48	0.85	0.85
	PtSb/Pt	1.48	0.90	0.85
NT (¹/₂ ML)	PtAu/Pt	1.27	0.87	0.61

At ¹/₄ ML alloy coverage, the reaction mechanism on P-T and NT alloys were visually similar, and the initial, transition, and final states are represented in Figure 3 by PtIn. The similarities in transition states for the different alloys can be seen in Table S1. The differences in barriers and reaction energies between the alloys can be attributed to a combination of the electronic ligand effects and strain effects (especially for the larger M atoms) of the guest metal atoms. Ga and Au lowered the barrier to dehydrogenation, while the remaining alloys increased the barrier, though the effects were small. The

barrier on Pt(111) was 0.90 eV, and the largest barrier at $\frac{1}{4}$ ML alloy coverage was 1.12 eV for Pt₃Bi, and most of the alloys were within 0.1 eV of the Pt value. As would be expected for a late transition state reaction, the reaction energies followed a similar trend to $E_{a,\text{ethene}}$, in that the range was small, and Pt₃Bi had the most endothermic reaction at 0.68 eV, compared to 0.32 for Pt.

3.3.5 Selectivity

The binding energies and barriers from Tables 3.3 and 3.5 allow the calculation of the selectivity descriptors (eq 3.1) for those alloys where activation barriers were calculated and are given in Table 3.6. At $\frac{1}{4}$ ML alloy coverage, PtPb had the highest selectivity descriptor at 0.84 eV. That is to say that cleaving the C-H bond in ethene was calculated to be 0.84 eV more difficult than desorbing the ethene, suggesting that this surface would show a low preference for coke formation pathways and a higher selectivity towards gaseous ethene. This compares favorably to PtSn, which is used commercially, for which the selectivity descriptor at low coverage was 0.37, and very favorably compared to pure Pt(111), for which the selectivity descriptor was negative, indicating a preference for coke formation pathways ethene desorption. PtAu and PtGa also had negative selectivity descriptors. Of the other alloys calculated, PtBi and PtTl also showed large values for $E_{a,\text{ethene}} - \Delta E_{\text{des}}$, while the remaining alloys calculated were similar to Pt Sn, albeit slightly poorer.

Increasing the alloy coverage improved the selectivity descriptor for all alloys, and even alloys with negative selectivity descriptors at low coverage were more favorable at high coverage. The three best low-coverage alloys, Pb, Bi, and Tl could not be evaluated at higher coverage with the current alloy model due to their large atomic radii

as discussed in Section 3.3.1. The selectivity descriptor of PtSn improved to 1.05 eV at the higher coverage. The selectivities for the alloys of Hg, In, and Sb improved by larger amounts, such that all three were slightly more selective than PtSn at the higher coverage, with PtSb at 1.18 eV. It should be noted that the ordering of the selectivities at low coverage did not match the ordering at high coverage. For example, PtSb was the best P-T alloy calculated at high coverage, but the worst (excepting PtGa) at lower coverage.

Table 3.6: The DFT-calculated selectivity descriptor values on Pt alloys (in eV) **0-6**

Alloy		Selectivity Descriptor	
		$\frac{1}{4}$ ML	$\frac{1}{2}$ ML
P-T	Hg	0.33	1.09
	Ga	-0.23	0.49
	In	0.28	1.11
	Tl	0.70	--
	Sn	0.37	1.05
	Pb	0.84	--
	Sb	0.28	1.18
	Bi	0.78	--
NT	Pt ^a	-0.12	--
	Au	-0.08	0.43

These results suggest that it is possible to improve upon the intrinsic selectivity of the PtSn alloy, but the choice of alloying element depends strongly on the coverage of the alloying element in the surface of the synthesized metal alloy nanoparticles. If low coverage prevails, PtPb shows promise, as do PtBi and PtTl. At high coverage, PtSb appears the best, followed closely by PtIn and PtHg.⁸⁴ However, PtSn represents the best compromise that may reflect conditions in industrial catalyst manufacturing. When tight control over the ratio of elements in the catalyst particle surfaces is not achievable or is not sought, the best alloy may be one that performs well at any alloy concentration. In

fact, many nanoparticle synthesis techniques produce a distribution of alloy concentrations across different particles, and so both high and low coverages will be present in a real catalyst powder or particle concurrently. In this regard, PtSn is a strong choice at both low and high alloy coverages.

3.3.5 Scaling Relations

Due to the high computational cost of calculating barriers and sampling many binding geometries of C_2H_x species, the selectivity descriptor in eq 3.1 is not easily computed over a large range of alloys and concentrations. Even in this study, only a subset of alloys was calculated using DFT. As such, scaling relationships were developed to accurately predict both parts of the selectivity descriptor: the ethene desorption energy (ΔE_{des}) and the ethene dehydrogenation barrier ($E_{a,ethene}$). To minimize the computational cost of the calculations required to accurately predict selectivity, correlations were sought with simple data sets computed with DFT for CH_x species and requiring only structure optimization calculations.

A separate scaling relation for each term of the selectivity descriptor was sought. For the desorption energy (i.e. -binding energy) of ethene, a correlation was with the binding energy of a methyl group (BE_{CH_3}) on the same surface. In both bound ethene and methyl groups, carbon atoms are sp^3 hybridized, species bind to top sites, and the binding preferences between a Pt atom and a guest metal atom are preserved for both species. That is, P-T and NT alloys have both ethene and methyl bound to Pt atoms, while CT alloys prefer binding through the guest metal atom. These factors contribute to a reasonably linear scaling relation between ΔE_{des} and BE_{CH_3} , as seen in Figure 3.4 for both high and low coverage of the alloying element. Other species that bind to top sites

gave similarly good correlations, such as between ethyl and methyl groups. Correlation between ΔE_{des} and other CH_x species was also tested, such as carbon, but was poorer than with methyl. This indicates that the nature of the binding site (i.e. a top site or a three-fold hollow) is important in the predictive power of the calculation. The equation for the line correlating ΔE_{des} and BE_{CH_3} for the lower coverage alloys is given below, where α_1 and β_1 are the slope and intercept, with values of -1.64 and -2.40 eV respectively.

$$\Delta E_{\text{des}} = \alpha_1 \text{BE}_{\text{CH}_3} + \beta_1 \quad \text{Eq. 3.3}$$

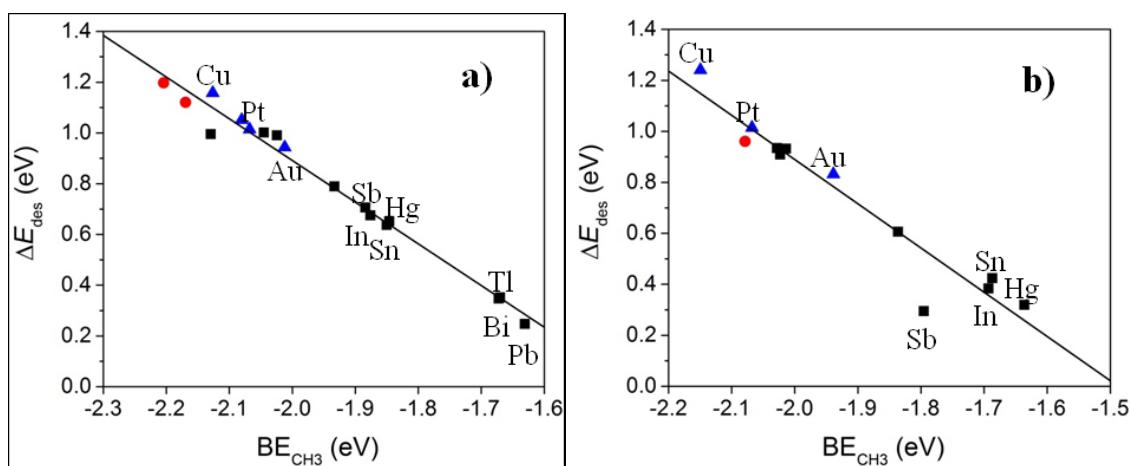
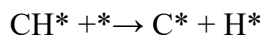


Figure 3.3: A relationship between methyl binding energy (BE_{CH_3}) and desorption energy of ethene (ΔE_{des}) at a) 1/4 ML and b) 1/2 ML coverage. NT alloys in blue, P-T alloys in black, and CT alloys in red. **0-3**

Finding a scaling relation for $E_{\text{a,ethene}}$ was less straightforward. The Brønsted–Evans–Polanyi relation has been extensively used to relate reaction energies to activation energy barriers^{85–87}. Typically, one might correlate the barrier for ethene dehydrogenation to the reaction energy for dehydrogenation. Instead, a relation that relied only on the binding energy calculations of simple CH_x species would be much more computationally efficient, and so a representative C-H bond-cleaving step was desired. $E_{\text{a,ethene}}$ is the difference in energy between the transition state and adsorbed ethene. An analysis of the bonding changes between these structures suggests a reasonable set of variables to use for

the correlations. As seen in Figure 3.3, between the initial and transition states a C-H bond is weakened, and a Pt-H bond is forming, and a second new bond will form between carbon and platinum. Among reactions of CH_x species, methylidyne dehydrogenation is the simplest because the reaction does not involve the breaking or formation of any C-M or C-Pt bonds, so that the C-H bond breaking and Pt-H/M-H bond formation energies can be isolated, as both the reactant and product involve carbon in a three-fold hollow site.



While reaction energy for methylidyne dehydrogenation, ΔE_{CH} , includes the breaking of the C-H bond and the formation of the Pt-H bond, it does not adequately account for the nascent interaction between carbon and platinum in the transition state of ethene dehydrogenation. To account for this interaction, it was found that adding BE_{CH3} to ΔE_{CH} accounted for the changes in bonding encapsulated in $E_{\text{a,ethene}}$, such that a linear correlation between the sum and the barrier was found. The correlation for the lower alloy coverage of $\frac{1}{4}$ ML, given in Figure 3.5, was only possible because the transition state structures in all these alloys were so similar. CT alloys were left out of this correlation, as $E_{\text{a,ethene}}$ values were not calculated for these alloys, and their transition state structures would be expected to differ from the P-T and NT alloys due to the different initial and final state structures (Table 3.4a).

At $\frac{1}{2}$ ML coverage by the alloying element, the transition state structures varied to such an extent (see Table B1) as to make a simple correlation impossible - a separate correlation would be needed for each reaction mechanism, and the mechanism followed by a particular alloy would not be known a priori. The structure of the vinyl adsorbate (obtained from a structure minimization calculation) was predictive of the transition state

structure (obtained from the more expensive transition state searching calculation), but the authors felt that the value of separate correlations for much smaller subsets of metal alloy surfaces would be of little value. For this reason, no further correlations on the high alloy coverage surfaces were sought. The equation for the line correlating $E_{a,\text{ethene}}$ and BE_{CH3} and ΔE_{CH} for the lower coverage alloys is given below, where α_2 and β_2 are the slope and intercept, with values of 0.46 and 1.53 eV respectively.

$$E_{a,\text{ethene}} = \alpha_2(BE_{CH3} + \Delta E_{CH}) + \beta_2 \quad \text{Eq. 3.4}$$

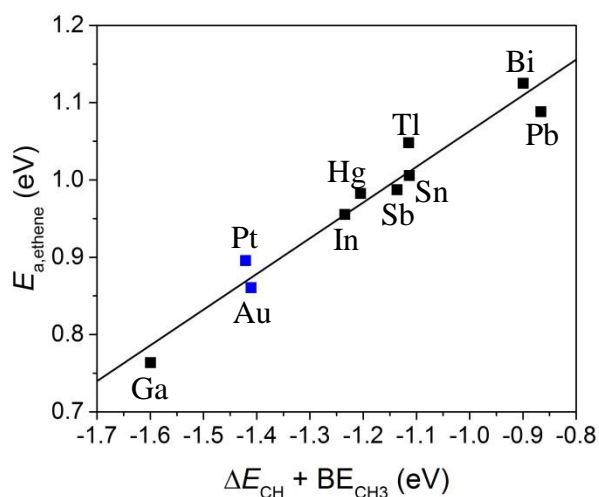


Figure 3.4: A linear relationship between the methyldiene dehydrogenation reaction energy (ΔE_{CH}) plus the methyl binding energy (BE_{CH3}) versus ethene dehydrogenation barrier ($E_{a,\text{ethene}}$) for alloys at $\frac{1}{4}$ ML coverage. NT alloys in blue, and P-T alloys in black.

As the values for BE_{CH3} and ΔE_{CH} were calculated previously in populating Table 3.3 (summarized in Table 7), eq 3.3 and eq 3.4 can be used to predict values of ΔE_{des} and $E_{a,\text{ethene}}$ from a scaling relation that were not calculated by DFT, saving significant computational expense. These are included in Table B2. Since the selectivity descriptor eq 3.1 is simply the difference between $E_{a,\text{ethene}}$ and ΔE_{des} , subtracting eq 3 from eq 4 results in a scaling relation between BE_{CH3} and ΔE_{CH} and the selectivity descriptor (eq 5), where $\alpha = (\alpha_2 - \alpha_1) = 2.1$, α_2 is as before, and $\beta = (\beta_2 - \beta_1) = 3.93$ eV.

$$\text{Selectivity Descriptor} = E_{a,\text{ethene}} - \Delta E_{\text{des}} = \alpha \text{BE}_{\text{CH}_3} + \alpha_2 \Delta E_{\text{CH}} + (\beta_2 - \beta_1) \quad \text{Eq. 3.5}$$

Table 3.7 Selectivity Predictors and descriptors for ethene dehydrogenation for ¼ ML coverage alloys. 0-7

¼ ML Surface		BE_{CH3}	ΔE_{CH}	$E_{a,\text{ethene}} - \Delta E_{\text{des}}$	
				Scaling Relation ^a	DFT ^b
P-T	Pt ₃ Pb/Pt	-1.63	0.76	0.84	0.84
	Pt ₃ Bi/Pt	-1.67	0.77	0.76	0.78
	Pt ₃ Tl/Pt	-1.67	0.56	0.66	0.70
	Pt ₃ Sn/Pt	-1.85	0.74	0.37	0.37
	Pt ₃ Hg/Pt	-1.85	0.64	0.33	0.33
	Pt ₃ Sb/Pt	-1.88	0.75	0.30	0.28
	Pt ₃ In/Pt	-1.88	0.64	0.27	0.28
	Pt ₃ Cd/Pt	-1.93	0.55	0.10	-
	Pt ₃ Ga/Pt	-2.02	0.42	-0.15	-0.23
	Pt ₃ Al/Pt	-2.05	0.51	-0.15	-
	Pt ₃ Zn/Pt	-2.07	0.47	-0.22	-
	Pt ₃ Ge/Pt	-2.13	0.42	-0.37	-
NT	Pt ₃ Au/Pt	-2.01	0.60	-0.04	-0.08
	Pt	-2.07	0.65	-0.13	-0.12
	Pt ₃ Ag/Pt	-2.05	0.50	-0.16	-
	Pt ₃ Pd/Pt	-2.10	0.56	-0.24	-
	Pt ₃ Co/Pt	-2.10	0.51	-0.27	-
	Pt ₃ Cu/Pt	-2.13	0.44	-0.35	-
	Pt ₃ Ni/Pt	-2.14	0.47	-0.37	-

With this scaling relation, the selectivity for each alloy considered at the simplest level of DFT calculation (binding of CH_x species only) could be predicted, and the alloys ranked from most promising to least promising (Table 3.7). Many alloys were predicted to be more selective than pure Pt, and the alloys of Pb, Bi, and Tl were predicted to be more selective than PtSn. With the exception of Au, only P-T alloys were predicted to be more selective than Pt, and even then Au was only slightly more selective. The remaining NT transition metals were predicted to be less selective than pure Pt(111). Some high spin alloys such as Fe and Mn did not fit the trend formed by the remaining alloys, and so

are not included in Table 3.7. The CT alloys are omitted as the parameters in (eq 3.5) were developed without CT alloy data.

Table 3.7 shows predictive power for selectivity in low coverage alloys, as the DFT values (when available) are in good agreement with the scaling relation. Due to the lack of correlation for activation energy barriers at the higher coverage alloys, a similar scaling relation could not be made. While it is tempting to predict that the relative ordering of the alloys would not change between low and high coverage, this was not the case as seen even in the relatively small number of DFT-calculated selectivity descriptors in Table 3.6. This illustrates that scaling relations to predict selectivity can be coverage dependent for binary metal alloy surfaces.

3.4. Conclusions

Density functional theory has been applied to determine the effects of alloying Pt with various elements on the selectivity of ethene. The binding energy and geometry of methane derivatives has been calculated in a comprehensive manner on $\text{Pt}_3\text{M}/\text{Pt}(111)$ surface substitutional alloys where M was transition metals and main group elements. Using the binding energies and geometries a relationship was derived between the C_1 species methyl and the C_2 species ethene to predict binding energies. C-H bond scission was done in a similar manor using the Brønsted–Evans–Polanyi relation to predict the dehydrogenation barrier of ethene with C_1 derivatives. These two factors were then combined to predict the difference between the ethene dehydrogenation barrier and desorption with a high degree of accuracy.

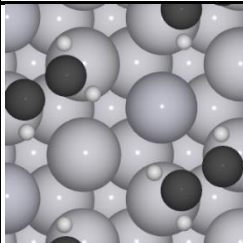
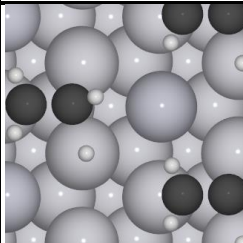
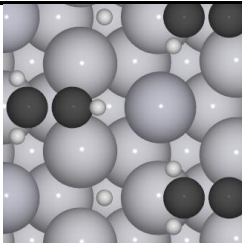
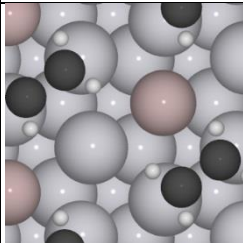
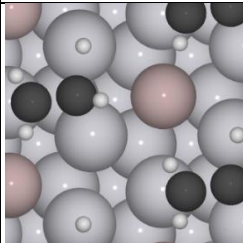
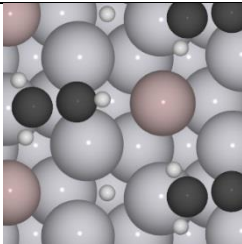
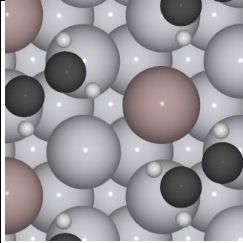
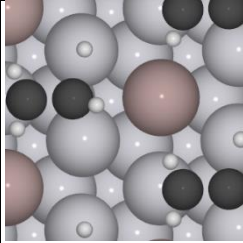
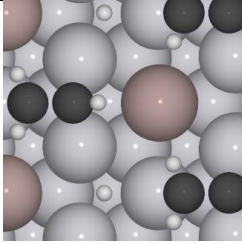
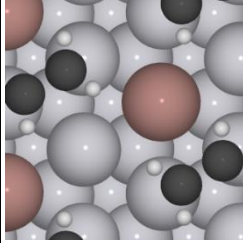
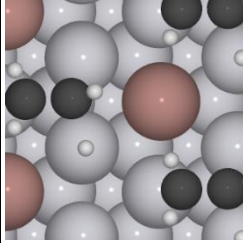
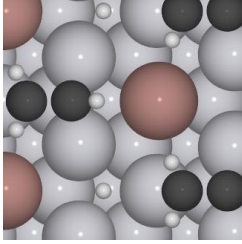
A similar approach was applied to alloys with $\frac{1}{2}$ ML of the alloying element to predict the ethene dehydrogenation barrier and binding energy with C_1 species. The binding energies of C_1 species were able to predict the binding energies of C_2 species with similar binding geometries but not species whose binding geometry changed. C-H bond scission could not be properly correlated between C_1 and C_2 due to altered binding locations leading to multiple dehydrogenation mechanisms between alloys.

Selectivity was found to be dependent on alloy coverage. At $\frac{1}{4}$ ML coverage, PtSn was found to be much better than at $\frac{1}{2}$ ML. Hg, Sb, and In alloys showed lower selectivity than Sn at low coverage but higher selectivity at higher coverage.

The Pt alloys found to have the highest selectivity at $\frac{1}{4}$ ML coverage were the PtBi, PtTl, and PtPb, none of which appeared viable for ethane dehydrogenation due to melting point issues. These alloys are possibly the best alloy for propane dehydrogenation as it shows high selectivity for ethane dehydrogenation at low alloy concentrations. PtIn was found to have higher selectivity than PtSn at $\frac{1}{2}$ ML coverage and could be better at ethane dehydrogenation if local alloy concentration is monitored and maintained.

3.A Supporting Information: PtM alloys

Table A.1: Initial, final, and transition state structures for ethene dehydrogenation mechanism on Pt₃M/Pt and PtM/Pt.

		$\text{C}_2\text{H}_4^* \rightarrow (\text{C}_2\text{H}_3 + \text{H})^*$		
$\frac{1}{4}$ ML Surface		Reactant state	Transition state	Product state
P-T	Pt ₃ Hg/Pt			
	Pt ₃ Ga/Pt			
	Pt ₃ In/Pt			
	Pt ₃ Tl/Pt			

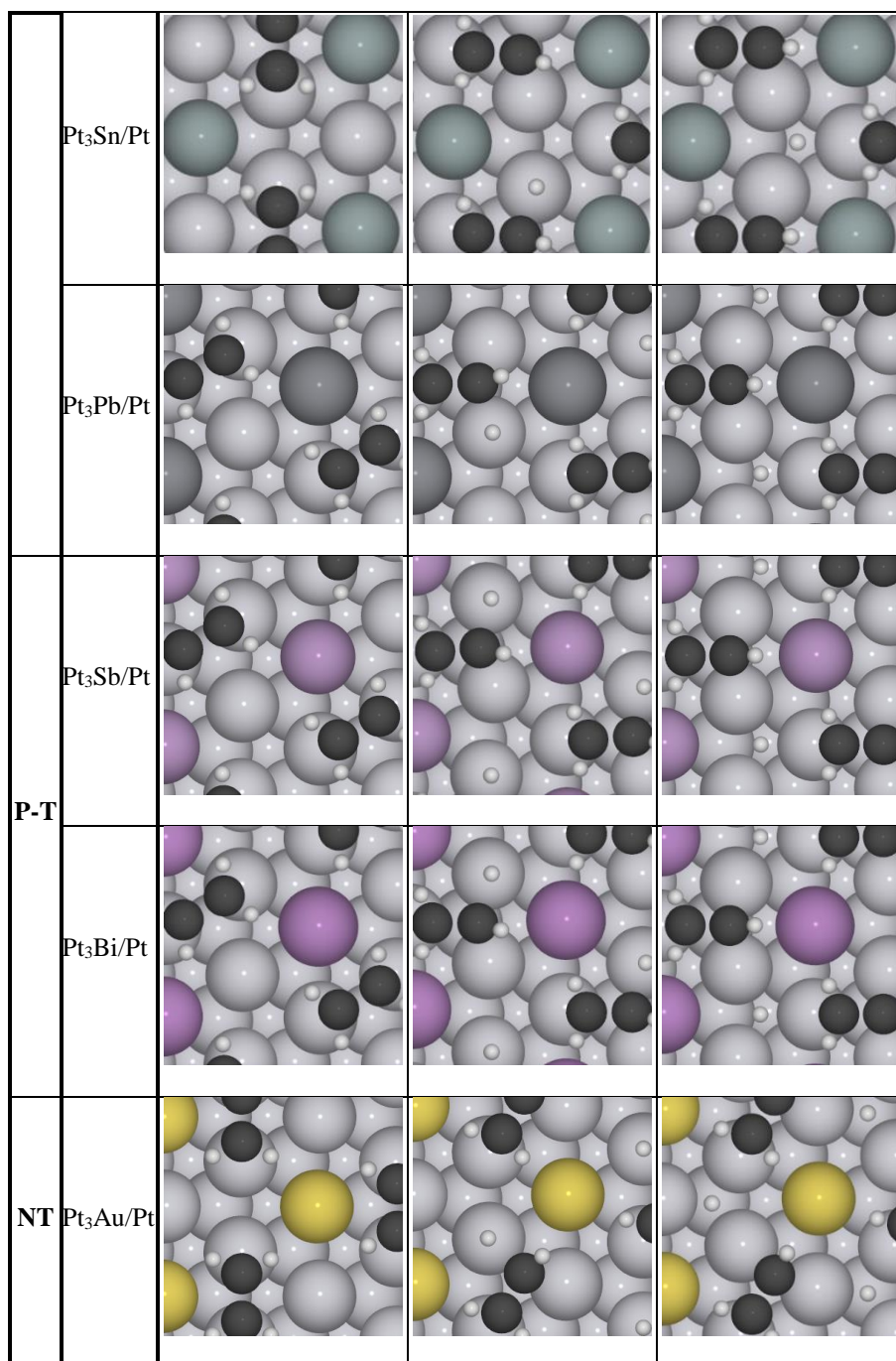


Table A.2: Ethene dehydrogenation barrier and desorption energy calculated through scaling relations (in eV).

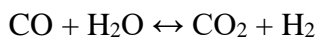
		Scaling Relation	
$\frac{1}{4}$ ML Surface		$E_{a,\text{ethene}}$	ΔE_{des}
P-T	Pt ₃ Pb/Pt	1.13	0.28
	Pt ₃ Bi/Pt	1.11	0.35
	Pt ₃ Tl/Pt	1.01	0.35
	Pt ₃ Sn/Pt	1.01	0.64
	Pt ₃ Hg/Pt	0.97	0.64
	Pt ₃ Sb/Pt	1.00	0.70
	Pt ₃ In/Pt	0.96	0.69
	Pt ₃ Cd/Pt	0.89	0.78
	Pt ₃ Ga/Pt	0.79	0.93
	Pt ₃ Al/Pt	0.81	0.97
	Pt ₃ Zn/Pt	0.79	1.00
	Pt ₃ Ge/Pt	0.74	1.10
NT	Pt ₃ Mn/Pt	1.64	0.91
	Pt ₃ Au/Pt	0.87	1.00
	Pt	0.87	0.97
	Pt ₃ Ag/Pt	0.81	1.05
	Pt ₃ Pd/Pt	0.81	1.06
	Pt ₃ Co/Pt	0.79	1.10
	Pt ₃ Cu/Pt	0.74	1.12
	Pt ₃ Ni/Pt	0.75	1.00
	Pt ₃ Fe/Pt	0.21	1.04
CT	Pt ₃ Tc/Pt	- ^a	1.17
	Pt ₃ Ru/Pt	- ^a	1.09
	Pt ₃ Re/Pt	- ^a	1.18
	Pt ₃ Rh/Pt	- ^a	1.23
	Pt ₃ Ir/Pt	- ^a	0.28
	Pt ₃ Os/Pt	- ^a	0.35

^a Because the relation for predicting $E_{a,\text{ethene}}$ was developed using a data set that excluded all CT alloys, these values cannot be calculated using the same relation.

Chapter 4: Density Functional Theory Investigation of the Role of Cocatalytic Water in Water Gas Shift Reaction over Anatase TiO₂ (101)

4.1 Introduction

Clean energy production and conversion are among the biggest challenges of the 21st century. These include effective utilization of energy resources, as well as clean end-use applications that limit emissions of CO₂ and other pollutants. Hydrogen gas is a promising clean-burning energy carrier as water is the only byproduct of its consumption. Steam reforming of methane is the primary method for industrial hydrogen production today, producing over 50% of the world's hydrogen,⁸⁸⁻⁹⁰ and coproducing carbon monoxide. Chemical synthesis with hydrogen such as Fischer-Tropsch synthesis utilizes the water gas shift reaction (WGS) reaction to adjust the critical ratio of hydrogen gas to carbon monoxide.⁹¹ Primary fuel uses of hydrogen gas such fuel cells heavily depend on WGS to increase hydrogen yield and remove carbon monoxide from the hydrogen stream, as many hydrogen fuel cell catalysts are easily poisoned by carbon monoxide.⁹²



Many catalysts have been studied for the WGS reaction, most of them consisting of metal particles supported on metal oxides.⁹³⁻¹⁰¹ Typically the role of the metal is to bind carbon monoxide,^{93,102,103} while the reducible metal oxide, such as titanium dioxide or cerium oxide, binds and disassociates the water.¹⁰⁴⁻¹⁰⁶ Effective catalysts rely on cooperativity between the metal and metal oxide to catalyze the reaction.^{107,108} Pt-based catalysts have attracted interest due to high CO conversion¹⁰¹ compared to other transition metals, and there is evidence of an advantageous metal-support interaction with Pt, especially with TiO₂.¹⁰⁹⁻¹¹¹

An important operating variable in the WGS reaction is the water/carbon monoxide feed ratio, as it greatly impacts both conversion and the extent of coke formation. Higher water content in the feed increases conversion and decreases coking.¹¹² The effect of water concentration on surface chemistry is complex. For industrial Cu/ZnO catalysts, non-empirical rate laws are available^{113,114} for low water/carbon monoxide ratios, but these elementary rate laws did not fit behavior at higher water/CO ratios and empirical power-law equations are needed for accurate rate prediction.¹¹⁵ One reason for the large concentration effect is likely due to the site competition between water and WGS intermediates.¹¹⁶ The surface water concentration therefore seems to be able to affect the dominant WGS mechanism. Several WGS reaction pathways have been proposed including a simple redox reaction,¹¹⁷ and pathways involving carboxyl (CO₂H) or formate (HCOO) intermediates.^{118,119} On Pt¹²⁰ and Cu,¹²¹ carboxyl appears to be the key WGS intermediate. For both of these pathways, however, the activation and chemisorption of water has been shown to be kinetically important.¹²²

The common TiO₂ polymorphs are anatase and rutile. Anatase is preferred in many catalytic applications due to smaller particle sizes leading to larger specific surface areas. For photocatalytic purposes, it is tempting to suggest that rutile, the polymorph with the smaller band gap energy at 3.03 eV,¹²³ would be preferred. However anatase is the more effective photocatalyst despite the slightly larger band gap energy, 3.20 eV,¹²³ due to higher mobility of electron-hole pairs, leading to less bulk recombination.^{124,125} Anatase has been used as a support material in WGS reactions with a number of metals, including Pt, Pd, Rh, Ru, Au, Ag, and Cu.^{99-101,126-128}

Density functional theory (DFT) is a powerful computational tool that has been used to predict reaction mechanisms on catalyst surfaces. DFT has successfully given insight into activation energy barriers, reaction energies, binding energies, and binding geometries. Over the past decade, advances in methodology and computational power have allowed for accurate treatment of systems with localized electrons, expanding the scope of DFT into catalysis on metal oxide surfaces.¹²⁹⁻¹³² DFT has been applied to the mechanism of WGS on Pt¹²⁰ and Cu¹²¹ metal surfaces. Other works have focused on the Pt-metal oxide interfaces, where Pt₈/CeO₂(111) was found to disassociate water more exothermically than on Pt(111),¹⁰⁹ and on Pt₈/TiO₂(110) where a redox mechanism dominated over associative pathways at high and low temperatures.^{110,111} DFT has also been used to successfully describe the interaction of water with TiO₂ surfaces.¹³³⁻¹³⁶

In the present work, DFT is applied to investigate the role of water in the WGS reaction steps on the anatase TiO₂ (101) surface. The binding energies and structures for WGS reaction intermediates are calculated and minimum energy pathways for three possible WGS mechanisms are compared – direct CO oxidation, and associative mechanisms with carboxyl and formate intermediates. Beyond acting as a reactant, the effect of water as a non-innocent cocatalyst in the elementary steps of WGS is investigated. Cocatalytic water can play a larger role in the hydrogenation and dehydrogenation steps by acting as a bridging hydrogen acceptor/donor on the low density anatase (101) surface. Based on kinetic reaction barriers, the formate pathway is favored only slightly over the carboxyl pathway, with the direct oxidation pathway being unfavorable. These results help interpret the role of water and the oxide support for practical WGS catalysts consisting of a precious metal supported on anatase TiO₂.

4.2 Methods

Periodic DFT calculations were performed using the VASP code^{49,50} within the generalized gradient approximation (GGA-PBE)¹³⁷ using projector-augmented wave (PAW)^{52,53} potentials. Corrections to the on-site Coulomb interactions have been accounted for through the Hubbard term (DFT+U).¹³⁸ Dudarev's approach¹³⁹ was applied to increase the accuracy of the band gap and reaction kinetics with a $U_{\text{eff}} = 4$ for titanium atoms. This U_{eff} was chosen to align both the band gap and lattice parameters with experimental values as well as prevent electron delocalization.^{140–142} The single-electron wave functions were expanded using plane waves with an energy cutoff of 400 eV.

All oxide slabs were based on the (101) surface of anatase TiO_2 , and modeled by a (2×2) surface unit cell with four atomic layers for a total of 32 Ti atoms and 64 O atoms. The lattice constants used for anatase TiO_2 were $a = 3.784 \text{ \AA}$ and $c = 9.515 \text{ \AA}$.¹⁴³ A vacuum layer of 24 \AA was used to separate periodic images of the slab in the z direction (normal to the surface), and a dipole correction was applied and the electrostatic potential was adjusted to ensure that interaction between the surface slab and its periodic images was negligible.⁵⁵ The Brillouin zone was sampled using a $(2 \times 2 \times 1)$ Gamma-centered Monkhorst-Pack k-point mesh⁵⁶ following a convergence test for adsorbate binding energies with respect to sampling mesh size. All four layers were allowed to relax in all calculations.

Binding energy is calculated as $\text{BE} = E_{\text{ads}} - E_{\text{slab}} - E_{\text{gas}}$, where E_{ads} , E_{slab} , E_{gas} are the total energies calculated for the slab with the adsorbate, the clean stoichiometric slab, and the adsorbate in the gas phase, respectively. Formation energies were used in analyzing oxygen vacancy formation, defined as $\text{FE} = E_{\text{vo-slab}} + E_{\text{o-gas}} - E_{\text{slab}}$, where $E_{\text{vo-}}$

E_{slab} and E_{o-gas} were the total energies for the oxygen vacancy slab and the oxygen atom in the gas phase, respectively. The addition of a single adsorbate molecule to a slab with a (2×2) surface unit cell corresponds to $\frac{1}{4}$ monolayer (ML) adsorbate coverage. The nudged elastic band (NEB) method⁵⁷ was used to find transition states and calculate activation energy barriers.

4.3 Results and Discussion

4.3.1 Model Anatase TiO₂ (101) Surface

The most stable facet of anatase is the (101) face with one Ti-O bond cleaved per two surface titanium atoms. Cleaving along the (101) facet of anatase in the (2×2) unit cell used here breaks a total of eight Ti-O bonds, leaving eight under-coordinated surface atoms; four each of O and Ti. In addition there are twelve other surface atoms that are coordinatively saturated in the surface layer, with the same valency as their corresponding bulk atoms; eight O atoms and four Ti atoms.

Figure 1 labels the unique O and Ti atoms near the (101) surface of anatase in the (2×2) unit cell used in the calculations. Each unique atom is repeated four times in the (2×2) surface unit cell. Titanium atoms are labelled with two digits and oxygen atoms with three digits. The first layer has two unique titanium atoms, Ti_{#10} and Ti_{#11}, along with four unique oxygen atoms, O_{#100}, O_{#110}, O_{#101}, and O_{#111}. Ti_{#10} and O_{#100} are coordinatively unsaturated. O_{#111} is the only first layer atom that is not directly accessible from the surface.

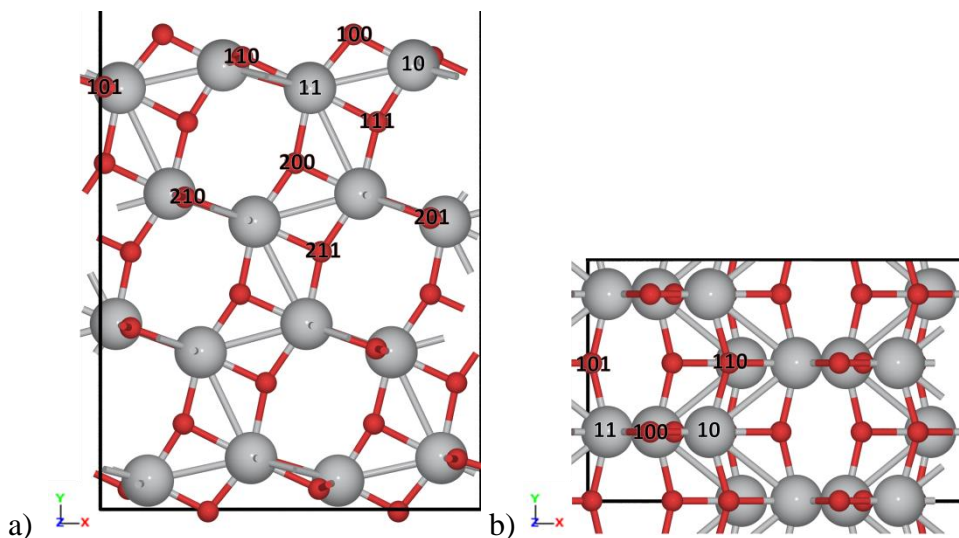


Figure 4.1 Anatase (101) unit cell used in calculations a) side view with near-surface unique atoms numbered and b) top view. Titanium atoms (grey) are labelled with two digits and oxygen atoms (red) by three digits. Edges of calculation unit cell are shown by black borders. Oxygen atoms O#100, O#101 and O#110 are accessible from the surface and O#100 is coordinatively unsaturated. Titanium atoms Ti#10 and Ti#11 are accessible from the surface with Ti#10 coordinatively unsaturated. Each unique atom repeats four times per unit cell. 0-1

Because hydrogen atoms are small enough to bind to subsurface oxygen atoms in interstitial positions, these sites themselves are labelled with four digits. The first three digits indicate the oxygen atom to which the hydrogen atom is bound. The fourth digit indicates the position of the hydrogen atom since it may take a position either “above” or “below” oxygen. A “0” indicates that the hydrogen atom is closer to the vacuum. For example, H_{#1100} and H_{#1101} are bonded to O_{#110}, where H_{#1100} is closer to the vacuum.

Oxygen vacancy (V_O) sites are named after the oxygen atom they displace, such that V_{O#100} denotes a vacancy formed by removing O_{#100}.

4.3.2 Binding of WGS intermediates

The WGS mechanism has been postulated to involve direct oxidation of CO to CO₂ or an associative mechanism where CO reacts with surface species to give carboxyl or formate intermediates which then dissociate to release CO₂. Even within these three pathways, there are numerous possible ways for the reaction to occur on a reducible

metal oxide surface. Possible elementary steps considered in the present study are summarized in Scheme 4.1.

For the direct oxidation of CO, there are several possible oxidants. For example, CO oxidation can occur via an oxygen adsorbate O^* (1), or via a lattice oxygen resulting in a vacancy V_O^* (2).

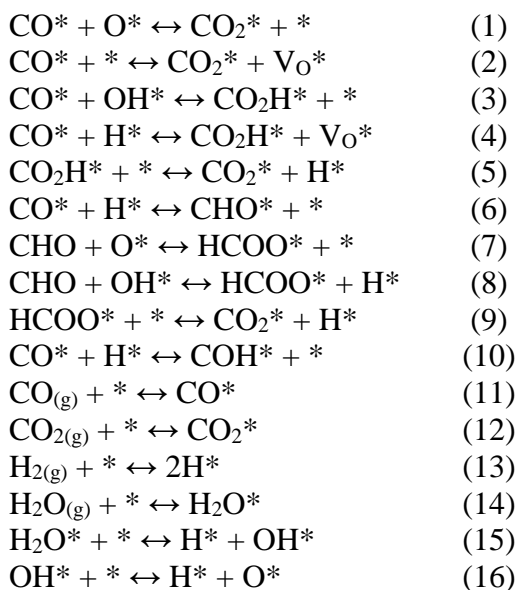
The associative carboxyl pathway involves CO reacting with a hydroxyl group to form a carboxyl intermediate CO_2H^* . This mechanism can either involve an OH^* adsorbate species (3) or can involve a hydroxyl group where a proton is bonded to a lattice oxygen atom, resulting in a lattice oxygen vacancy (4). Subsequent dehydrogenation of the carboxyl intermediate yields $CO_{2(g)}$ (5).

The association formate pathway involves the initial formation of an intermediate by reaction of CO^* with a hydrogen adsorbate H^* . Hydrogenation occurs either at the C-position, making formyl CHO^* (6), or at the O-position, making hydroxymethylidyne, COH^* (10). Both of these mechanisms were considered initially, and (10) was excluded from further consideration due to the large difference in reaction energies starting from $CO^* + H^*$. The formation of formyl (6) on anatase (101) was calculated to be 0.73 eV downhill, making it thermodynamically favorable, while the formation of hydroxymethylidyne (10) was 0.85 eV uphill. With a 1.58 eV difference between the isomers, pathways involving COH were eliminated from further consideration.

Formyl oxidation gives formate, and possible oxidants include adsorbed oxygen (7) and hydroxyl (8). Formate can then cleave the C-H bond to give CO_2^* and H^* (9).

The adsorption/desorption of reactants and products are considered in steps (11-14). The role of water may be as a source of OH* or H* in the preceding steps, so partial dissociation of molecularly adsorbed water is included in the mechanism (15), and for steps where atomic oxygen adsorbate is invoked, total dissociation of water to atoms is included (16).

The binding energies and geometries of the intermediates in these elementary reactions are discussed in Sections 4.3.2.1-4.3.2.5



Scheme 4.1 Elementary steps in WGS considered in the present study.

In the discussion that follows, the * notation to indicate an adsorbed species (e.g. CO*) is omitted (e.g. CO) and all species are in the adsorbed state unless it is specifically indicated that they are in the gas phase (e.g. CO_(g)).

4.3.2.1 Hydrogen Adsorption

Hydrogen atoms were found to bind only to oxygen atoms. Attempts to form Ti-H bonds when setting up calculations failed to find any local minima where such a bond

was possible. The binding energies of all stable binding sites are given in Table 4.1. The strongest hydrogen binding site, H_{#1000} (Figure 4.2), found at the under-coordinated surface oxygen atom O_{#100}, was 0.6 eV stronger than at any other O atom. There was little variance between the hydrogen binding energies to fully coordinated O atoms near the surface compared to those deeper into the bulk of the slab, with most falling between -1.51 eV and -1.69 eV. Minor exceptions were found with H_{#1101}, which bound hydrogen weaker (-1.22 eV) due to the placement of the binding site between two undercoordinated Ti atoms, and H_{#2000}, which bound hydrogen slightly stronger (-1.80 eV). A major exception was found at H_{#1011} where no stable structure was found.

Because the hydrogen atom is added to the TiO₂ surface as a proton and an electron, calculating the charge densities on the adjacent atoms to the adsorbates can confirm relative electronegativities of the surface atoms relative to the adsorbates. To estimate charge densities, the partial occupancy of orbitals by electrons was used as a first order measure of electron localization. While this method perhaps does not provide quantitative differentiation between charges on similar atoms, it provides a clear picture of charge transfer from an adsorbate to the surface. In the case of the hydrogen atom, Ti⁴⁺ centers in the TiO₂ would be expected to be more electronegative than a proton, and charge transfer from the hydrogen to the Ti atom is expected. This is exactly what was observed in the calculations, with a shift of approximately 0.85 electrons from hydrogen to titanium, leading to a +3.15 charge on the Ti center in the newly formed Ti-O-H group. This distribution is consistent with describing the adsorbate as a proton with a reduced Ti³⁺, or as a resonance structure with primarily H⁺/Ti³⁺ character.



Table 4.1 Hydrogen binding energies in eV, and localized charge on adjacent Ti atoms.0-1

Site	BE (eV)	Ti charge ^d	Site	BE (eV)	Ti charge ^d
1000^a	-2.39	+3.13	2000	-1.80	+3.16
1010^b	-1.58	+3.14	2010	-1.62	+3.16
1011^b		^c	2011	-1.63	+3.16
1100^b	-1.51	+3.13	2100	-1.51	+3.17
1101^b	-1.22	+3.12	2101	-1.57	+3.17
1110^b	-1.69	+3.10	2110	-1.66	+3.15

^a Coordinatively unsaturated oxygen atom site. ^b Coordinatively saturated surface atom. ^c No stable structure found. ^d Charge on Ti atom calculated from orbital electron occupancy.

4.3.2.2 Water Adsorption

Two modes of water adsorption were considered. Physisorbed water, H₂O_(p), represents molecular adsorption of a water molecule on the TiO₂ surface. Activation of surface water leads to O-H bond cleaving, resulting in chemisorbed water, H₂O_(c), an OH/H pair on the surface. The best binding geometries for both water binding modes are shown in Figure 4.2. In the discussion that follows, chemisorbed water refers to OH and H coadsorbed on the same slab in a calculation.

In H₂O_(p), the oxygen atom interacts with the coordinatively unsaturated Ti_{#10} atom with the water molecule oriented parallel to the surface and a binding energy of -0.87 eV (Scheme 1.14). In chemisorbed water, the OH and H fragments preferred to bind to the coordinatively unsaturated Ti_{#10} and O_{#100} (at the H_{#1000} position) sites to form two Ti-O-H groups sharing a Ti atom. Separating the two OH groups to distant sites on the same surface was +0.19 eV uphill, indicating that there is significant hydrogen bonding between the geminal groups. Unlike with H adsorption, no charge transfer to Ti was found, and instead heterolytic O-H bond cleavage formed an OH⁻/H⁺ pair. Despite hydrogen bonding, water chemisorption was +0.22 eV unfavorable compared to physisorption (Scheme 4.1.15), with an overall binding energy of -0.65 eV. This result

shows that new bonds formed with the anatase (101) surface are weaker than the OH bond in water. Prior studies have shown that water dissociation on the clean and defect-free anatase (101) surface is an activated process,^{133-135,144} which supports the 0.22 eV positive reaction energy from physisorbed water to chemisorbed water reported here. To investigate the barrier for water dissociation further, the transition state energy between physisorbed and chemisorbed water was calculated, giving an activation energy barrier of 0.44 eV for water activation. This value is small enough that water activation may be trivial under temperatures relevant for WGS reaction.

In water chemisorption, the OH group is reduced to OH⁻ as opposed to the reduction of Ti⁴⁺ to Ti³⁺ observed with H atom adsorption. It is evident that the OH group is therefore more electronegative than Ti⁴⁺. This creates a problem when attempting to adsorb OH as a lone adsorbate, in the absence of an electron donor. In chemisorbed water, H acts as the electron donor. Calculations of OH adsorption alone showed that it remains as ·OH, a high energy radical. It takes the same Ti_{#10} site without charge transfer. The calculated binding energy of ·OH, -1.08 eV, is misleading out of context. This value is calculated relative to OH in vacuum. The energy to generate adsorbed OH from water gives a more meaningful figure. The energy to generate an isolated ·OH from chemisorbed water involves two steps. First, the hydrogen bonding between the surface hydroxyls formed from H⁺ and OH⁻ is broken by moving the species farther apart within the same calculation slab, resulting in a 0.19 eV penalty. In this geometry, the H⁺/OH⁻ nature of the adsorbates is conserved. Separating the two adsorbates to separate calculation slabs (so-called “infinite separation”) breaks any possible interaction between the adsorbates; the two species are now H⁺ as in H_{#1000} and ·OH. This reaction is

equivalent to moving an electron from the more electronegative OH^- to less electronegative Ti^{4+} , and is therefore substantially uphill at +2.37 eV. This energy state may not be easily reachable during thermal catalysis. It may be relevant in photocatalysis, where the high energy input may be provided when photon energy equivalent to the band gap energy of anatase is absorbed.^{145,146} Photoinduced water dissociation on anatase (101) has been experimentally observed.¹⁴⁴

As $\cdot\text{OH}$ from water is likely absent during thermocatalytic reaction without light input, (3) from Scheme 4.1 that relies on isolated OH species will be removed from consideration. However, reaction with OH^- coadsorbed with H^+ (i.e. $\text{H}_2\text{O}_{(\text{c})}$) will be considered instead. This is the same logic by which other elementary reactions that can be written with OH as a reactant have been omitted from Scheme 4.1.

In Scheme 4.1, (1) and (7) are written with atomic oxygen as an adsorbate. Similar to OH, O is more electronegative than Ti^{4+} , leading to it adsorbing as a high energy radical (Figure 4.2). Formation of an isolated oxygen diradical at the $\text{Ti}_{\#10}$ site from O-H bond cleavage in $\cdot\text{OH}$ would require an additional +1.34 eV energy input, or +3.71 eV relative to $\text{H}_2\text{O}_{(\text{c})}$. This large energy is beyond the band gap energy of anatase, and hence such a species is not expected in photocatalysis nor thermocatalysis. Instead, coadsorption of an O atom and two H atoms was considered. This led to the expected formation of anionic O^{2-} and two protons. The energy required to form this state by cleaving the final O-H bond in chemisorbed water (Scheme 1.16) was +0.65 eV. The barrier for this reaction was calculated as 0.88 eV.

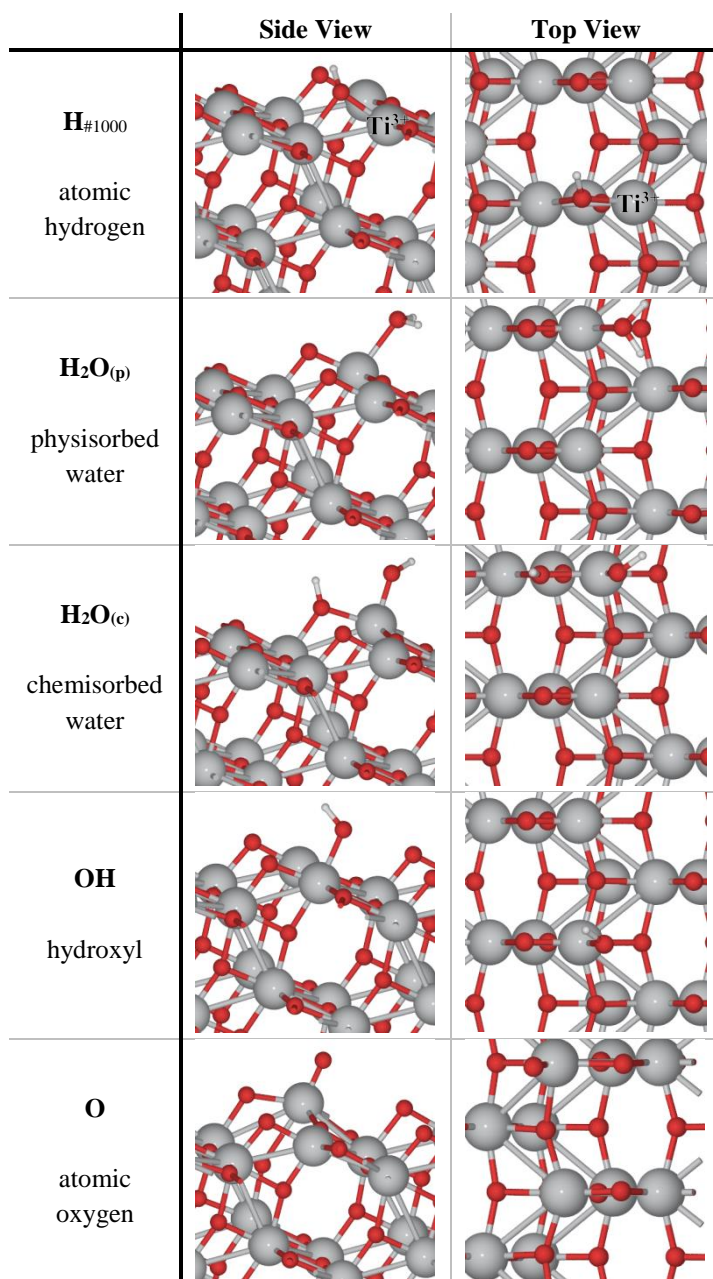


Figure 4.2 Best binding orientations of adsorbates on anatase (101), including physisorbed water, H₂O_(p), and chemisorbed water, H₂O_(c) water. Reduced Ti³⁺ center is labelled in H_{#1000}. H adsorbs as a proton, H₂O_(c) as a proton/hydroxide anion pair, OH and O as radicals, and H₂O_(p) adsorbs molecularly.0-2

4.3.2.3 Cationic Adsorbates

As was found with H atom adsorption, adsorbates less electronegative than Ti⁴⁺ ionized upon adsorption, and the calculated electron orbital populations showed a transfer

of charge from the newly formed cation to a newly reduced geminal Ti atom. The formyl (CHO) and carboxyl (CO₂H) adsorbates were found to transfer an electron to Ti, such that they could be described as cations with nearby Ti³⁺ centers. The binding energies and structures are given in Table 4.2 and Figure 4.3 respectively. The binding geometries of both of these adsorbates were similar, with the carbonyl group in a similar orientation. The carbon atom bonded to undercoordinated O_{#100} and the carbonyl oxygen bonded to Ti_{#10}. This orientation left the remaining part of the adsorbate (H for formyl and OH for carboxyl) oriented facing nearly perpendicular from the surface.

Table 4.2 Binding energies of molecular and WGS intermediate species on anatase (101) in eV0-2

Species	BE
H₂O_(p)	-0.87
H₂O_(c)^a	-0.65
OH^b	-1.08
O^b	-2.05
CHO	-2.29
CO₂H	-2.27
HCOO+H^c	-3.41
CO	-0.34
CO₂	-0.20

^a Equivalent to OH coadsorbed as an anion with a proton, ^b Radical adsorbates, ^c Coadsorbed as anion and a proton

4.3.2.4 Anionic Adsorbates

In Section 4.3.2.2 the effect of electronegativity on binding interaction for OH and O species was discussed. Without an electron donor, these species cannot be reduced and are adsorbed as high energy radicals. In the WGS reaction, formate (HCOO) is another such intermediate which would also form a high energy radical without an electron donor. While such free radicals may be relevant during photocatalysis, they are not expected during thermal catalysis in the WGS reaction.

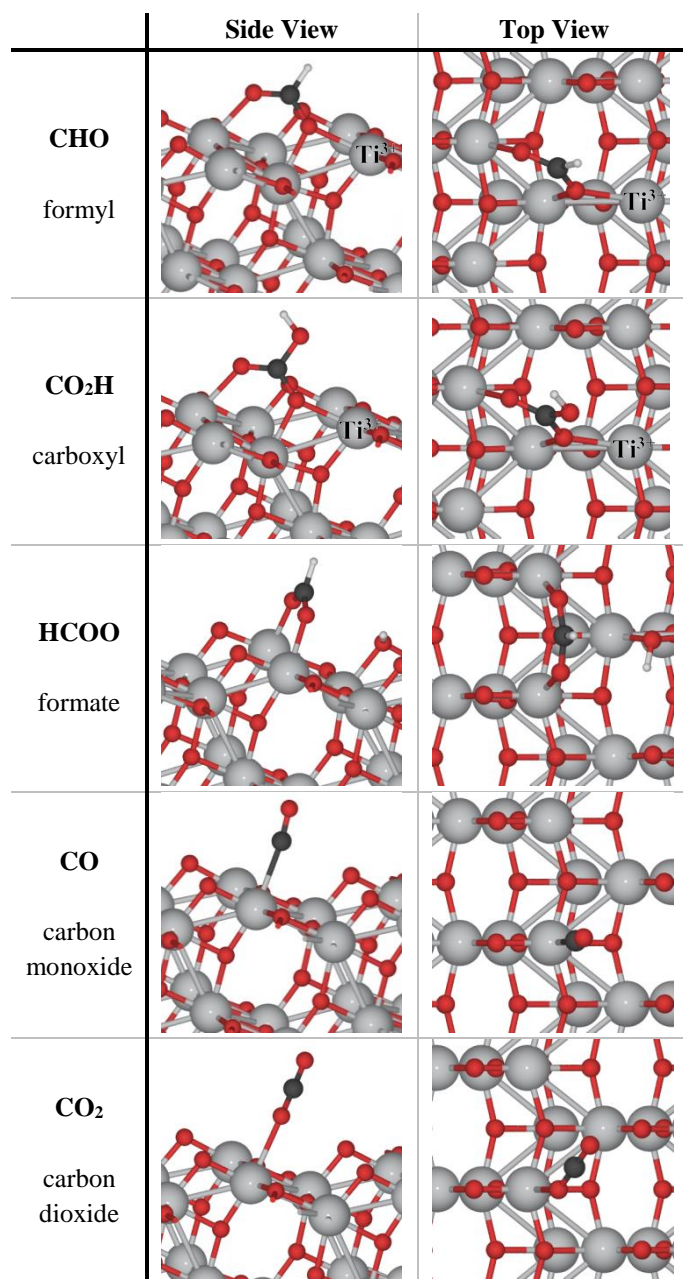


Figure 4.3 Best binding orientations of CH_xO_y species on anatase (101). Reduced Ti³⁺ centers are labelled where present. CHO and CO₂H adsorb as cations, HCOO adsorbs as an anion and is coadsorbed with a proton, and CO and CO₂ adsorb molecularly. 0-3

To calculate adsorbed states for formate, a hydrogen atom was coadsorbed on the same slab in all calculations involving formate. As with chemisorbed water, H acted as an electron donor to become an adsorbed proton, and the resulting anionic formate species adsorbed across two low-coordinate Ti-atom atop sites (Figure 4.3). The coadsorbed proton can also be seen binding to an adjacent oxygen site. The calculated binding energy

of -3.41 eV can therefore be thought of as the chemisorption energy of a formic acid molecule as an anion/proton pair.

4.3.2.5 Molecular Adsorbates

The molecular adsorbates CO and CO₂ were found to interact very weakly with the surface, with binding energies of -0.34 eV and -0.20 eV respectively. Both species adsorb to a Ti top site (Figure 4.3) albeit through different atoms. CO bound through its carbon atom, with the C=O bond perpendicular to the surface. The interaction of CO₂ with the surface was through the oxygen atom, with the molecule oriented perpendicular to the surface. Among close-shelled species, physisorbed water binds to the same open coordination site significantly stronger, and may be expected to compete with adsorbed CO and CO₂.

4.3.3 Oxygen Vacancies

The oxygen atoms in the surface of anatase are known to be highly reactive and participate in chemical reactions as oxidizing agents.^{147,148} The removal of reactive lattice oxygen through chemical reaction creates an oxygen vacancy, V_O. To account for the role of lattice oxygen in oxidation steps, the formation of oxygen vacancies from the stoichiometric TiO₂ surface was investigated. The formation energies for V_O in different lattice positions are given in Table 4.3. The under-coordinated O_{#100} was found to be the easiest to remove as it already had fewer Ti-O bonds to cleave. Surface O_{#110} was more difficult to remove than bulk oxygen, likely because it was bonded to multiple under-coordinated Ti atoms, resulting in stronger Ti-O bonds. Saturated oxygen sites at the near-surface (O_{#101}) and those in more bulk-like positions (O_{#201}, O_{#210}, O_{#211}) showed similar vacancy formation energies.

Following removal of an oxygen atom, charge neutrality in the sub stoichiometric oxide structure was maintained as two Ti centers adjacent to the oxygen vacancy were reduced, and can be summarized as follows.

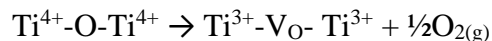


Table 4.3 Oxygen vacancy formation energies in eV, identified by the O atom removed. Oxygen is removed as $\frac{1}{2}\text{O}_{2(\text{g})}$. 0-3

V_o	
Site	FE
100^a	4.22
101^b	5.13
110^b	5.57
111	^c
200	4.83
201	5.08
210	5.24
211	5.11

^aCoordinatively unsaturated oxygen atom site. ^b Coordinatively saturated surface atom. ^c A vacancy “placed” at this site “migrates” to 100 – i.e. the O atom at 100 moves to 111 and V_{o#100} forms instead.

4.3.4 Elementary Reactions in WGS Reaction Mechanism

Based on the results of the calculations for binding structure of the anionic adsorbates, it becomes clear that some of the elementary steps in Scheme 1 cannot proceed as written. (1) and (7) invoke isolated oxygen atoms, and (3) and (8) use OH. Reactions involving these intermediates can therefore be excluded from further consideration, except heavily modified to consider anionic species coadsorbed with protons. A similar modification is required for steps involving formate (7-9), where coadsorbed protons are included in all further discussion. Apart from chemisorbed water and coadsorbed formate/proton, all other species and energies in the following discussion report species at infinite separation, isolated on separate calculation slabs. Reaction energies and activation energies for elementary steps are summarized in Table 4.4.

The direct oxidation of CO by atomic O (1) can be excluded on energetic arguments. A transition state search was performed for this reaction regardless, but no viable mechanism was found with the current methods. Oxidation of CO by lattice oxygen (2) was feasible however. The reaction was calculated to be +1.10 eV uphill with a 1.86 eV barrier, reflecting the difficulty in forming oxygen vacancies.

Table 4.4 Binding energy of chemisorbed water with and without water on the both sides of the slab 0-4

	Reaction	ΔE	E_a
(2)	$\text{CO} \rightarrow \text{CO}_2 + \text{V}_\text{O}$	1.10	1.86
(3) ^b	$\text{CO} + \text{H}_2\text{O}_{(\text{c})} \rightarrow \text{CO}_2\text{H} + \text{H}$	-0.23	1.32
(5)	$\text{CO}_2\text{H} \rightarrow \text{CO}_2 + \text{H}$	0.04	0.48
(6)	$\text{CO} + \text{H} \rightarrow \text{CHO}$	-0.73	4.23
(8) ^b	$\text{CHO} + \text{H}_2\text{O}_{(\text{c})} \rightarrow \text{HCOO} + 2\text{H}$	-0.33	0.92
(9) ^c	$\text{HCOO} + \text{H} \rightarrow \text{CO}_2 + 2\text{H}$	0.87	2.23
(15)	$\text{H}_2\text{O}_{(\text{p})} \rightarrow \text{H}_2\text{O}_{(\text{c})}$	0.22	0.44
(16)	$\text{H} + \text{OH} \rightarrow 2\text{H} + \text{O}$	0.65	0.88
	$\text{V}_\text{O} + \text{H}_2\text{O}_{(\text{p})} \rightarrow 2\text{H}$	-1.07	2.32
	$\text{V}_\text{O} + \text{H}_2\text{O}_{(\text{c})} \rightarrow 2\text{H}$	-1.29	0

ΔE is the energy of reaction. E_a is the activation energy barrier. All species are surface species at infinite separation except as follows: $\text{H}_2\text{O}_{(\text{c})}$ which is OH+H coadsorbed on the same slab, and $\text{HCOO}+\text{H}$ which are coadsorbed on the same slab. ^a Without cocatalytic water. ^b Modified from Scheme 1 to use anionic OH^- from chemisorbed water. ^c A spectator hydrogen atom is included in the calculation as formate must be coadsorbed with a proton for charge balance.

The healing of these oxygen vacancies to complete a catalytic cycle was investigated. The reaction of an oxygen vacancy with chemisorbed water was found to be 1.29 eV downhill and proceeded with zero activation energy barrier. In the reaction, the OH^- anion moves to the vacancy, and enters the vacant lattice position, such that the final structure is equivalent to two adsorbed protons. In effect, the only barrier to healing oxygen vacancies with chemisorbed water was the barrier of 0.22 eV to form chemisorbed water (15). The direct reaction between physisorbed water and oxygen vacancies was far less favorable. Though the reaction energy was 1.07 eV downhill, the minimum energy pathway possessed a 2.32 eV activation energy barrier. Chemisorbed water is highly favored as an intermediate in healing oxygen vacancies.

The minimum energy pathway for the direct CO oxidation reaction is shown in Figure 4, where it is compared to the associative carboxyl and formate pathways. All three pathways share the same initial steps involving the adsorption of carbon monoxide, and the activation of physisorbed water to form chemisorbed water. The direct CO oxidation pathway then involves the oxidation of CO to CO₂ with lattice oxygen, followed by healing the oxygen vacancy with chemisorbed water. The final step is desorption of CO₂ and the associative adsorption of H₂. As anatase TiO₂ is known not to possess the proper active sites for hydrogen gas evolution,¹⁴⁹ the H-H bond formation mechanism was not investigated on anatase (101). In the direct CO oxidation pathway, the highest apparent barrier is for the oxidation step, forming an oxygen vacancy, +0.87 eV relative to the reactants CO_(g) and H₂O_(g). In constructing the potential energy surfaces in Figure 4.4, an arbitrary choice was made to chemisorb water before the CO oxidation step. The effect is to raise the reactant state energy for that step relative to the gas phase by the chemisorption reaction energy, 0.22 eV. This also raises the apparent activation energy barrier by the same amount, so a barrier of 0.65 eV relative to the gas phase can be obtained instead by reversing the order of the oxidation and chemisorption steps. This does not change the comparison of the pathways, as all pathways share the same initial steps. Only the direct oxidation pathway does not require chemisorption before the initial high barrier, and may optionally place this step afterwards. The associative pathways involve reactions with chemisorbed water immediately, so their barriers are not affected.

Scheme 4.1 identified two possible routes for CO oxidation in the carboxyl pathway requiring association between CO and an OH group to form CO₂H. Step (3) as written has already been excluded as it involves high energy OH radical. Instead,

alternate OH groups can be considered as reactants in the carboxyl pathway. Step (4) involves an OH group consisting of a lattice-oxygen bonded to a proton. Reaction with CO, resulting in the formation of an oxygen vacancy, was calculated to be 1.06 eV uphill, once again reflecting the energetic penalty for forming oxygen vacancies. By contrast, modifying step (3) to involve reaction with anionic OH^- from chemisorbed water instead was -0.23 eV downhill. The reaction requires CO to be coadsorbed with $\text{H}_2\text{O}_{(\text{c})}$, which further weakens the already weak interaction between CO and the TiO_2 surface. The resulting activation energy barrier for the reaction was 1.32 eV, of which 1.14 eV was the penalty relative to infinite separation of coadsorbing CO and chemisorbed water.

The next step following carboxyl formation is carboxyl dehydrogenation (5), where the O-H bond is cleaved, yielding CO_2 and a second proton. This reaction was facile compared to the previous step, with a nearly thermoneutral reaction energy of +0.04 eV and a low barrier of only 0.48 eV. This meant that the reaction of CO with OH^- was the highest apparent activation energy barrier in the carboxyl pathway, 0.33 eV relative to the gaseous reactants (Figure 4.4).

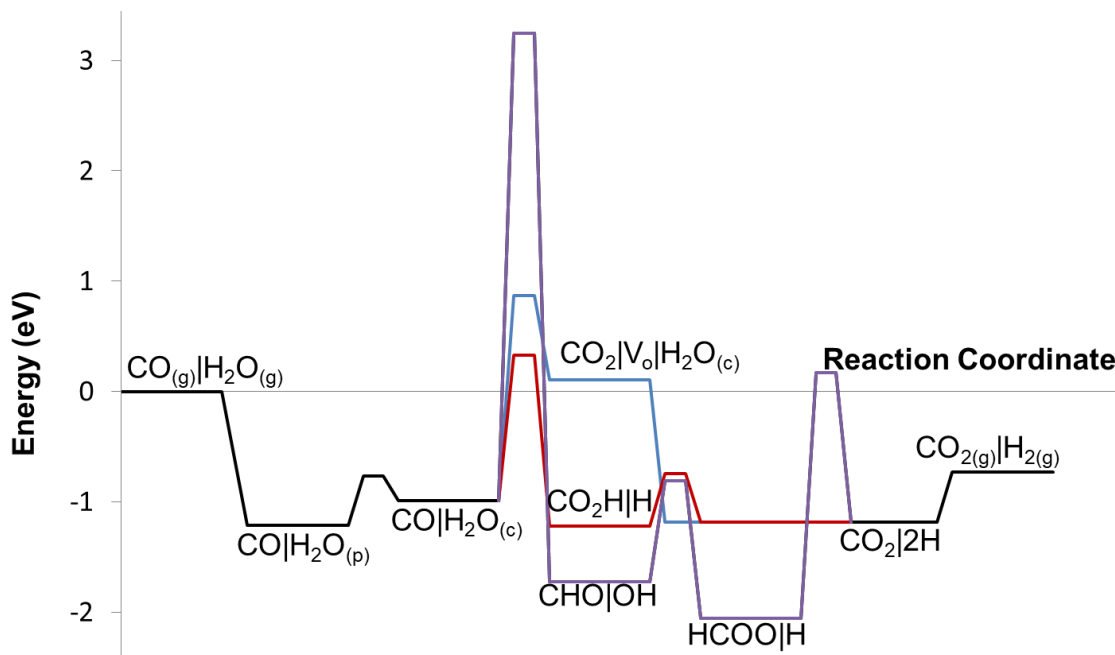


Figure 4.4 Reaction pathways for direct CO oxidation (blue), associative carboxyl (red), and associative formate (purple) pathways. Common steps (CO and H₂O physisorption, water activation to form H₂O(c), and CO₂ and H₂ desorption) are shown in black. All species are surface species at infinite separation except gases as indicated and as follows: H₂O(c)↔ is OH+H coadsorbed on the same slab, HCOO+H are coadsorbed on the same slab, and CHO+OH are coadsorbed on the same slab. 0-4

The formate pathway consists of three steps from Scheme 4.1: CO hydrogenation to formyl (6), formyl oxidation by OH (8), and formate dehydrogenation (9). As before, OH⁻ from chemisorbed water was substituted for OH in (8), and the formate state in (8) and (9) involve a coadsorbed proton. The first step, forming a C-H bond between CO and H was found to be prohibitively difficult. Although the reaction energy was -0.73 eV, the barrier was 4.23 eV (3.24 eV above the gaseous reactants). The final formate dehydrogenation step was similarly disadvantaged, with a barrier of 2.23 eV. These two steps illustrate how difficult hydrogen transfer reactions on anatase (101) can be, which is discussed in further detail in the following section on the role of cocatalytic water.

The modified formyl oxidation step (8) had a barrier of 0.92 eV and an unexpected mechanism. The minimum energy pathway from formyl to formate in the presence of

chemisorbed water is to strip a lattice oxygen atom to oxidize formyl, partly forming an oxygen vacancy, and healing the vacancy immediately with the coadsorbed OH species, all in a single step. Attempts to divide the mechanism into separate vacancy formation and removal steps failed, suggesting a concerted mechanism. No stable intermediate consisting of coadsorbed formate and chemisorbed water at or near an oxygen could be found either.

In the unassisted reaction pathways in Figure 4.4, the formate pathway is considerably unfavorable, while the carboxyl pathway has the lowest apparent activation energy barrier, 0.54 eV lower than that for the direct CO oxidation pathway.

4.3.5 Cocatalytic Water

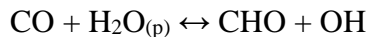
In the WGS reaction steps on anatase TiO₂ (101), hydrogen transfer reactions are particularly difficult. This is at least in part due to the large distances spanned by the atoms that move in the transition states, with no transition state stabilization provided by interactions with the surface. This is illustrated in Figure 5 using the very difficult CO hydrogenation step. In the unassisted pathway, the transition state structure involves a hydrogen atom that is between a bridging lattice oxygen (initial state structure) and the carbon to which it will bind in the formyl adsorbate (final state structure). What is remarkable about this transition state structure is that the hydrogen atom is very far from both the initial state and the final state, which are 3.8 Å away from one another. There is no binding site located between the initial and final state structures to provide any stabilization for the transition state. Therefore, the hydrogen atom is essentially behaving as a gas, having desorbed from the bridging oxygen site, diffusing through the vacuum, and adsorbing at the carbon position of the adsorbed CO molecule. This gas-like state

leads to the very high activation energy barrier of 4.23 eV for this elementary step. Based on this step alone, the formate pathway is uncompetitive. Note that the binding geometry of CO in the initial state is very different from the best binding geometry of CO in Figure 3. Instead of binding solely through a Ti-C interaction perpendicular to the surface when adsorbed alone, after coadsorbing H the CO molecule rotates to increase its interactions with the surface prior to the hydrogen transfer step. In this state, the CO has C-O, C-Ti, and O-Ti interactions with the surface. This state is higher in energy than the structure for isolated CO, but only by 0.34 eV, so the structural change is a very small fraction of the 4.23 eV barrier for the reaction.

Under normal reaction conditions, it is reasonable to expect that physisorbed or chemisorbed water may be adsorbed near the reactants of a hydrogen transfer reaction such as CO hydrogenation. If situated on an adjacent site, these waters can potentially participate in the reaction, acting as hydrogen acceptors and donors. One such arrangement is depicted in the initial state for the cocatalytic water case in Figure 4.5. In this case, a water molecule is physisorbed to Ti_{#10}, which displaces the CO to the adjacent oxygen atom. This destabilization of adsorbed CO is costly – this configuration is 1.27 eV uphill from isolated adsorbates. However, from this position, one of the protons of the water molecule is positioned facing the CO carbon. In the transition state, the two adsorbed molecules bend towards each other and a hydrogen transfer occurs. The water molecule is stabilizing the hydrogen that is being transferred, reducing the activation energy barrier significantly. The total barrier, including the CO displacement effect, was calculated to be 1.45 eV, significantly lower than the barrier of 4.23 eV for the unassisted

pathway. Note that the final state structure has formyl, a cationic adsorbate, coadsorbed with hydroxide, which therefore takes an anionic structure.

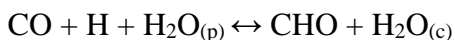
The reaction depicted as catalytic water in Figure 5 has the stoichiometry



To make this reaction more directly analogous to (6), an adsorbed hydrogen is added to both sides of the reaction. Using the notation of Scheme 1, the overall stoichiometry can then be written as:



As OH must be coadsorbed with a cationic adsorbate such as CHO or H, pairing it with H can be recognized as chemisorbed water. Using the notation of Table 4, the reaction is then:



This means that the net reaction energy of (6') must be 0.22 eV less favorable than (6), as it includes the energy required to chemisorb water. This can be seen comparing Tables 4 and 5. The unassisted mechanism is -0.73 eV, and the cocatalytic water mechanism is -0.51 eV. As water is not consumed in the reaction, only reversibly chemisorbing in the net reaction, this reaction can be said to be cocatalytic in water.

Despite the significant reduction in barrier for CO hydrogenation, the energetic penalty for displacing CO makes the value of 1.45 eV still large. However, it is now of similar magnitude to the barriers for direct CO oxidation (2) and CO hydroxylation to carboxyl (3) of 1.86 eV and 1.32 eV. To better understand if this makes the formate pathway more competitive than it was without cocatalytic water, the potential energy surfaces for the water-assisted mechanisms in Figure 6 were constructed. Included in

these mechanisms are additional elementary steps where adsorbed water may play a role in lowering the activation energy barriers for hydrogen transfer reactions.

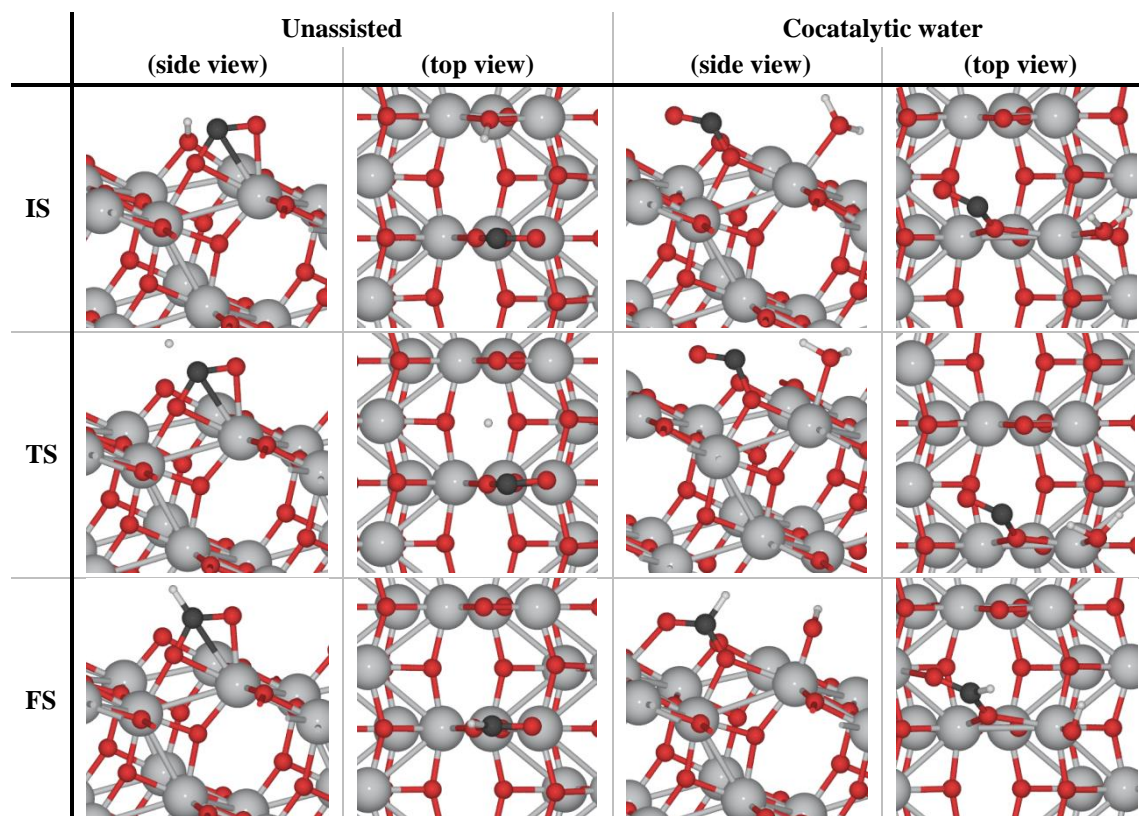
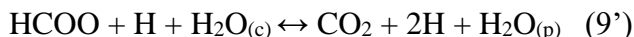
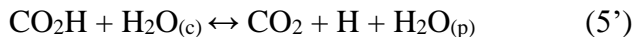


Figure 4.5 CO hydrogenation mechanism unassisted (without participation of a cocatalytic water molecule) and with cocatalytic water. The physisorbed water molecule acts as a hydrogen donor, bridging the spatial gap between donor and acceptor and reducing the activation energy barrier relative to the unassisted case. IS is the initial coadsorbed state, TS is the transition state, and FS is the final coadsorbed state. 0-5

The two additional reactions where hydrogen transfer benefitted from cocatalytic water were carboxyl dehydrogenation and formate dehydrogenation. The new reaction stoichiometries including cocatalytic water are given as (5') and (9') below. A spectator hydrogen atom is included in (9') as formate must be coadsorbed with a proton for charge balance. Of all the elementary reactions considered in the three WGS pathways, these were the only ones that involved hydrogen transfer. The reaction of formyl with

hydroxide to give formate does not involve hydrogen transfer, since the mechanism discussed in Section 3.4 was found to involve lattice oxygen instead. The reaction energies and activation barriers for all cocatalytic water steps are summarized in Table 5.



Unlike in CO hydrogenation, (5') and (9') are dehydrogenation steps. As such, the role of water is to act as the hydrogen acceptor instead of the hydrogen donor. Chemisorbed water was found to be well suited for this role. When coadsorbed on an adjacent site, OH^- was able to bend towards the donor hydrogen in carboxyl or formate, and hydrogen transfer was more facile in this stabilized transition state structure relative to the unassisted mechanism. As hydrogenation and dehydrogenation are microscopic reverses, the role of cocatalytic water on the reactions is the same in all cases, and differs only in the details. During dehydrogenation steps, chemisorbed water is converted to physisorbed water, so the reaction energies are 0.22 eV more favorable with cocatalytic water compared to the unassisted mechanisms, and the reverse effect is seen in hydrogenation.

In formate dehydrogenation, competition for binding sites displaces formate from its preferred bidentate geometry atop two Ti atoms, much as CO was displaced in (6'). The effect is small as when OH takes one of the two top sites, formate takes a monodentate binding mode at only a 0.27 eV penalty relative to isolated adsorbates. The transition state stabilization by having OH act as the hydrogen acceptor reduced the barrier by 0.31 eV relative to the unassisted reaction.

Unassisted carboxyl dehydrogenation was already calculated to be nearly thermoneutral (+0.04 eV) with a relatively small barrier (0.48 eV). The addition of physisorbed water formation therefore made the net reaction exothermic (-0.18 eV). The coadsorption of water with carboxyl was exothermic by -0.40 eV relative to the isolated species due in part to hydrogen bonding between the adsorbed species. The transition state energy was calculated to be 0.32 eV above the energy of the coadsorbed reactants, which is lower than the 0.48 eV barrier of the unassisted mechanism. This transition state is 0.08 eV below the energy of the reactants at infinite separation, so the reaction appears to have no barrier relative to isolated species.

Table 4.5 Reaction energies and activation energy barriers for elementary steps in WGS reaction mechanism where water acts as a cocatalyst. 0-5

	Reaction	ΔE	E_a
(5')	$\text{CO}_2\text{H} + \text{H}_2\text{O}_{(\text{c})} \rightarrow \text{CO}_2 + \text{H} + \text{H}_2\text{O}_{(\text{p})}$	-0.18	0 ^b
(6')	$\text{CO} + \text{H} + \text{H}_2\text{O}_{(\text{p})} \rightarrow \text{CHO} + \text{H}_2\text{O}_{(\text{c})}$	-0.51	1.45
(9') ^a	$\text{HCOO} + \text{H} + \text{H}_2\text{O}_{(\text{c})} \rightarrow \text{CO}_2 + 2\text{H} + \text{H}_2\text{O}_{(\text{p})}$	0.66	1.92

ΔE is the energy of reaction in eV. E_a is the activation energy barrier in eV. All species are surface species at infinite separation except as follow: $\text{H}_2\text{O}_{(\text{c})}$ which is $\text{OH}+\text{H}$ coadsorbed on the same slab, and $\text{HCOO}+\text{H}$ which are coadsorbed on the same slab. ^a A spectator hydrogen atom is included in the reaction as formate must be coadsorbed with a proton for charge balance. ^b The coadsorbed reactants were -0.40 eV favorable compared to infinite separation, so the transition state energy +0.32 eV relative to the coadsorbed state was still below the infinite separation state energy by -0.08 eV. The reaction is therefore reported having 0 eV barrier relative to isolated species.

The ability of adsorbed water to lower the activation energy barriers of key steps in the WGS reaction mechanisms leads to new minimum energy pathways as shown in Figure 6. These were constructed with the cocatalytic water already chemisorbed. This preserves the comparison with Figure 4, as both include the heat of adsorption only once in the thermodynamics of the catalytic cycle. This also represents reaction on surfaces where adsorbed water may be more abundant, such as for high water/carbon monoxide ratios, whereas the unassisted mechanism represents reaction on surfaces with less adsorbed

water such as low water/carbon ratios. Since the unassisted pathways in Figure 4 place the water activation step first, the subsequent states are all raised in energy by 0.22 eV relative to the gas phase, the water dissociation energy. In Figure 6, chemisorption of water may occur at any point, and so it has been placed at the end of the catalytic cycle. Therefore, the heat of dissociation does not impact the energy of these states relative to the gas phase.

The direct CO oxidation mechanism did not involve any hydrogen transfer steps, and so there is no impact of cocatalytic water. The highest barrier is still the CO oxidation step, although moving the chemisorption of water to later in the mechanism makes it 0.65 eV above the gas phase energy for the reactants, 0.22 eV less than when water chemisorption was the first step.

The hardest step of the associative carboxyl pathway was the formation of carboxyl (3), which did not involve hydrogen transfer. As a result, the transition state for this highest barrier in the water-assisted mechanism was unchanged, although moving water chemisorption to the end of the mechanism appears to reduce the barrier by 0.22 eV relative to the gas phase, as with the CO oxidation mechanism. This reaction consumes chemisorbed water. In the unassisted pathway, the next step is dehydrogenation with a 0.48 eV barrier relative to adsorbed carboxyl. In the cocatalytic water mechanism, the dehydrogenation became barrierless, but required chemisorbed water to act as the hydrogen acceptor. Therefore, the 0.44 eV water chemisorption barrier took the place of the 0.48 eV dehydrogenation barrier. The result is that though the mechanism in the carboxyl pathway has changed, the energetics remains essentially unchanged.

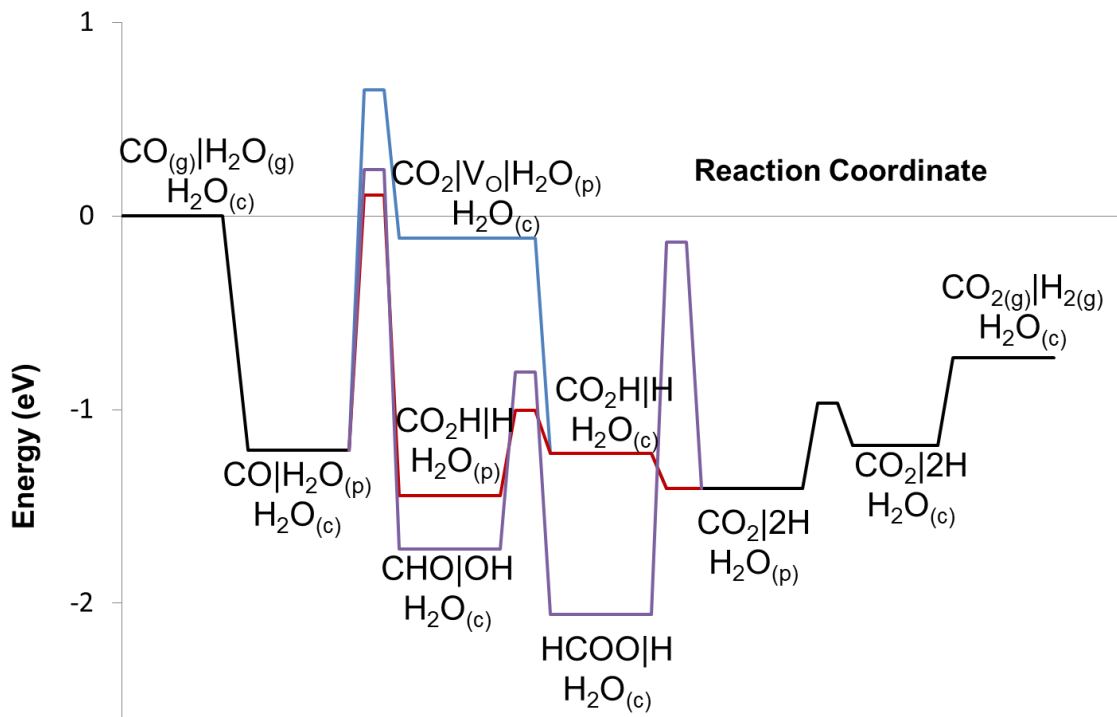


Figure 4.6 Reaction pathways including the effect of cocatalytic water for direct CO oxidation (blue), associative carboxyl (red), and associative formate (purple) pathways. Common steps (CO and H₂O physisorption, water activation to form H₂O(c), and CO₂ and H₂ desorption) are shown in black. All species are surface species at infinite separation except gases as indicated and as follows: H₂O(c) is OH+H coadsorbed on the same slab, HCOO+H are coadsorbed on the same slab, and CHO+OH are coadsorbed on the same slab. 0-6

Cocatalytic water plays a role in two steps of the associative formate pathways.

The greatest impact was in the CO hydrogenation step to form formyl (6) and (6'). The reduction of nearly 3 eV in this barrier meant that the apparent barrier for the highest energy transition state was 0.24 eV above the gas phase energy for the reactants. This makes it compare favorably with the direct CO oxidation mechanism, and comparable to the 0.11 eV barrier for the carboxyl pathway. The formate pathway would be essentially impossible without cocatalytic water, such as for low water coverage, but becomes competitive at high water coverage when adsorbed water may serve as a cocatalyst. Without cocatalytic water, the formate dehydrogenation step was also difficult, with the a transition state energy 0.17 eV above the gas phase energy. In the water assisted

mechanism, this barrier, while still large relative to the adsorbed reactants, was lower in energy than the gaseous reactants.

4.4 Conclusions

Periodic density functional theory calculations were carried out to investigate the mechanism of the water gas shift reaction on the (101) surface of anatase TiO_2 . The interactions between WGS intermediates and the anatase surface revealed the role of electronegativity on the binding modes of cationic and anionic adsorbates and on the reduction of Ti^{4+} centers. Two different structures for adsorbed water were considered: molecularly physisorbed water and dissociatively chemisorbed water. Three possible WGS mechanisms were proposed from these adsorbed structures: direct CO oxidation and associative mechanisms with carboxyl and formate intermediates. The effect of coadsorbed water molecules on the activation energy barriers of elementary steps was explored, where chemisorbed water behaved as a hydrogen acceptor and physisorbed water behaved as a hydrogen donor.

Direct CO oxidation was only possibly via lattice oxygen, where CO_2 formation also created a surface oxygen vacancy. Healing these oxygen vacancies with chemisorbed water was barrierless, while molecular water showed a very high activation energy barrier. Without any hydrogen transfer steps, energetics of the CO oxidation pathway were unaffected by cocatalytic water.

The carboxyl pathway showed the lowest apparent activation energy barrier of all three pathways. The formation of carboxyl came from CO hydroxylation by chemisorbed water and was the most difficult step. Without assistance from water, the subsequent

dehydrogenation of carboxyl was the second largest barrier in this mechanism. When the reaction was cocatalyzed by water, this reaction became barrierless, and instead the activation energy required to activate a second molecule of water replaced the dehydrogenation barrier. This meant that despite minor changes to the mechanism, the energetics of the carboxyl pathway were largely unaffected.

The formate pathway could be ruled out in the unassisted mechanism due to the 4.23 eV barrier to hydrogenate carbon monoxide in the first step. However, when assisted by water acting as a hydrogen donor, the barrier for this reaction dropped to 1.45 eV and the apparent barrier relative to gas phase reactants was only slightly larger than for the carboxyl pathway. The changes in the potential energy surfaces with participation from noninnocent coadsorbed water molecules were sufficient to make the formate pathway feasible on the (101) surface of anatase TiO_2 .

These suggest that the concentration of adsorbed water, which would be expected to vary with water/carbon monoxide ration during WGS, can change the feasible reaction pathways on the TiO_2 surface. The metal-free calculations on anatase have implications for TiO_2 -supported metal WGS catalysts, as the composition and concentrations of reactive species on the metal oxide surface are expected to vary with surface water concentration.

Chapter 5: Density Functional Theory Investigation of the Role of Cocatalytic Water in Methane Steam Reforming over Anatase TiO₂

(101)

5.1 Introduction

Hydrogen gas has potential as a clean-burning energy carrier that produces only water as a byproduct of combustion. Hydrogen fuel, when used in a fuel cell for stationary or transportation power, can provide higher thermodynamic efficiency than conventional internal combustion. However, elemental hydrogen is not found on earth, and must be chemically separated from one of its compounds such as water or methane. Commercially, methane steam reforming (MSR) is used to convert fossil methane to hydrogen gas and carbon monoxide (as syngas) at high temperature, providing over half of global hydrogen production.⁸⁸⁻⁹⁰ The reaction is endergonic and endothermic, requiring high energy input at high temperature.¹⁵⁰⁻¹⁵¹ As a result, the reaction operates with poor atom efficiency as half of the methane must be burned to provide heat for the process,¹⁵² which releases CO₂, a greenhouse gas, into the atmosphere. Together with MSR, the water-gas shift (WGS) reaction takes places, where carbon monoxide reacts with water to form carbon dioxide and hydrogen.



Many transition metal catalysts have been investigated for the methane steam reforming reaction, including Rh, Ru, Ni and Pt. Mechanistic studies on these metals have provided insight into the possible surface reaction pathways and rate limiting steps. Two primary pathways have been proposed for MSR. In the first, methane is fully dehydrogenated all the way to atomic carbon before undergoing any oxidation reactions.

Atomic carbon then oxidizes to carbon monoxide. An alternative mechanism involves oxidation at an earlier stage in the process, followed by subsequent dehydrogenation to a formyl intermediate and on to carbon monoxide. Over Ni catalysts, the rate limiting step was found to be the formyl dehydrogenation,^{151,153} while for Rh the initial methane activation step was found to be rate limiting.^{154,155}

Typically, alumina is used as the support for metal nanoparticles in MSR, but several advantages have been suggested for using TiO₂ as a support instead, including lower coke formation, wider range of feasible steam to carbon ratios, and lower reaction temperature for supported Ni particles.¹⁵⁶⁻¹⁵⁸ The Ni/TiO₂ system has been investigated for reforming of alcohols as well, including methanol,¹⁵⁹ ethanol,¹⁶⁰ and glycerol,¹⁶¹ where the interaction of the metal with the support has been implicated in the determining catalyst stability.

The application of TiO₂ and other semiconductors in methane steam reforming is potentially interesting as a photochemical alternative to the high-temperature thermocatalytic route in current industrial practice. Such a process, if it could lower the high-temperature requirement of MSR, could potentially double the atom efficiency by reducing or eliminating the need for fuel burn for heat generation, reducing carbon dioxide emissions and improving resource sufficiency. The Yoshida group has been investigating supported precious metals such as Pt and Rh on TiO₂,¹⁶² titanates,^{163,164} tantalates,^{165,166} and gallium oxide,¹⁶⁷ for photocatalytic MSR under mild conditions. In the reaction of water and methane over Pt/TiO₂, CO₂ was the primary carbonaceous product, with trace amounts of CO and ethane observed, and strong evidence for the formation of surface formates.

The WGS reaction has also been investigated both experimentally and computationally over supported metal nanoparticles,⁹³⁻¹⁰¹ where reducible metal oxides such as TiO_2 have been implicated in the dissociation of water.¹⁰⁴⁻¹⁰⁶ The structure and behavior of water molecules on TiO_2 surfaces has been probed with density functional theory (DFT) methods to give insight into binding geometries and energies.¹³³⁻¹³⁶ In Chapter 4 we investigated WGS mechanisms on the (101) surface of anatase TiO_2 with density functional theory calculations. We found that under conditions of low water coverage, the associative pathway with carboxyl as the intermediate was favored. At high water coverage, adsorbed water molecules would take a cocatalytic role in hydrogen transfer steps by acting as a hydrogen acceptor or donor, reducing the activation energy barriers of such steps. This meant that the associative formate pathway was competitive with the carboxyl pathway when the cocatalytic role of water was taken into consideration. Formation of OH radicals was predicted to be restricted to photocatalytic reaction conditions due to the large formation energies, consistent with experimental reports.¹⁴⁴⁻¹⁴⁶

In the present work, DFT is applied to the MSR reaction on anatase TiO_2 (101). A series of potential reaction intermediates formed from dehydrogenation, O addition, and OH addition reactions with methane and its derivatives is considered. Using binding energies and structures for these intermediates, potential energy surfaces for multiple reaction pathways are generated. The most energetically unfavorable pathways are excluded from further consideration. The remaining pathways all involve formaldehyde dehydrogenation to formyl as an intermediate, via either methoxyl or methylene intermediates. Activation energy barriers for these remaining pathways are calculated and

compared, including the role of cocatalytic water. Chemisorbed water can assist in dehydrogenation steps by acting as a hydrogen acceptor, lowering the barriers for these steps. These results help interpret the role of TiO_2 and water in methane steam reforming reactions.

5.2 Methods

Periodic DFT calculations were performed using the VASP code^{49,50} within the generalized gradient approximation (GGA-PBE)¹³⁷ using projector-augmented wave (PAW)^{52,53} potentials. Corrections to the on-site Coulomb interactions have been accounted for through the Hubbard term (DFT+U).¹³⁸ Dudarev's approach¹³⁹ was applied to increase the accuracy of the band gap and reaction kinetics with a $U_{\text{eff}} = 4$ for titanium atoms. This U_{eff} was chosen to align both the band gap and lattice parameters with experimental values as well as prevent electron delocalization.¹⁴⁰⁻¹⁴² The single-electron wave functions were expanded using plane waves with an energy cutoff of 400 eV. All oxide slabs were based on the (101) surface of anatase TiO_2 , and modeled by a (2×2) surface unit cell with four atomic layers for a total of 32 Ti atoms and 64 O atoms.

The lattice constants used for anatase TiO_2 were $a = 3.784 \text{ \AA}$ and $c = 9.515 \text{ \AA}$.¹⁴³ A vacuum layer of 24 \AA was used to separate periodic images of the slab in the z direction (normal to the surface), and a dipole correction was applied and the electrostatic potential was adjusted to ensure that interaction between the surface slab and its periodic images was negligible.⁵⁵ The Brillouin zone was sampled using a $(2 \times 2 \times 1)$ Gamma-centered Monkhorst-Pack k-point mesh⁵⁶ following a convergence test for adsorbate binding energies with respect to sampling mesh size. All four layers were allowed to relax in all calculations. Binding energy is calculated as $\text{BE} = E_{\text{ads}} - E_{\text{slab}} - E_{\text{gas}}$, where

E_{ads} , E_{slab} , E_{gas} are the total energies calculated for the slab with the adsorbate, the clean stoichiometric slab, and the adsorbate in the gas phase, respectively. Formation energies were used in analyzing oxygen vacancy formation, defined as $FE = E_{vo-slab} + E_{o-gas} - E_{slab}$, where $E_{vo-slab}$ and E_{o-gas} were the total energies for the oxygen vacancy slab and the oxygen atom in gas phase, respectively. The addition of a single adsorbate molecule to a slab with a (2×2) surface until cell corresponds to $\frac{1}{4}$ ML adsorbate coverage. The nudged elastic band (NEB) method⁵⁷ was used to find transition states and calculate activation energy barriers.

5.3 Results and Discussion

5.3.1 Model TiO₂ Surfaces

In anatase, the (101) facet has the lowest surface energy, with the lowest extent of coordinative unsaturation. In the surface layer, one Ti-O bond is cleaved per two surface titanium atoms yielding 0.10 bonds cleaved per Å². The model surface used in this study consists of a (2×2) surface unit cell of anatase (101). A total of eight Ti-O bonds are cleaved in the surface layer, leaving four atoms each of under-coordinated Ti and O atoms. The remaining surface Ti atoms (four) and O atoms (eight) are coordinatively saturated, with the same valency as in the bulk. The unit cell is the same as shown in Figure 4.1.

The reducibility of surface titanium atoms is well-described in this model. Hydrogen atoms prefer to bind atop the coordinatively unsaturated oxygen atoms, and become protons by charge transfer to geminal titanium atoms, effectively capturing the nominal reduction from Ti⁴⁺ to Ti³⁺.^{Error! Bookmark not defined.} Other adsorbates less electronegative than a Ti⁴⁺ center were found to behave similarly, and could be viewed as

cations with a reduced titanium center, including formyl (CHO), hydroxymethylidyne (COH), and carboxyl (CO₂H). By contrast, adsorbates more electronegative than Ti⁴⁺ would not oxidize upon adsorption, and when placed on the (101) surface alone formed high energy radical states. These adsorbates could be stabilized by coadsorbing H atoms in the same calculation slab. The significant stabilization in this binding arrangement can be interpreted by viewing the adsorbate and the hydrogen atom as an anion/cation pair, with H oxidized to a proton, and electron transfer to reduce the electronegative adsorbate to a cation. Hydroxyl (OH) and formate (HCOO) were found to take very high energy states when adsorbed alone, but were greatly stabilized as anions when coadsorbed with protons.

The binding interactions of water molecules with TiO₂ surfaces are of particular importance in the investigation of catalytic mechanisms involving water as a reactant and as a promoter or cocatalyst.^{105,106,133-136,144-146} Water may bind to the (101) surface of anatase molecularly as a physisorbed species or dissociatively as a chemisorbed species. The calculated structures are shown in Figure 5.1. In physisorbed water (H₂O_(p)), water binds atop the undercoordinated Ti atom, such that the oxygen atom occupies roughly the position of the Ti-O bond cleaved to form the (101) surface with a binding energy of -0.87 eV relative to a free water molecule. Chemisorbed water (H₂O_(c)) consists of hydroxyl groups formed from the heterolytic cleavage of a water O-H bond, resulting in an OH⁻ anion bound to the Ti atop site, and a proton bound to the undercoordinated bridging O atom, with a binding energy of -0.65 eV relative to a free water molecule. This means that the calculated energy to dissociate water was 0.22 eV, and the barrier for

water dissociation on the surface considered here was calculated to be 0.44 eV, consistent with reports that water dissociation is an activated process on anatase (101) .^{133-135, 144}

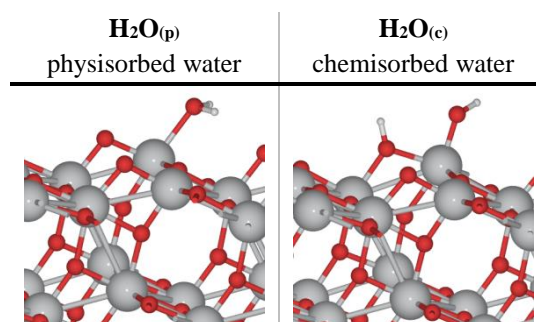
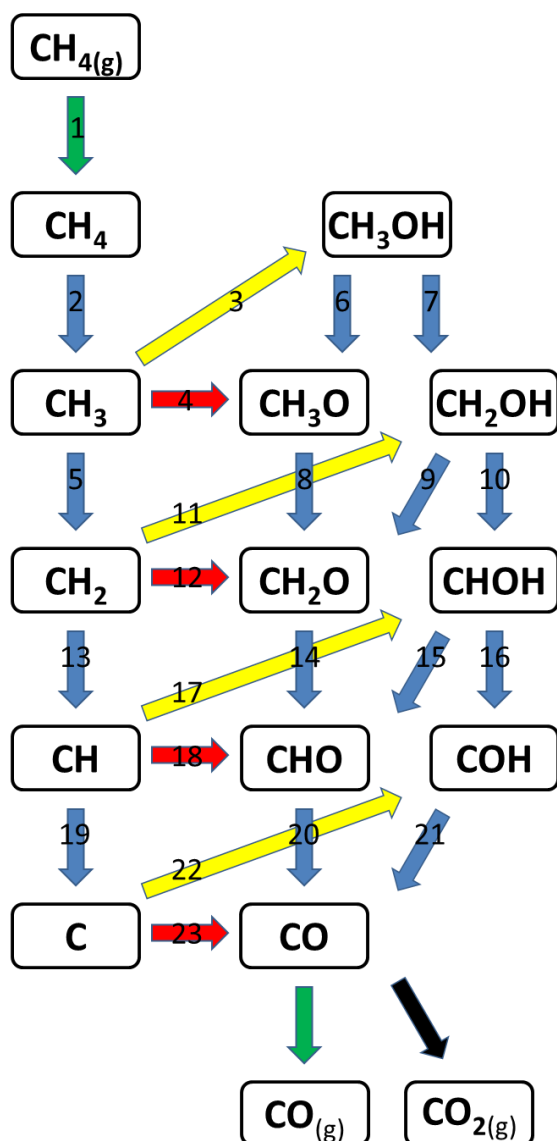


Figure 5.1 Side view of the best binding orientations of water on anatase (101) in its physisorbed and chemisorbed states. Chemisorbed water is bound as an OH^-/H^+ anion/cation pair from the heterolytic cleavage of the O-H bond in physisorbed water. 0-1

5.3.2 MSR Reaction Pathways and Intermediates

The elementary reactions of surface intermediates involved in conversion of methane into CO or CO_2 can be classified into three main types: cleavage of a C-H bond in a dehydrogenation step; direct oxidation by O to form a C-O bond; and addition of an OH group. Starting from methane, these successive steps are shown in Scheme 5.1. Following weak adsorption, the first step in the reaction is the initial and difficult C-H activation step. This is the only CH_x species that may not undergo direct oxidation or OH addition, which would violate the preferred sp^3 hybridization of carbon. After this initial C-H bond cleavage, the subsequent CH_x species methyl (CH_3), methylene (CH_2), methylidyne (CH), and carbon may all undergo dehydrogenation (except carbon), direct oxidation, or OH addition, leading to a number of oxygenated intermediates, CH_xO . Subsequent dehydrogenation of these species leads to additional reaction pathways without increasing the number of species under consideration, so thirteen total adsorbates need to be considered.

Ultimately, the pathways in Scheme 5.1 converge at adsorbed CO, which may desorb or itself react further in the water-gas shift reaction. The reactivity of CO towards water-gas shift, including the surface intermediates involved in the reaction are treated in detail in Chapter 4. These reactions are summarized in a single arrow in Scheme 5.1, but comprise of three possible mechanisms, direct CO oxidation and associative pathways with carboxyl and formate (HCOO) intermediates. Two of these mechanisms are directly comparable to the elementary O and OH addition steps considered in Scheme 5.1. The direct oxidation of CO was found to be kinetically unfavorable compared to the carboxyl mechanism, which begins with OH addition. The formate pathway begins with a hydrogenation step (as compared to dehydrogenation steps in Scheme 5.1) leading to CHO or COH. The reverse of both of these steps are also shown in Scheme 5.1. Unassisted, the formate pathway was found to be kinetically unfavorable on anatase (101) due to a very large 4.23 eV barrier for CO hydrogenation. However, adsorbed water functioned effectively as a hydrogen transfer agent, reducing the barrier of the reaction to 1.45 eV without being consumed in the reaction. Adsorbed water therefore played a cocatalytic role in assisting hydrogen transfer steps on the anatase (101) surface, and made the formate and carboxyl pathways competitive.



Scheme 5.1 Elementary dehydrogenation (blue arrows), direct oxidation (red), and OH addition (yellow) steps implicated in methane steam reforming to CO. Adsorption/desorption steps shown in green. Conversion of CO to CO₂ in the water-gas shift reaction is summarized by the black arrow, and discussed in chapter 4. All species adsorbed on TiO₂ surface except for gaseous species as indicated.

5.3.2.1 Binding of CH_x Species

When placed near the TiO₂ surface, methane showed little affinity for the surface (-0.01 eV binding energy) with no site preference. The binding geometry was essentially

that of a gaseous molecule far from the surface. The binding geometries and binding energies of dehydrogenated CH_x species are given in Figure 5.2 and Table 5.1 respectively.

Removing a hydrogen atom from methane to form methyl created a cationic adsorbate binding to the undercoordinated oxygen atom with a binding energy of -1.38 eV. Both the binding site and geometry were the same for CH_3^+ as for a proton, including the reduction of the geminal undercoordinated Ti atom to Ti^{3+} . The next best binding site on a coordinatively saturated oxygen atom was 0.93 eV higher in energy, indicating a very strong site preference for the undercoordinated sites.

Methylene bonded to a Ti-O bridge site at the undercoordinated titanium and oxygen atoms. In analogy to CH_3 , CH_2 may have been expected to bind to the undercoordinated surface oxygen atom and reduce the nearby titanium center. As the CH_2 radical has two unpaired electrons, this would have been expected to lead to doubly reduced Ti^{2+} or two Ti^{3+} centers. Instead, no reduction in the oxidation state of titanium was observed. Instead, CH_2 formed an additional Ti-C bond with the undercoordinated Ti atom, leading to the bridging geometry in Figure 5.2.

Two binding modes for methyldiyne were found. The first was similar to CH_2 and bound to the bridging Ti-O site consisting of the undercoordinated atoms with a binding energy of -3.87 eV. The alternative binding mode, shown in Figure 3, was 0.18 eV more stable, with a binding energy of -4.05 eV. The CH group inserted into a Ti-O bond between a coordinatively saturated titanium atom and the unsaturated O atom. The resulting structure is equivalent to a formyl group (CHO) binding to an oxygen vacancy

formed by transferring the lattice oxygen to the adsorbate. This result is an unusual planar geometry around carbon. In either structure, a single Ti atom is reduced to Ti^{3+} while the remaining electrons from the CH group constitute the new Ti-C bond.

Atomic carbon showed a similar effect to CH in that the preferred binding mode inserted into the lattice Ti-O bond, forming a CO molecule adsorbed to the oxygen vacancy by transferring the O atom to the carbon. The result was binding energy of -4.84 eV.

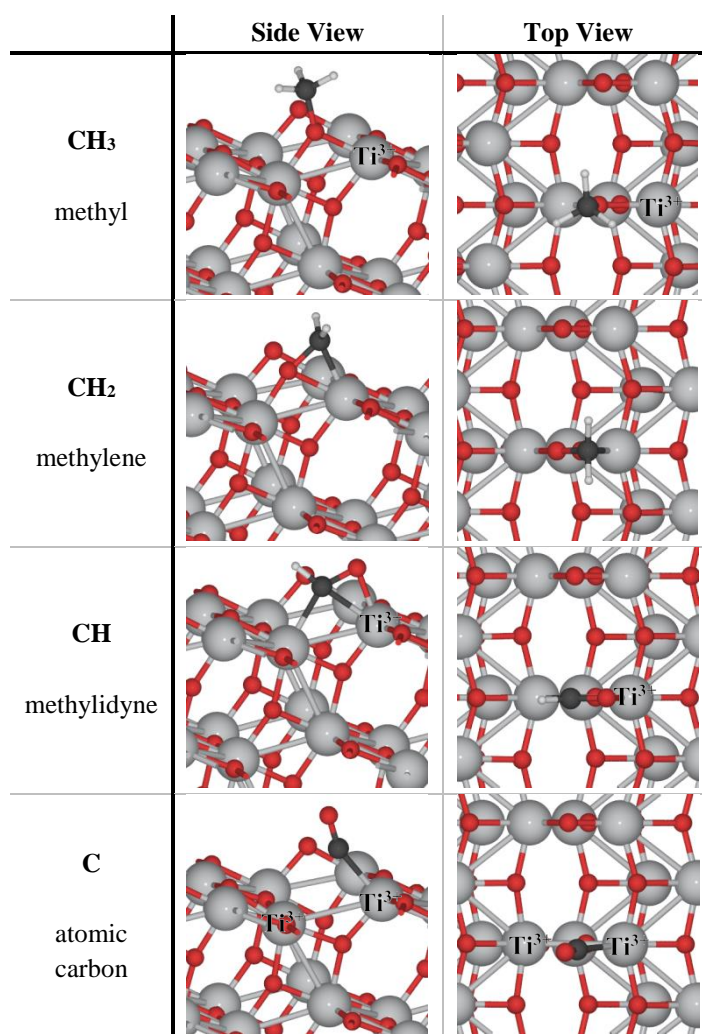


Figure 5.2 Best binding orientations of CH_x species on anatase (101). Reduced Ti³⁺ centers are labelled where present. CH₃, CH, and C adsorb as cations, and CH₂ adsorbs as a neutral species. 0-2

On the (101) facet of anatase, the undercoordinated oxygen atoms are 3.8 Å apart. This large spatial distance means that small CH_x species may only bind to a single binding site, meaning that methylidyne and atomic carbon will not be tetravalent around the carbon center. The binding modes of these adsorbates in Figure 5.2 circumvent this problem by insertion into the Ti-O bond, creating additional binding interactions at the oxygen vacancy that forms. Despite this stabilization, these species are still significantly uphill in energy relative to gaseous methane and clean TiO₂ surfaces, as discussed below.

5.3.2.2 Binding of CH_xO Species

The addition of O or OH to the four CH_x species in Figure 5.2 leads to the formation of the eight adsorbed CH_xO species shown in Scheme 5.1. The structures of these species bound to the (101) surface of anatase are shown in Figure 5.3, and the binding energies are given in Table 5.1. The general trends in binding preferences followed those observed for CH_x species and for water, and analogies can be drawn between them.

The interaction of methanol with the anatase surface most closely resembled that of physisorbed water. The O atom of methanol interacted with the undercoordinated Ti atom in a geometry not unlike the lattice position of the “missing” oxygen from the cleavage of the surface plane. The O-H bond was oriented parallel to the surface, as in water, but the methyl group pointed away from the surface, such that the plane of the molecule was orthogonal to the surface. The entirety of the water molecule was oriented parallel to the surface, probably due to its smaller size. As the methanol molecule is intact

in this binding structure, this can be thought of as physisorbed methanol, with a binding energy of -0.80 eV.

The methoxyl group, CH_3O , was the only adsorbate more electronegative than Ti^{4+} , and attempts to place it on a clean surface led to very high energy radical states. Similar phenomena were found with adsorption of hydroxyl and formate species and given that hydroxyl and methoxyl are isoelectronic adsorbates, the similar binding modes are sensible. Instead, the methoxyl species was added to a calculation slab already containing a hydrogen atom, similar to hydroxyl and formate cases, the resultant stabilization of the methoxyl can be described as an anionic CH_3O^- group coadsorbed with a proton. The binding energy was -2.84 eV. In this structure, the methoxyl oxygen was in a similar position as in physisorbed methanol, atop the undercoordinated Ti atom. The proton was situated on an undercoordinated oxygen atom that did not share a bond with the binding site for the methoxyl group. In all discussion that follows, CH_3O was coadsorbed with H in order to obtain the stabilized anionic structure rather than the high energy radical. During MSR reaction conditions, water activation would lead to the formation of adsorbed hydrogen atoms (as protons) and so this coadsorption model is reasonable.

Hydroxymethyl (CH_2OH) took a binding geometry similar to that of methyl. In both adsorbates, a CH_2 group sat atop the undercoordinated bridging surface oxygen and transferred charge to the geminal undercoordinated Ti atom, described as a Ti^{3+} center. In addition the OH group in hydroxymethyl pointed towards a different undercoordinated Ti atom not bonded to the bridging oxygen, forming a 2.55 Å O-Ti dative bond. This highly elongated bond is in contrast to 1.9-2.0 Å for lattice Ti-O bonds in the surface layer, and

the two Ti-O bonds of the bridging oxygen involved in bonding at 2.05 Å and 2.12 Å. This weak interaction did not stabilize the hydroxymethyl group by much (binding energy = -1.83 eV), and compared to CH₃O, its isomer, hydroxymethyl was 0.62 eV unfavorable.

Formaldehyde is a molecular species with a double bond that is able to form an η^2 interaction with the two adjacent undercoordinated sites. The CH₂ group bonded to an oxygen atom and the O atom bonded to a titanium atom. The π electrons of formaldehyde are implicated in the bonding interaction, as evidenced by the elongation of the C-O double bond. In calculations of free formaldehyde, the double bond was 1.21 Å, but in the adsorbed molecule, the bond had stretched to 1.40 Å, nearly as long as the single bond in free methanol (1.43 Å).

Hydroxymethylene (CHOH) is an isomer of formaldehyde and took a binding orientation nearly identical to that of methylene. The OH group of CHOH was positioned in the same orientation as one of the CH groups in CH₂. By also taking a bridging binding site between the undercoordinated titanium and oxygen atoms, the CHOH group was also able to bind without transferring charge to the support, and no reduction of titanium was observed. Although the binding energy of CHOH (-1.92 eV) appears to be stronger than that of formaldehyde, the proper comparison is between the total energy of both isomers in their best binding orientations. This difference reveals that CHOH was 1.22 eV less favorable than formaldehyde.

Unlike formaldehyde, the C-O group in formyl retained its carbonyl character upon binding to the undercoordinated oxygen atom. The carbonyl oxygen formed a dative bond (2.25 Å) with a nearby Ti atom, but the C-O bond length was still only 1.25

Å, much more similar to the double bond in formaldehyde than the single bond in methanol. The isomer of formyl, hydroxymethylidyne, showed a stronger binding energy, but comparing the relative energies for the two isomers, formyl was more favorable by 1.58 eV. Both isomers formed a reduced titanium center at the geminal Ti atom.

Table 5.1 Binding energies of MSR intermediates species on anatase (101) in eV. 0-1

Species	BE
CH₄	-0.01
CH₃	-1.38
CH₂	-3.02
CH	-4.05
C	-4.84
CH₃OH	-0.80
CH₃O + H^a	-2.84
CH₂OH	-1.83
CH₂O	-0.84
CHOH	-1.92
CHO	-2.29
COH	-2.57
CO	-0.34
CO₂	-0.20

^a Coadsorbed as anion and a proton.

Between all isomer pairs in Scheme 5.1, the isomers with OH groups formed from cleavage of a C-H group in CH_{x-1}OH species, or OH addition to CH_x species, were always less stable than the isomers without OH groups. These more stable isomers were formed from O-H cleavage or from O atom addition to CH_x species. The preference between isomers became larger as the adsorbates underwent successive hydrogenation, with a modest difference of 0.62 eV between methoxyl and hydroxymethyl, up to a significant difference of 1.58 eV between formyl and hydroxymethylidyne.

	Side View	Top View
CH_3OH methanol		
CH_3O methoxyl		
CH_2OH hydroxymethyl		
CH_2O formaldehyde		
CHOH hydroxymethylene		
CHO formyl		

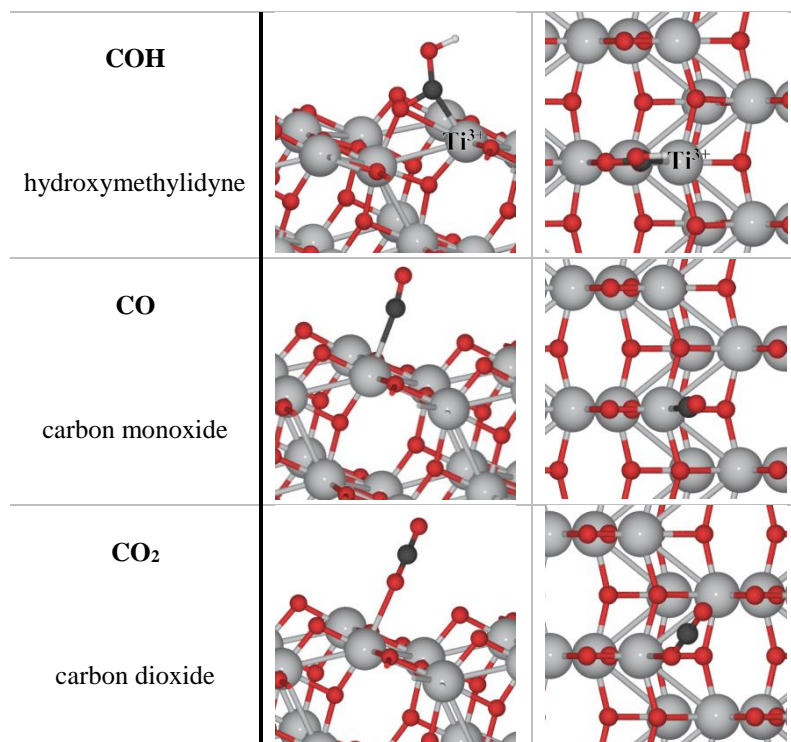


Figure 5.3 Best binding orientations of CH_xO species on anatase (101). Reduced Ti³⁺ centers are labelled where present. CH₂OH, CHOH, CHO and COH adsorb as cations, CH₃O adsorbs as an anion and is coadsorbed with a proton, and CH₃OH, CH₂O, CO and CO₂ adsorb molecularly.⁰⁻³

5.3.2.3 Binding of CO_x Species

CO and CO₂ interacted only weakly with the anatase (101) surface. Both molecules physisorbed to a top site over titanium in their preferred binding geometries, via carbon in CO and via oxygen in CO₂ (Figure 5.3). With low binding energies of -0.34 eV and -0.20 eV respectively, CO and CO₂ must compete for these binding sites with many species, including molecularly adsorbed water, which binds to the Ti top site more strongly.

5.3.3 Methane Steam Reforming Pathways

Constructing reaction pathways consisting of elementary steps from methane to CO (or CO₂) connecting all the intermediates in Table 5.1 using the three reaction classes identified in Section 5.3.2 (dehydrogenation, O addition, OH addition) requires

reconsideration once the very high energy of OH and O radicals is considered. Instead, alternate mechanisms involving water were considered. For OH addition steps, (steps 3, 11, 17, 22 in Scheme 5.1), chemisorbed water is substituted in the reaction, such that the reaction occurs with the anionic hydroxyl and the proton is generated as a byproduct. In the absence of atomic oxygen, the direct oxidation by O (steps 4, 12, 18, 23 in Scheme 5.1) may proceed either by pulling oxygen from the TiO₂ lattice, generating an oxygen vacancy (V_O), or by pulling oxygen directly from chemisorbed water.



The energetic penalty for forming oxygen vacancies is significant, and the difference between these two mechanisms comprises the energy required to heal a vacancy with chemisorbed water, $\text{V}_\text{O} + \text{H}_2\text{O}_{(\text{c})} \rightarrow 2\text{H}$, with calculated reaction energy of -1.29 eV. Due to this large difference in reaction energies, only the reactions with chemisorbed water were considered, and formation of lattice oxygen vacancies was not considered further.

The reaction energies for all steps in the MSR reaction are given in Table 5.2. Using these reaction energies, the potential energy surfaces in Figure 5.4 were constructed. Nearly all dehydrogenation steps were endothermic, except for the dehydrogenation of high energy CHOH and COH species. OH addition was always exothermic, but O addition could be exothermic or endothermic depending on the reactant – CH₃ oxidation by water was slightly uphill while all others were downhill. The pathways leading to adsorbed CHO or CO involved adsorption and activation of one molecule of water, which was consumed in either OH or O addition steps. From either CHO or CO to CO_(g) required no additional water. The water-gas shift steps, starting from either CO or CHO, require adsorption and consumption of one additional water molecule.

The details of the water-gas shift reaction are discussed in Chapter 4 and are omitted from Figure 5.4 except for steps derived from CHO. The pathway from CHO to CO₂ appears to be more favorable than any pathway leading to CO_(g). Experimental investigation of MSR on metal-free anatase TiO₂ confirm that CO₂ is the preferred CO_x product.¹⁶⁸

Table 5.2 Reaction energies for elementary steps in MSR mechanism.^{a 0-2}

	Reaction	ΔE
(1)	$\text{CH}_{4(g)} \rightarrow \text{CH}_4$	-0.01
(2)	$\text{CH}_4 \rightarrow \text{CH}_3 + \text{H}$	+0.97
(3) ^b	$\text{CH}_3 + \text{H}_2\text{O}_{(c)} \rightarrow \text{CH}_3\text{OH} + \text{H}$	-0.10
(4) ^c	$\text{CH}_3 + \text{H}_2\text{O}_{(c)} \rightarrow \text{CH}_3\text{O} + 2\text{H}$	+0.11
(5)	$\text{CH}_3 \rightarrow \text{CH}_2 + \text{H}$	+0.94
(6)	$\text{CH}_3\text{OH} \rightarrow \text{CH}_3\text{O} + \text{H}$	+0.20
(7)	$\text{CH}_3\text{OH} \rightarrow \text{CH}_2\text{OH} + \text{H}$	+0.82
(8) ^d	$\text{CH}_3\text{O} + \text{H} \rightarrow \text{CH}_2\text{O} + 2\text{H}$	+0.81
(9)	$\text{CH}_2\text{OH} \rightarrow \text{CH}_2\text{O} + \text{H}$	+0.19
(10)	$\text{CH}_2\text{OH} \rightarrow \text{CHOH} + \text{H}$	+1.42
(11) ^b	$\text{CH}_2 + \text{H}_2\text{O}_{(c)} \rightarrow \text{CH}_2\text{OH} + \text{H}$	-0.21
(12) ^c	$\text{CH}_2 + \text{H}_2\text{O}_{(c)} \rightarrow \text{CH}_2\text{O} + 2\text{H}$	-0.02
(13)	$\text{CH}_2 \rightarrow \text{CH} + \text{H}$	+1.38
(14)	$\text{CH}_2\text{O} \rightarrow \text{CHO} + \text{H}$	+0.10
(15)	$\text{CHOH} \rightarrow \text{CHO} + \text{H}$	-1.13
(16)	$\text{CHOH} \rightarrow \text{COH} + \text{H}$	+0.45
(17) ^b	$\text{CH} + \text{H}_2\text{O}_{(c)} \rightarrow \text{CHOH} + \text{H}$	-0.18
(18) ^c	$\text{CH} + \text{H}_2\text{O}_{(c)} \rightarrow \text{CHO} + 2\text{H}$	-1.30
(19)	$\text{CH} \rightarrow \text{C} + \text{H}$	+0.51
(20)	$\text{CHO} \rightarrow \text{CO} + \text{H}$	+0.73
(21)	$\text{COH} \rightarrow \text{CO} + \text{H}$	-0.85
(22) ^b	$\text{C} + \text{H}_2\text{O}_{(c)} \rightarrow \text{COH} + \text{H}$	-0.23
(23) ^c	$\text{C} + \text{H}_2\text{O}_{(c)} \rightarrow \text{CO} + 2\text{H}$	-1.08

ΔE is the energy of reaction in eV. All species are surface species at infinite separation except for gaseous species and coadsorbed species as follows: H₂O_(c) or OH+H, and CH₃O+H which are coadsorbed as anions and protons on the same slab. ^a All steps in this table neglect cocatalytic water. ^b Modified from Scheme 1 to use anionic OH⁻ from chemisorbed water. ^c Modified from Scheme 1 to use water as oxidant. ^d A spectator hydrogen atom is included in the reaction as methoxyl must be coadsorbed with a proton for charge balance.

Comparing the pathways in Figure 5.4, there are some reactions that are unlikely to occur based on energetics alone. Considering the reactions from CH₂, the

dehydrogenation reaction is +1.38 eV uphill compared to water chemisorption at +0.22 eV followed by O or OH addition which are both downhill. Similarly CH₂OH can undergo C-H scission at +1.42 eV or O-H scission at +0.19 eV. Adding the activation energy barriers over these large endothermic reaction energies would make these reactions even less favorable. Given the large discrepancy in reaction energies at these forks, these higher-energy pathways were excluded from further consideration. Eliminating CH formation from CH₂ (step 13 from Scheme 5.1) and CHOH formation from CH₂OH (step 10) means that steps forming atomic carbon and COH would also be excluded, as well as any further elementary reactions of these species. The four eliminated intermediates, CH, C, CHOH, and COH were the only adsorbed states on the potential energy surface higher in energy than adsorbed CO. Altogether, steps 10, 13, 15-19 and 21-23 from Scheme 5.1 could be eliminated.

The potential energy surface in Figure 5.4 also makes methanol synthesis from methane look quite feasible. This is a surprising result, as direct synthesis of methanol from methane has received significant research attention.¹⁶⁹ Surely if methanol formation were possible, its desorption energy of only 0.80 eV would mean that it would be favored as a product over subsequent surface reactions to CO and CO₂. Desorption of methanol would be roughly equivalent in energy to the bound CH₂OH state in Figure 5.4. However, this reaction has not been reported experimentally, and experiments on metal-free anatase do not detect methanol as a product.¹⁶⁸ By contrast, formaldehyde is observed as a gas-phase product in these reactions at low yield, and so pathways involving formaldehyde as an intermediate can still be considered as relevant. The desorption energy of formaldehyde of 0.84 eV makes it comparable in energy to the

adsorbed CO state in Figure 5.4. That formaldehyde is seen, but not as a major product experimentally suggests that pathways leading from adsorbed formaldehyde to other products are kinetically and thermodynamically more favorable than formaldehyde desorption or conversion of formaldehyde to CO via CHO. This again points to the pathway from CHO to $\text{CO}_{2(g)}$ as appearing to be more energetically favorable than any pathway to $\text{CO}_{(g)}$.

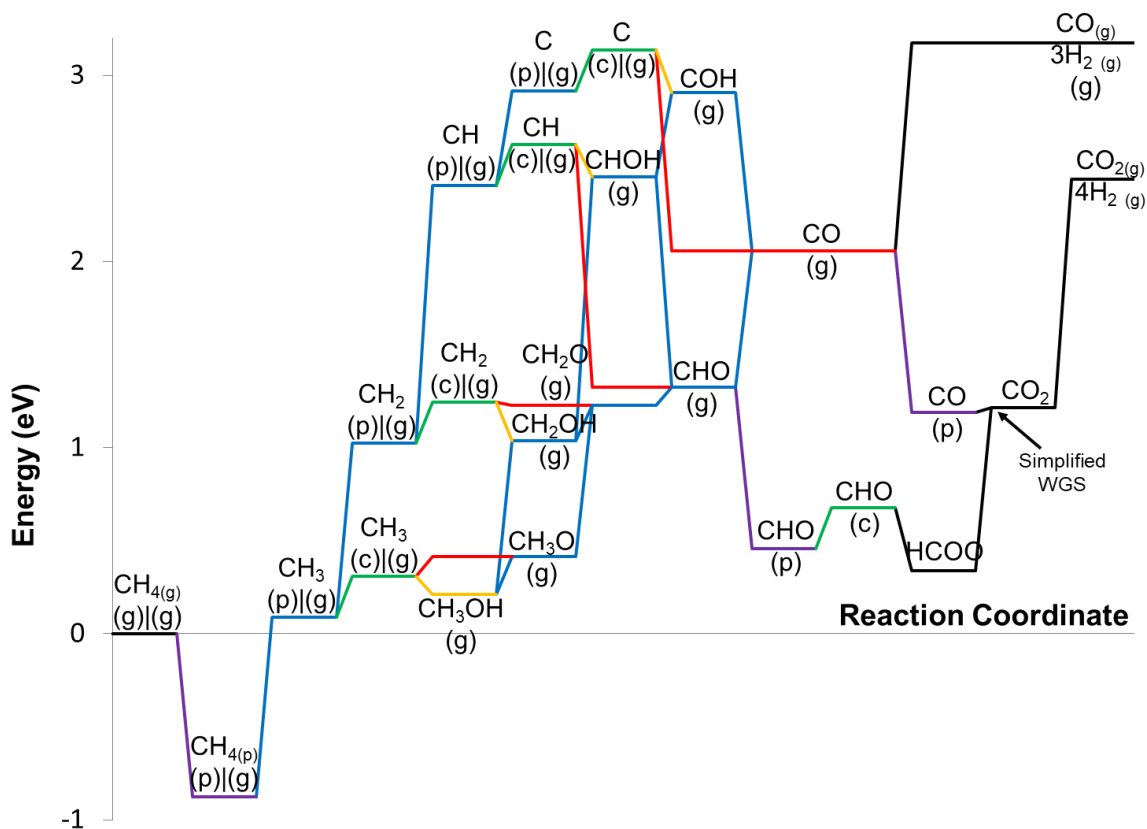


Figure 5.4 Potential energy surfaces for methane steam reforming mechanisms on anatase TiO_2 (101). Elementary steps include dehydrogenation (blue), oxidation by O (red), and OH addition (yellow). Additional steps include water physisorption (purple), chemisorption (green), and water-gas shift reaction (black). WGS mechanism not shown in detail except for CHO/HCOO pathway. State of any water molecules present indicated by (g) gaseous, (p) physisorbed, (c) chemisorbed. Surface hydrogen atoms as products omitted for clarity, and associative desorption as H_2 included with final CO and CO_2 desorption steps. All species are surface species at infinite separation except for gaseous species and coadsorbed species as follows: $\text{H}_2\text{O}_{(c)}$ or $\text{OH}+\text{H}$, and $\text{CH}_3\text{O}+\text{H}$ which are coadsorbed as anions and protons on the same slab. 0-4

After eliminating several pathways from methane to CO_x based on the above discussion, the pathways that remain all begin with methane dehydrogenation to methyl,

Step 2 in Scheme 5.1, and involve formaldehyde and CHO as intermediates. From methyl to formaldehyde there are three possible pathways. The methoxyl pathway involves oxidation of methyl by water to form methoxyl, Step 4, followed by methoxyl dehydrogenation, Step 8. Two other pathways begin with methyl dehydrogenation to methylene, Step 5. The direct methylene pathway is defined by the oxidation of methylene to formaldehyde by water, Step 12, while the indirect methylene pathway involves OH addition to methylene to form CH_2OH , Step 11, followed by dehydrogenation to formaldehyde, Step 9. From formaldehyde, Step 14 is the dehydrogenation reaction to formyl. Formyl may take two pathways, the dehydrogenation pathway to CO, Step 20, or the WGS pathway to CO_2 via formate. Adsorbed CO itself can desorb or undergo WGS via the carboxyl pathway to CO_2 . Activation energy barriers for these remaining steps are discussed in the following sections.

5.3.4 Elementary Reactions without Assistance from Cocatalytic Water

Methane activation is a challenging reaction for any catalyst surface due to the symmetry of the molecule and its four strong C-H bonds. Coupled with its weak interaction with the TiO_2 surface, the dehydrogenation of methane to methyl is expected to be a challenging reaction. In the transition state structure (Figure 5.5), the carbon atom interacts with the undercoordinated surface bridging atom while one C-H bond stretches towards the undercoordinated Ti atom. This transition state resembles pentavalent carbon, and the product state for this mechanism places the hydrogen atom at an unfavorable position atop a Ti atom. Together, these factors contribute to a very large activation energy barrier of 4.96 eV when the reaction is unassisted and takes place on the clean anatase (101) surface. This barrier is likely prohibitive even at high temperatures, and

further reaction is unlikely if the initial barrier is unsurmountable. For this reason, the cocatalytic effect of water, which lowers activation energy barriers in WGS mechanism hydrogen transfer steps on anatase (101), was investigated for the MSR reaction pathways. Following the results for WGS, it is expected that water will greatly reduce some of the dehydrogenation barriers in the MSR pathway as well. The effect of cocatalytic water on this and all dehydrogenation steps is discussed in Section 5.3.5.

The barriers for the remaining MSR reaction steps following methane dehydrogenation are reported in Table 5.3, and the reaction pathways are summarized in Figure 5.6. While the initial methane dehydrogenation barrier was large, similarly large barriers were found for other elementary dehydrogenation steps when unassisted by cocatalytic water. The dehydrogenation reaction of methyl to methylene, methoxyl to formaldehyde, and formyl to carbon monoxide all possessed barriers larger than 4 eV. As with methane, these reactions also had large endothermic reaction energies of >0.7 eV. Each of these reactions' transition states were high in energy due in part to the large distance between active sites on the anatase (101) surface. Undercoordinated oxygen atoms, which were the preferred binding sites for many adsorbates including hydrogen atoms, are 3.8 Å apart. Any adsorbates that bind to these sites through the carbon atom must place carbon and hydrogen on these two distant sites in the final state, or else place the hydrogen in an energetically unfavorable binding site as in Figure 6. The transition state must therefore span a large physical distance without any stabilization from nearby surface atoms. In the case of hydrogen transfer between formyl and carbon monoxide, the hydrogen atom in this transition state was found to have a gas-like character, with no interaction with the surface. Another way to describe this effect is that when both

products from the C-H bond scission prefer the same site and site density is low, the competition for binding sites leads to long migration distances for the smaller daughter fragment – the H atom – and consequently large barriers.

Not all dehydrogenation reactions were equally difficult. C-H bond scission in formaldehyde was only 1.62 eV. The reaction energy of only 0.10 eV was also significantly less than with the previous four examples. This was because CH₂O and CHO are the only adsorbates where both the reactant and the product interact with the surface via C and O atoms, and as such the transition state is somewhat stabilized relative to other C-H bond scission reactions. The O-H bond cleavage barrier in CH₂OH was facile in contrast to all C-H cleavage reactions, with a barrier of only 0.48 eV. This is readily explained by the preferred binding structure of hydroxymethyl in Figure 5.3. The oxygen atom is trivalent in this structure, with the dissociating hydrogen atom dissociate pointing towards the hydrogen acceptor site, and an undercoordinated surface oxygen atom only 1.82 Å away.

Unlike hydrogen atom transfer reactions including all the dehydrogenation reactions above, O and OH addition reactions are not expected to benefit from cocatalytic water, and use water as a reactant instead. This means that the barriers for methyl oxidation to methoxyl, methylene oxidation to formaldehyde, and methyl hydroxylation to hydroxymethyl are unchanged in pathways where cocatalytic water is considered. All three of these reactions had small reaction energies of +0.11 eV, -0.02 eV, and -0.21 eV respectively, and used chemisorbed water as a reactant.

In methyl and methylene oxidation reactions, the OH group in chemisorbed water acts as the oxidant, transferring an O atom to the CH_x species and transferring H to a

nearby lattice oxygen atom. The barriers for these reactions were similar, 2.06 eV and 2.00 eV respectively. These large barriers arise due to the concerted cleavage of the O-H bond while forming the C-O bond and a new O-H bond in the transition states. Attempts to find step-wise mechanisms were unsuccessful. Taking methylene oxidation as an example, the hydrogen atom from chemisorbed water transferred to the surface oxygen atom already bonded to one H atom. The product of this elementary step is formaldehyde and a water molecule formed from a lattice oxygen atom, leaving an oxygen vacancy. This reaction therefore pays the same >1 eV energy penalty for forming the vacancy by placing two H atoms on the same oxygen atom. This energy is then recovered as the two hydrogen atoms diffuse away from each other on the surface, restoring the oxygen atom to its lattice position. Therefore, the overall 2.00 eV barrier for this step includes +1.18 eV to form the formaldehyde/water/ V_O state and the overall reaction energy of -0.02 eV includes the -1.20 eV recovered by healing the vacancy. The reaction of water with oxygen vacancies is discussed in more detail in Chapter 4.

Table 5.3 Reaction energies and activation energy barriers in eV for elementary steps in MSR. 0-3

	Reaction	ΔE	E_a
(2)	$\text{CH}_4 \rightarrow \text{CH}_3 + \text{H}$	+0.97	4.96
(2') ^a	$\text{CH}_4 + \text{H}_2\text{O}_{(\text{c})} \rightarrow \text{CH}_3 + \text{H} + \text{H}_2\text{O}_{(\text{p})}$	+0.75	2.95
(4) ^c	$\text{CH}_3 + \text{H}_2\text{O}_{(\text{c})} \rightarrow \text{CH}_3\text{O} + 2\text{H}$	+0.11	2.06
(5)	$\text{CH}_3 \rightarrow \text{CH}_2 + \text{H}$	+0.94	4.55
(5') ^a	$\text{CH}_3 + \text{H}_2\text{O}_{(\text{c})} \rightarrow \text{CH}_2 + \text{H} + \text{H}_2\text{O}_{(\text{p})}$	+0.72	1.68
(8) ^d	$\text{CH}_3\text{O} + \text{H} \rightarrow \text{CH}_2\text{O} + 2\text{H}$	+0.81	4.33
(8') ^{a,d}	$\text{CH}_3\text{O} + \text{H} + \text{H}_2\text{O}_{(\text{c})} \rightarrow \text{CH}_2\text{O} + 2\text{H} + \text{H}_2\text{O}_{(\text{p})}$	+0.60	1.69
(9)	$\text{CH}_2\text{OH} \rightarrow \text{CH}_2\text{O} + \text{H}$	+0.19	0.48
(9') ^a	$\text{CH}_2\text{OH} + \text{H}_2\text{O}_{(\text{c})} \rightarrow \text{CH}_2\text{O} + \text{H} + \text{H}_2\text{O}_{(\text{p})}$	-0.03	<0.44 ^e
(11) ^b	$\text{CH}_2 + \text{H}_2\text{O}_{(\text{c})} \rightarrow \text{CH}_2\text{OH} + \text{H}$	-0.21	1.33
(12) ^c	$\text{CH}_2 + \text{H}_2\text{O}_{(\text{c})} \rightarrow \text{CH}_2\text{O} + 2\text{H}$	-0.02	2.00
(14)	$\text{CH}_2\text{O} \rightarrow \text{CHO} + \text{H}$	+0.10	1.62
(14') ^a	$\text{CH}_2\text{O} + \text{H}_2\text{O}_{(\text{c})} \rightarrow \text{CHO} + \text{H} + \text{H}_2\text{O}_{(\text{p})}$	-0.12	<0.44 ^e
(20)	$\text{CHO} \rightarrow \text{CO} + \text{H}$	+0.73	4.97
(20') ^a	$\text{CHO} + \text{H}_2\text{O}_{(\text{c})} \rightarrow \text{CO} + \text{H} + \text{H}_2\text{O}_{(\text{p})}$	+0.51	1.96

ΔE is the energy of reaction. E_a is the activation energy barrier. All species are surface species at infinite separation except for gaseous species and as follows: $\text{H}_2\text{O}_{(\text{c})}$ or $\text{OH}+\text{H}$, and $\text{CH}_3\text{O}+\text{H}$ which are coadsorbed as anions and protons on the same slab. ^a Reaction i' indicates water-assisted hydrogen transfer mechanism i.e. cocatalytic water. ΔE is -0.22 eV more exothermic due to net conversion of chemisorbed water to physisorbed water. ^b Modified from Scheme 1 to use anionic OH^- from chemisorbed water. ^c Modified from Scheme 1 to use water as oxidant. ^d A spectator hydrogen atom is included in the calculation as methoxyl must be coadsorbed with a proton for charge balance. ^e The intrinsic barrier was less than the 0.44 eV water chemisorption barrier, so the larger of the two barriers is given.

Compared to oxidation, methylene hydroxylation possesses a lower activation energy barrier. The mechanism was very different as well. The reaction did not proceed in a single step, but rather in two separate steps owing to the high degree of coordination between the CH_2 adsorbate with anatase surface atoms. In the first part of the mechanism, the C-Ti bond broke and the methylene group only interacted with the surface via its C-O bond. This state was 0.78 eV higher in energy than the best binding orientation for CH_2 , and the transition state was an additional 0.26 eV higher, for a total activation energy barrier of 1.04 eV to reach this less-favorable binding geometry. The remainder of the reaction involved migration of the chemisorbed water OH group to methylene, forming a C-O bond. This reaction was 0.79 eV downhill with a 0.56 eV barrier. The highest energy

transition state for this reaction was 1.33 eV higher in energy than the reactants, and this barrier is reported in Table 5.3 and Figure 5.6.

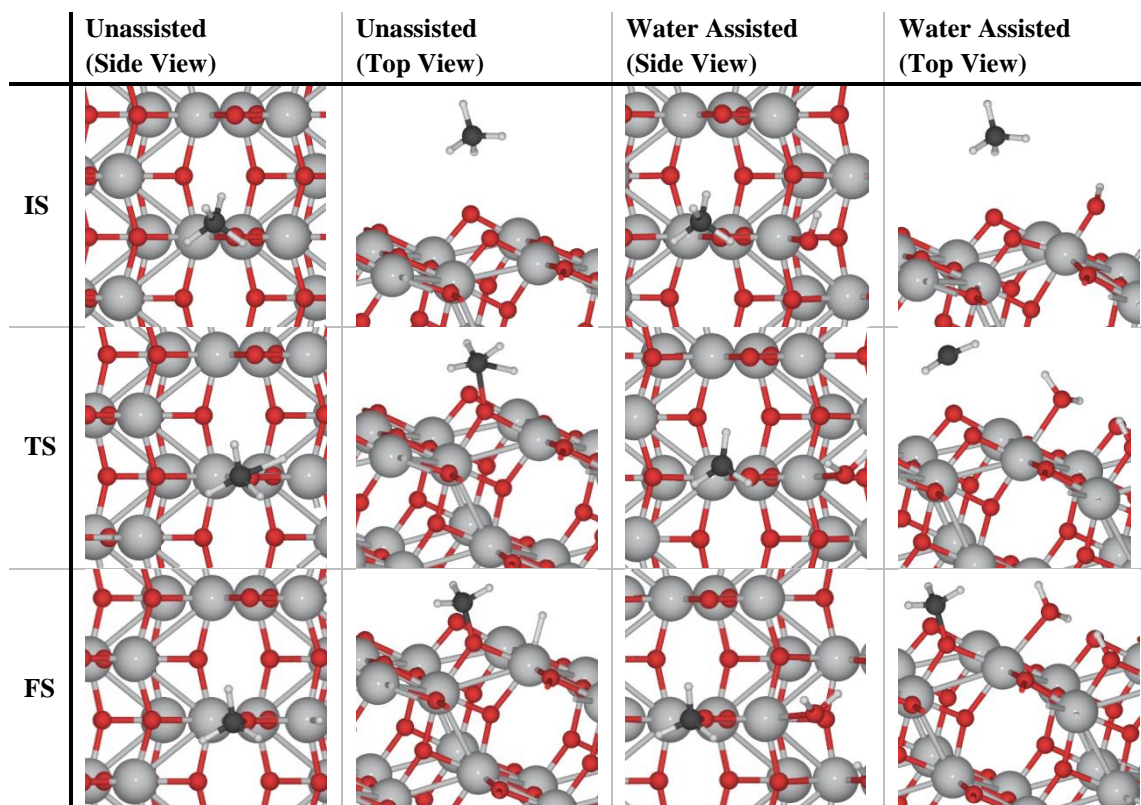


Figure 5.5 Methane hydrogenation mechanism unassisted (without participation of a cocatalytic water molecule) and with cocatalytic water. IS is the initial coadsorbed state, TS is the transition state, and FS is the final coadsorbed state. 0-5

Considering the three possible pathways to formaldehyde from methyl in the absence of cocatalytic water (Figure 5.6A), the comparison between the indirect and direct methylene pathways favors the indirect pathway with only a 1.33 eV barrier to add OH to CH₂ compared to 2.00 eV to add O. Both the indirect methylene and methoxyl pathways face steep dehydrogenation barriers for the dehydrogenation of a CH₃ group – in methyl dehydrogenation for the indirect methylene pathway and in methoxyl for the methoxyl pathway. Compared to gaseous methane and water reactants, these effective barriers were similar in energy, 4.64 eV and 4.75 eV respectively, and were even higher

in energy than the effective dehydrogenation barrier of methane of 4.09 eV. These three barriers dominate the potential energy surfaces, and the similarity in effective barriers means that the indirect methylene and methoxyl pathways are both competitive for the formation of formaldehyde. The dehydrogenation of formaldehyde to formyl was much lower in barrier compared to other dehydrogenation steps.

The elementary steps from formyl to gaseous CO and CO₂ was been discussed in detail in Chapter 4. In the context of MSR, the dehydrogenation barrier to CO is the highest energy point in any of the pathways, 6.29 eV compared to gaseous reactants. This means that the direct conversion of formyl to CO₂ was more favorable via the formate pathway.

5.3.5 Effect of Cocatalytic Water on Dehydrogenation Steps and MSR Pathways

Hydrogen transfer steps comprised the four largest kinetic barriers in the MSR pathways. These same steps can proceed with assistance from cocatalytic water, by having the OH group of chemisorbed water act as a hydrogen acceptor. The OH group can bridge the spatial gap between hydrogen adsorption sites and stabilize the energy of the transferred hydrogen in the transition state. This effect was previously described for hydrogen transfer steps in WGS, where it led to the formate pathway being competitive with the carboxyl pathway by lowering the CO hydrogenation barrier from 4.23 eV to 1.45 eV. This elementary step is the microscopic reverse of formyl dehydrogenation, Step 20 in Scheme 5.1, with a barrier of 4.97 eV in the absence of cocatalytic water. With cocatalytic water, formyl reacts with chemisorbed water (OH+H), and the products are CO and physisorbed water, with the adsorbed H from chemisorbed water acting as a spectator. The barrier is lowered to 1.96 eV. Due to the conversion of chemisorbed water

to physisorbed water, all reaction energies involving cocatalytic water appear -0.22 eV more exothermic in Table 5.3 than their unassisted counterparts. The activation of physisorbed water to form chemisorbed water is $+0.22$ eV uphill and closes the catalytic cycle. As chemisorption must precede any cocatalytic water reaction, the energy for water activation is included in the barriers of all such steps in Figure 5.6B. Further, for any dehydrogenation steps with intrinsic barriers less than the chemisorption barrier of 0.44 eV, the water activation step is the highest barrier and therefore is the barrier listed in Table 5.3 and shown in Figure 5.6B.

To investigate the cocatalytic effect of chemisorbed water in the dehydrogenation steps in MSR, reactants were coadsorbed on the same slab as OH+H. The minimum energy pathways to transfer hydrogen from the MSR intermediates to the OH group were calculated and the barriers for these water-assisted reactions are compared to the unassisted pathways in Table 5.3 and Figure 5.5. The effect on the initial methane activation step and its transition state structure are shown in Figure 5.5. One of the reasons for the very large barrier for methane activation was the lack of a suitable site near the product methyl adsorption site to place the removed hydrogen atom. In the unassisted pathway, this hydrogen was placed in a very unfavorable binding site atop Ti. In the presence of chemisorbed water, this site is occupied by OH which places a much better H-acceptor at roughly the same position. The transition state no longer involves five-coordinate carbon. Being an endothermic reaction, the late transition state resembles a gaseous CH_3 radical and physisorbed water. This CH_3 group then binds to the undercoordinated surface oxygen atom in the product state. The gas-like nature of the CH_3 group in the transition state means that there is little stabilization from interaction

with the anatase surface, but the reduction in the activation energy barrier by taking advantage of the cocatalytic water is substantial. The new barrier was only 2.95 eV, 2.02 eV lower than in the unassisted pathway. Though the barrier of nearly 3 eV is large, it is conceivable that reaction would occur at the very high temperatures used for methane steam reforming. It is also smaller than the band gap energy of anatase TiO_2 of 3.20 eV,¹²³ suggesting that photocatalytic conditions may be able activate the C-H bond.

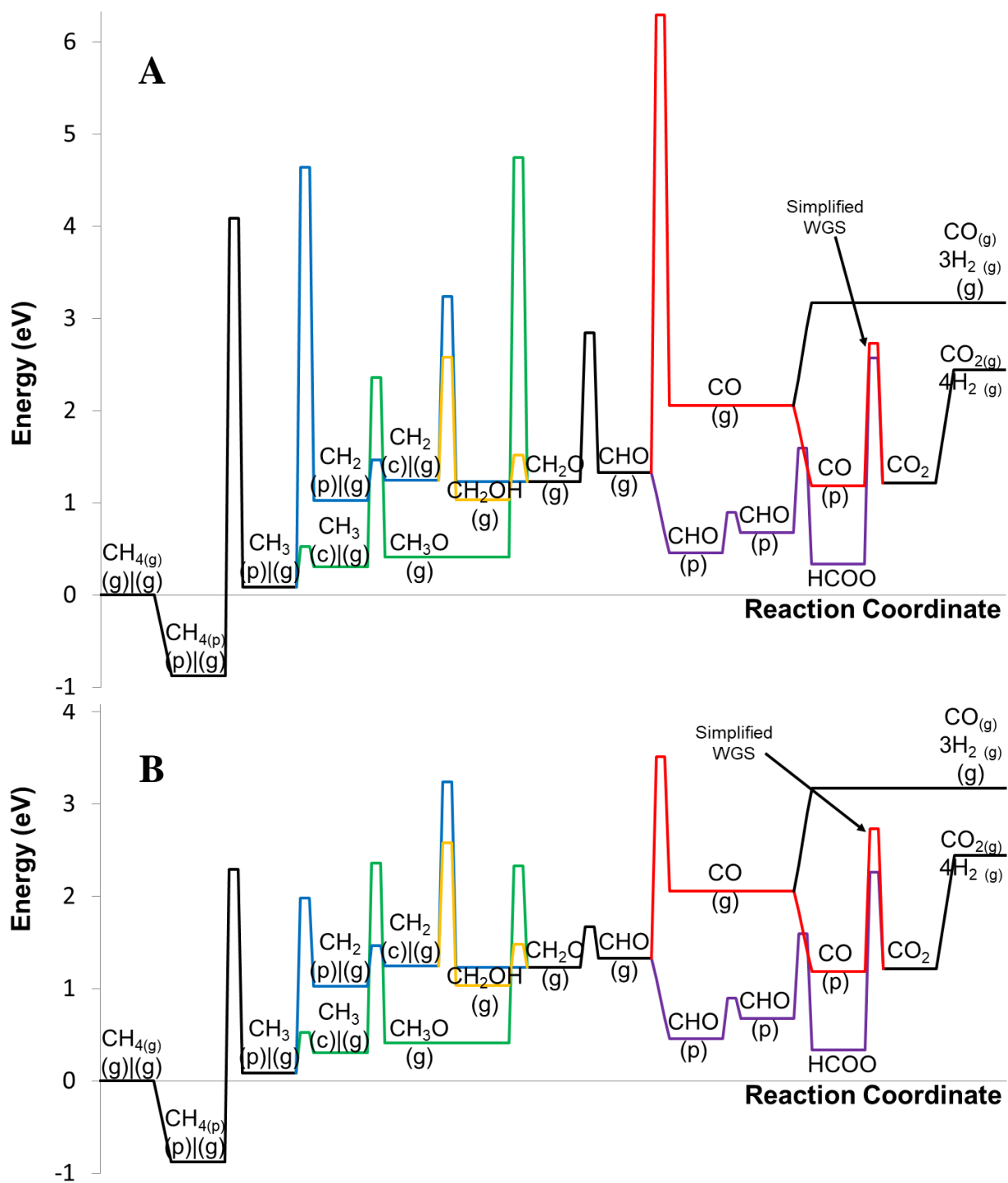


Figure 5.6 Reaction pathways without (A) and with (B) the effect of cocatalytic water on dehydrogenation barriers. Reaction steps common in all pathways shown in black, methoxyl pathway in green, direct methylene pathway in blue, indirect methylene (hydroxymethyl) pathway in yellow, CO/carboxyl WGS pathway in red, and formate WGS pathway in purple. See Figure 5.4 for labelling conventions. The energy to chemisorb water, +0.22 eV, is included in the barrier heights for reactions which utilize cocatalytic water in B. 0-4

Cocatalytic water played a similar role in lowering the activation energy barriers of dehydrogenation steps by having the OH group act as a hydrogen acceptor. The reactions with the largest unassisted dehydrogenation barriers, including methane dehydrogenation, showed the largest reductions. The barriers for dehydrogenating the CH₃ groups in adsorbed methyl and methoxyl were 4.55 eV and 4.33 eV without water, and were reduced to 1.68 eV and 1.69 eV respectively with cocatalytic water. The highest energy state in Figure 5.6A was the transition state for formyl dehydrogenation with a barrier of 4.97 eV which was reduced to 1.96 eV. Together with methane dehydrogenation, these four steps showed barrier reductions of >2 eV, with the formyl dehydrogenation barrier dropping by the largest margin, 3.0 eV.

These reductions in dehydrogenation barriers dramatically changed the appearance of the potential energy surfaces in Figure 5.6B. The methane activation barrier is only 2.29 eV relative to the gaseous reactants, and is comparable in energy to methyl oxidation (2.36 eV unchanged from Figure 5.6A) and methoxyl dehydrogenation barriers (2.33 eV). The methyl dehydrogenation transition state was previously higher in energy than the methane dehydrogenation transition state. Owing to its larger comparative barrier reduction, it is now slightly lower in energy (1.98 eV), no longer the highest energy state on the methylene pathways, and lower than both the methylene oxidation and hydroxylation transition states (2.58 eV and 3.24 eV respectively). The indirect methylene pathway is still preferred between these two, but its highest transition state, for the hydroxylation step, is slightly higher in energy than methane activation and any barrier in the methoxyl pathway. This gives a slight overall advantage to the methoxyl pathway. The highest point on any pathway is still the transition state for

formyl dehydrogenation. While the transition state for the cocatalytic dehydrogenation mechanism is now only 0.34 eV higher in energy than the gaseous $\text{CO}_{(\text{g})}$ product state, WGS via the formate pathway still appears to be more favorable. As the highest barrier in the formate pathway was dehydrogenation, even this barrier was reduced by 0.31 eV, ^{Error! Bookmark not defined.} bringing it below the desorption energies of all the products of the net reaction of methane to carbon dioxide.

Dehydrogenation reactions with smaller barriers saw smaller benefit from the participation of cocatalytic water in the reaction. The O-H cleavage in hydroxymethyl was already only 0.48 eV, and cocatalytic water steps still require water chemisorption, so the effective barrier could not be reduced below the chemisorption barrier of 0.44 eV. The formaldehyde dehydrogenation barrier of 1.62 eV was reduced significantly (calculated at 0.27 eV), and so effectively the barrier is that for water activation instead of C-H bond cleavage. In the unassisted formaldehyde mechanism, the distance between the hydrogen donor and the acceptor (a lattice oxygen atom) was 3.83 Å, while in the cocatalytic water case, the distance between the hydrogen donor and the acceptor (now the OH group of chemisorbed water) was 3.09 Å.

5.4 Conclusions

Periodic density functional theory calculations were carried out to investigate the mechanism of the methane steam reforming reaction on the (101) surface of anatase TiO_2 . Based on binding energies for surface intermediates generated from dehydrogenation, oxidation, and hydroxylation of methane and its derivatives, potential energy surfaces were generated to compare the thermodynamics of possible pathways from methane to both carbon monoxide and carbon dioxide as products. Due to steep

energetic penalties in dehydrogenation of methylene and hydroxymethyl, pathways involving these intermediates were not considered further. This meant that all steam reforming pathways on anatase TiO_2 were proposed to involve formaldehyde dehydrogenation to formyl. Three pathways were suggested. The methoxyl pathway involved oxidation of methyl followed by dehydrogenation of methoxyl. The direct methylene pathway involved dehydrogenation of methyl, followed by oxidation of methylene to formaldehyde. Due to the high barrier for CHO dehydrogenation, the water-gas shift reaction is expected to make CO_2 , rather than CO, the preferred product during MSR over metal-free TiO_2 .

Activation energy barriers calculated for reactions on clean anatase (101) surfaces showed very high >4.3 eV barriers for many dehydrogenation steps, especially the initial methane activation barrier to form surface methyl (4.96 eV), essentially making all MSR pathways equally unlikely. However, the addition of chemisorbed water to the anatase surface revealed the cocatalytic role of water in reducing the barriers of difficult dehydrogenation steps. The ability of the OH group to act as a hydrogen acceptor and form physisorbed water stabilized the most difficult dehydrogenation transition states by >2 eV. This led to much more feasible apparent activation energy barriers of 2.2-2.6 eV relative to gaseous methane and steam as reactants. Though differences were small, the methoxyl pathway was slightly preferred over the methylene pathways to form formaldehyde.

Even elementary reactions without hydrogen transfer benefitted from the presence of chemisorbed water. Direct oxidation and hydroxyl mechanisms using chemisorbed

water as a reactant were thermodynamically favored over reactions involving removing lattice oxygen to form oxygen vacancies.

These results further support the proposed active role of adsorbed water in catalyzing reactions on TiO_2 surfaces. The cocatalytic activity of water has the potential to dramatically alter potential energy landscapes on anatase surfaces, changing the expected surface species and their concentrations under reaction conditions. The metal-free calculations can help interpret the activity of the bare support for reactions of derivatives of methane, methanol, and formaldehyde on metal nanoparticles supported on anatase, and how intermediates of such reactions may interact with metal catalysts.

Bibliography

- ¹ Cavani, F.; Ballarini, N.; Cericola, A. Oxidative Dehydrogenation of Ethane and Propane: How Far From Commercial Implementation?, *Catalysis Today* 2007, 127, 113.
- ² Cavani, F.; Trifiro, F. The Oxidative Dehydrogenation of Ethane and Propane as an Alternative Way for the Production of Light Olefins, *Catalysis Today*, 1995, 24, 307.
- ³ Blasco, T.; Lopez Nieto, J.M. Oxidative Dehydrogenation of Short Chain Alkanes on Supported Vanadium Oxide Catalysts, *Applied Catalysis A: General*, 1997, 157, 117.
- ⁴ Khodakov, A.; Olthof, B.; Bell, A.T.; Iglesia, E., Structure and Catalytic Properties of Supported Vanadium Oxides: Support Effects on Oxidative Dehydrogenation Reactions, *Journal of Catalysis*, 1999, 181, 205.
- ⁵ Bhasin, M.M.; McCain, J.H.; Vora, B.V.; Imai, T.; Pujado, P.R., Dehydrogenation and Oxidative Dehydrogenation of Paraffins to Olefins, *Applied Catalysis A: General*, 2001, 221, 397.
- ⁶ Kondratenko, E.V.; Cherian, M.; Baerns, M.; Su, D.; Schlögl, R.; Wang, X.; Wachs, I.E., Oxidative Dehydrogenation of Propane over V/MCM-41 Catalysts: Comparison of O₂ and N₂O as Oxidants, *Journal of Catalysis* 2005, 234, 131-142.
- ⁷ Burch, R.; Garla, L.C., Platinum-tin Reforming Catalysts: II. Activity and Selectivity in Hydrocarbon Reactions, *Journal of Catalysis* 1981, 71, 360-372.
- ⁸ Bari  s, O.A.; Holmen, A.; Blekkan, E.A., Propane Dehydrogenation over Supported Pt and Pt-Sn Catalysts: Catalyst Preparation, Characterization, and Activity Measurements, *Journal of Catalysis* 1996, 158, 1-12.
- ⁹ Vu, B.K.; Song, M.B.; Ahn, I.Y.; Suh, Y.-W.; Suh, D.J.; Kim, J.S.; Shin, E.W., Location and Structure of Coke Generated over Pt-Sn/Al₂O₃ in Propane Dehydrogenation, *Journal of Industrial and Engineering Chemistry* 2011, 17, 71-76.
- ¹⁰ Absi-Halabi, M.; Stanislaus, A.; Trimm, D.L., Coke Formation on Catalysts During the Hydroprocessing of Heavy Oils, *Applied Catalysis*, 1991, 72, 1993.
- ¹¹ Bibby, D.M.; Howe, R.F.; McLellan, G.D., Coke Formation in High-Silica Zeolites, *Applied Catalysis A: General*, 1992, 93, 1.
- ¹² Bartholomew, C.H., Mechanisms of Catalyst Deactivation, *Applied Catalysis A: General*, 2001, 212, 17.
- ¹³ Baschuk, J.J.; Li, X. Carbon Monoxide Poisoning Of Proton Exchange Membrane Fuel Cells. *Fuel and Energy Abstracts* 2002, 43, 260.
- ¹⁴ Jones, G.; Jakobsen, J.; Shim, S.; Kleis, J.; Andersson, M.; Rossmeisl, J.; Abildpedersen, F.; Bligaard, T.; Helveg, S.; Hinnemann, B. First Principles Calculations And Experimental Insight Into Methane Steam Reforming Over Transition Metal Catalysts. *Journal of Catalysis* 2008, 259, 147-160.
- ¹⁵ Rostrup-Nielsen, J.; Sehested, J.; Noerskov, J. Hydrogen And Synthesis Gas By Steam- And CO₂ Reforming. *ChemInform* 2003, 34.
- ¹⁶ Shen, J.; Hill, J.M.; Watwe, R.M.; Spiewak, B.E.; Dumesic, J.A., Microcalorimetric, Infrared Spectroscopic, and DFT Studies of Ethylene Adsorption on Pt/SiO₂ and Pt-Sn/SiO₂ Catalysts, *Journal of Physical Chemistry B*, 1999, 103, 3923.
- ¹⁷ Watwe, R.M.; Cortright, R.D.; Mavrikakis, M.; Norskov, J.K.; Dumesic, J.A., Density Functional Theory Studies of the Adsorption of Ethylene and Oxygen on Pt (111) and Pt₃Sn (111), *Journal of Chemical Physics*, 2001, 114, 4663.
- ¹⁸ J.M. Essen, J. Haubrich, C. Becker, K. Wandelt, Adsorption of Ethene on Pt(111) and Ordered Pt_xSn/Pt(111) Surface Alloys: A Comparative HREELS and DFT Investigation. *Surface Science*. 601 (2007) 3472.
- ¹⁹ Nyk  nen, L.; Honkala, K., Density Functional Theory Study on Propane and Propene Adsorption on Pt (111) and PtSn Alloy Surfaces, *Journal of Physical Chemistry C*, 2011, 115, 9578.
- ²⁰ de Waard, C.; Lotz, U.; Milliams, D. Predictive Model For CO₂ Corrosion Engineering In Wet Natural Gas Pipelines. *CORROSION* 1991, 47, 976-985.
- ²¹ Siirola, J. The Impact Of Shale Gas In The Chemical Industry. *AIChE Journal* 2014, 60, 810-819.

-
- ²² Vu, B.K.; Song, M.B.; Ahn, I.Y.; Suh, Y.-W.; Suh, D.J.; Kim, J.S.; Shin, E.W., Location and Structure of Coke Generated over Pt–Sn/Al₂O₃ in Propane Dehydrogenation, *Journal of Industrial and Engineering Chemistry* 2011, 17, 71-76.
- ²³ Absi-Halabi, M.; Stanislaus, A.; Trimm, D.L., Coke Formation on Catalysts During the Hydroprocessing of Heavy Oils, *Applied Catalysis*, 1991, 72, 1993.
- ²⁴ Bibby, D.M.; Howe, R.F.; McLellan, G.D., Coke Formation in High-Silica Zeolites, *Applied Catalysis A: General*, 1992, 93, 1.
- ²⁵ Bartholomew, C.H., Mechanisms of Catalyst Deactivation, *Applied Catalysis A: General*, 2001, 212, 17.
- ²⁶ Peng, Z.; Somodi, F.; Helveg, S.; Kisielowski, C.; Specht, P.; Bell, A.T., High-resolution in situ and ex situ TEM Studies on Graphene Formation and Growth on Pt Nanoparticles, *Journal of Catalysis*, 2012, 286, 22.
- ²⁷ Tsai, Y.L.; Xu, C.; Koel, B.E., Chemisorption of Ethylene, Propylene and Isobutylene on Ordered Sn/Pt (111) Surface Alloys, *Surface Science* 1997, 385, 37.
- ²⁸ Zhao, H.; Koel, B.E., Reactivity of Ethyl Groups on a Sn/Pt (111) Surface Alloy, *Catalysis Letters* 2005, 99, 27.
- ²⁹ Zhao, H.; Koel, B.E., Influence of Coadsorbed Hydrogen on Ethylene Adsorption and Reaction on a ($\sqrt{3} \times \sqrt{3}$) R30°-Sn/Pt (111) Surface Alloy, *Langmuir*. 2005, 21, 971.
- ³⁰ Batzill, M.; Beck, D.E.; Koel, B.E., Electronic Contrast in Scanning Tunneling Microscopy of Sn–Pt (111) Surface Alloys, *Surface Science* 2000, 466, L821-L826.
- ³¹ Panja, C.; Saliba, N.; Koel, B.E., Coking Resistance of Pt–Sn Alloys Probed by Acetylene Chemisorption, *Catalysis Letters*, 2000, 68, 175.
- ³² Panja, C.; Saliba, N.; Koel, B.E., Acetylene Chemisorption on Sn/Pt (100) alloys, *Journal of Physical Chemistry B*, 2001, 105, 3786.
- ³³ Bednarova, L.; Lyman, C.E.; Rytter, E.; Holmen, A., Effect of Support on the Size and Composition of Highly Dispersed Pt–Sn Particles, *Journal of Catalysis*, 2002, 211, 335.
- ³⁴ Galvita, V.; Siddiqi, G.; Sun, P.; Bell, A.T., Ethane Dehydrogenation on Pt/Mg (Al) O and PtSn/Mg (Al) O Catalysts, *Journal of Catalysis*, 2010, 271, 209-219.
- ³⁵ Watwe, R.M.; Cortright, R.D.; Nørskov, J.K.; Dumesic, J.A., Theoretical Studies of Stability and Reactivity of C₂ Hydrocarbon Species on Pt Clusters, Pt (111), and Pt (211), *Journal of Physical Chemistry B*, 2000, 104, 2299.
- ³⁶ Chen, Y.; Vlachos, D.G., Hydrogenation of Ethylene and Dehydrogenation and Hydrogenolysis of Ethane on Pt (111) and Pt (211): a Density Functional Theory Study, *Journal of Physical Chemistry C*, 2010, 114, 4973.
- ³⁷ Yang, M.L.; Zhu, Y.A.; Fan, C.; Sui, Z.J.; Chen, D.; Zhou, X.G., DFT Study of Propane Dehydrogenation on Pt Catalyst: Effects of Step Sites, *Physical Chemistry Chemical Physics*, 2011, 13, 3257.
- ³⁸ Viñes, F.; Lykhach, Y.; Staudt, T.; Lorenz, M.P.A.; Papp, C.; Steinrück, H.-P.; Libuda, J.; Neyman, K.M.; Görling, A., Methane Activation by Platinum: Critical role of Edge and Corner Sites of Metal Nanoparticles, *Chemistry, A European Journal*, 2010, 16, 6530.
- ³⁹ Yang, M.L.; Zhu, Y.A.; Fan, C.; Sui, Z.J.; Chen, D.; Zhou, X.G., Density Functional Study of the Chemisorption of C 1, C 2 and C 3 Intermediates in Propane Dissociation on Pt (111), *Journal of Molecular Catalysis A: Chemical*, 2010, 321, 42.
- ⁴⁰ Yang, M.L.; Zhu, Y.A.; Zhou, X.G.; Sui, Z.J.; Chen, D., First-Principles Calculations of Propane Dehydrogenation over PtSn Catalysts, *ACS Catalysis*, 2012, 2, 1247-1258.
- ⁴¹ Wu, J.; Peng, Z.; Bell, A.T., Effects of Composition and Metal Particle Size on Ethane Dehydrogenation over Pt_xSn 100– x/Mg (Al) O (70 ≤ x ≤ 100), *Journal of Catalysis*, 2014, 311, 161-168.
- ⁴² Nykänen, L.; Honkala, K., Selectivity in Propene Dehydrogenation on Pt and Pt₃Sn Surfaces from First Principles, *ACS Catalysis*, 2013, 3, 3026.
- ⁴³ Kim, J.; Fu, J.; Podkolzin, S.G.; Koel, B.E., Studies of Ethylene Oxide Adsorption on Pt– Sn Alloys with TPD, HREELS, UPS, and DFT Calculations, *Journal of Physical Chemistry C*, 2010, 114, 17238.

-
- ⁴⁴ Alcala, R.; Shabaker, J.W.; Huber, G.W.; Sanchez-Castillo, M.A.; Dumesic, J.A., Experimental and DFT Studies of the Conversion of Ethanol and Acetic Acid on PtSn-based Catalysts, *Journal of Physical Chemistry B* 2005, 109, 2074-2085.
- ⁴⁵ Dupont, C.; Jugnet, Y.; Loffreda, D., Theoretical Evidence of PtSn Alloy Efficiency for CO Oxidation, *Journal of the American Chemical Society*, 2006, 128, 9129.
- ⁴⁶ Gulmen, M.A.; Sumer, A.; Aksoylu, A.E., Adsorption Properties of CO on Low-Index Pt 3 Sn surfaces, *Surface Science*, 2006, 600, 4909.
- ⁴⁷ Sumer, A.; Aksoylu, A.E., CO and O Coadsorption on Pt 3 Sn Studied by DFT: Changes in the Adsorptive Properties of the Surface with Alloying and Coverage, *Surface Science*, 2008, 602, 1636.
- ⁴⁸ Kim, J.; Welch, L.A.; Olivas, A.; Podkolzin, S.G.; Koel, B.E., Adsorption and Decomposition of Cyclohexanone (C₆H₁₀O) on Pt (111) and the (2×2) and ($\sqrt{3}\times\sqrt{3}$) R30°-Sn/Pt (111) Surface Alloys, *Langmuir*, 2010, 26, 16401.
- ⁴⁹ Kresse, G.; Furthmüller J., Efficiency of Ab-Initio Total Energy Calculations for Metals and Semiconductors using a Plane-Wave Basis Set, *Comput. Mater. Sci.* 1996, 6, 15-50.
- ⁵⁰ Kresse, G.; Furthmüller, J., Efficient Iterative Schemes for Ab Initio Total-Energy Calculations using a Plane-Wave Basis Set, *Phys. Rev. B* 1996, 54, 11169-11186.
- ⁵¹ Perdew, J.P.; Wang, Y., Accurate and Simple Analytic Representation of the Electron-Gas Correlation Energy, *Phys. Rev. B* 1992, 45, 13244-13249.
- ⁵² Blöchl, P.E., Projector Augmented-Wave Method, *Phys. Rev. B* 1994, 50, 17953-17979.
- ⁵³ Kresse, G.; Joubert, D., From Ultrasoft Pseudopotentials to the projector Augmented-Wave Method, *Phys. Rev. B* 1999, 59, 1758-1775.
- ⁵⁴ Jiang, L.; Sun, G.; Sun, S.; Liu, J.; Tang, S.; Li, H.; Zhou, B.; Xin, Q., Structure and Chemical Composition Of Supported Pt–Sn Electrocatalysts For Ethanol Oxidation, *Electrochimica Acta* 2005, 50, 5384-5389.
- ⁵⁵ Neugebauer, J.; Scheffler, M., Adsorbate-Substrate and adsorbate-Adsorbate Interactions of Na and K Adlayers on Al (111), *Phys. Rev. B* 1992, 46, 16067-16080.
- ⁵⁶ Monkhorst, H.J.; Pack, H.J., Special Points for Brillouin-Zone Integrations, *Phys. Rev. B* 1976, 13, 5188-5192.
- ⁵⁷ Henkelman, G.; Uberuaga, B. P.; Jonsson, H. J., A Climbing Image Nudged Elastic Band Method for Finding Saddle Points and Minimum Energy Paths, *Chem. Phys.* 2000, 113, 9901– 9904.
- ⁵⁸ Henkelman, G.; Arnaldsson, A.; Jónsson, H., A Fast and Robust Algorithm for Bader Decomposition Of Charge Density, *Comput. Mater. Sci.* 2006, 36, 254-360.
- ⁵⁹ Sanville, E.; Kenny, S. D.; Smith, R.; Henkelman, G. An Improved Grid-Based Algorithm for Bader Charge Allocation, *J. Comp. Chem.* 2007, 28, 899-908.
- ⁶⁰ Tang, W.; Sanville, E.; Henkelman, G. A Grid-Based Bader Analysis Algorithm without Lattice Bias, *J. Phys.: Condens. Matter* 2009, 21, 084204.
- ⁶¹ Yu, M.; Trinkle, D. R. Accurate and Efficient Algorithm for Bader Charge Integration, *J. Chem. Phys.* 2011, 134, 064111.
- ⁶² Hansen, M. Constitution of Binary Alloys, McGraw Hill, New York, 1958.
- ⁶³ Srinivasan, R.; Davis, B.H., The Structure of Platinum-Tin Reforming Catalysts, *Platinum Metals Review*, 1992, 36, 151-163.
- ⁶⁴ Ballarini, A.; Zgolicz, P.; Vilella, I.; de Miguel, S.; Castro, A.; Scelza, O., n-Butane Dehydrogenation on Pt, PtSn and PtGe Supported on γ -Al₂O₃ Deposited on Spheres of α -Al₂O₃ by Washcoating, *Applied Catalysis A: General* 2010, 381, 83-91.
- ⁶⁵ Moscu, A.; Schuurman, Y.; Veyre, L.; Thieuleux, C.; Meunier, F., Direct Evidence by in situ IR CO Monitoring of the Formation and the Surface Segregation of a Pt–Sn Alloy, *Chemical Communications* 2014, 50, 8590.
- ⁶⁶ Panja, C.; Saliba, N.; Koel, B., Adsorption of Methanol, Ethanol and Water on Well-Characterized Pt-Sn Surface Alloys, *Surface Science* 1998, 395, 248-259.
- ⁶⁷ Xu, C.; Koel, B., Dehydrogenation of Cyclohexene on Ordered Sn/Pt (111) Surface Alloys, *Surface Science* 1994, 304, 249-266.

-
- ⁶⁸ Samson, P.; Nesbitt, A.; Koel, B.; Hodgson, A., Deuterium Dissociation on Ordered Sn/Pt (111) Surface Alloys, *The Journal of Chemical Physics* 1998, *109*, 3255.
- ⁶⁹ Cortright, R.D.; Hill, J.M.; Dumesic J.A., Selective Dehydrogenation of Isobutane over Supported Pt/Sn Catalysts, *Catal. Today* 55 (2000) 213–223.
- ⁷⁰ Solomon, E. I.; Brunold, T. C.; Davis, M. I.; Kemsley, J. N.; Lee, S. K.; Lehnert, N.; Neese, F.; Skulan, A. J.; Yang, Y. S.; Zhou, J., Geometric and Electronic Structure/Function Correlations in Non-Heme Iron Enzymes, *Chem. Rev.* 2000, *100*, 235–350
- ⁷¹ Kogan, S.B.; Schramm, H.; Herskowitz, M., Dehydrogenation of Propane on Modified Pt/ θ -Alumina Performance in Hydrogen and Steam Environment, *Appl. Catal. A* 2001, *208*, 185-191.
- ⁷² Tasbihi, M.; Feyzi, F.; Amlashi, M.A.; Abdullah, A.Z.; Mohamed, A.R., Effect of the Addition of Potassium and Lithium in Pt–Sn/Al₂O₃ Catalysts for the Dehydrogenation of Isobutene, *Fuel Process. Technol.* 2007, *46*, 8722-8728.
- ⁷³ Han, Z.; Li, S.; Jiang, F.; Wang, T.; Ma, X.; Gong, J. Propane Dehydrogenation over Pt–Cu Bimetallic Catalysts: The Nature of Coke Deposition and the Role of Copper. *Nanoscale* **2014**, *6*, 10000-10008.
- ⁷⁴ Siddiqi, G.; Sun, P.; Galvita, V.; Bell, A. Catalyst Performance of Novel Pt/Mg(Ga)(Al)O Catalysts for Alkane Dehydrogenation. *J. Catal.* **2010**, *274*, 200-206.
- ⁷⁵ Sun, P.; Siddiqi, G.; Vining, W.; Chi, M.; Bell, A. Novel Pt/Mg(In)(Al)O Catalysts for Ethane and Propane Dehydrogenation. *J. Catal.* **2011**, *282*, 165-174.
- ⁷⁶ Hauser, A.; Gomes, J.; Bajdich, M.; Head-Gordon, M.; Bell, A. Subnanometer-Sized Pt/Sn Alloy Cluster Catalysts for the Dehydrogenation of Linear Alkanes. *Phys. Chem. Chem. Phys.* **2013**, *15*, 20727-20734.
- ⁷⁷ Chandler, B.; Rubinstein, L.; Pignolet, L. Alkane Dehydrogenation with Silica Supported Platinum and Platinum–Gold Catalysts Derived from Phosphine Ligated Precursors. *J. Mol. Catal. A-Chem.* **1998**, *133*, 267-282.
- ⁷⁸ Hamid, S.; Lambert, D.; Derouane, E. Dehydroisomerisation Of N-Butane over (Pt,Cu)/H-TON Catalysts. *Catal. Today* **2000**, *63*, 237-247.
- ⁷⁹ Bond, G.; Cunningham, R. Alkane Transformations on Supported Platinum Catalysts. *J. Catal.* **1997**, *166*, 172-185.
- ⁸⁰ Hook, A.; Massa, J.; Celik, F. Effect Of Tin Coverage On Selectivity For Ethane Dehydrogenation Over Platinum–Tin Alloys. *J. Phys. Chem. C* **2016**, *120*, 27307-27318
- ⁸¹ Selvarani, G.; Selvaganesh, S.; Krishnamurthy, S.; Kiruthika, G.; Sridhar, P.; Pitchumani, S.; Shukla, A. A Methanol-Tolerant Carbon-Supported Pt–Au Alloy Cathode Catalyst For Direct Methanol Fuel Cells And Its Evaluation By DFT. *J. Phys. Chem. C* **2009**, *113*, 7461-7468.
- ⁸² Xia, F.; Cao, Z. Relativistic DFT Studies of Dehydrogenation of Methane By Pt Cationic Clusters: Cooperative Effect Of Bimetallic Clusters. *J. Phys. Chem. A* **2006**, *110*, 10078-10083.
- ⁸³ This is a simplification, as carbon formation need not necessarily proceed through ethene as an intermediate,⁸⁰ especially on pure Pt. Regardless, the opposite – stronger ethene binding – will certainly make selectivity to ethene worse.
- ⁸⁴ It should also be noted that PtHg is a liquid at elevated temperature reaction conditions, and will function vastly different from the other alloys.
- ⁸⁵ Santen, R.; Neurock, M.; Shetty, S. Reactivity Theory of Transition-Metal Surfaces: A Brønsted–Evans–Polanyi Linear Activation Energy–Free-Energy Analysis. *Chem. Rev.* **2010**, *110*, 2005-2048.
- ⁸⁶ Skúlason, E.; Karlberg, G.; Rossmeisl, J.; Bligaard, T.; Greeley, J.; Jónsson, H.; Nørskov, J. Density Functional Theory Calculations for the Hydrogen Evolution Reaction in an Electrochemical Double Layer on the Pt(111) Electrode. *Phys. Chem. Chem. Phys.* **2007**, *9*, 3241-3250.
- ⁸⁷ Bligaard, T.; Nørskov, J.K.; Dahl, S.; Matthiesen, J.; Christensen, C.H.; Sehested, J. The Brønsted–Evans–Polanyi Relation and the Volcano Curve in Heterogeneous Catalysis. *J. Catal.* **2004**, *224*, 206-217.

-
- ⁸⁸ Agrafiotis, C.; von Storch, H.; Roeb, M.; Sattler, C. Solar Thermal Reforming of Methane Feedstocks for Hydrogen and Syngas Production—A Review. *Renewable and Sustainable Energy Reviews* **2014**, *29*, 656-682.
- ⁸⁹ Barreto, L.; Makihiro, A.; Riahi, K. The Hydrogen Economy in the 21st Century: A Sustainable Development Scenario. *International Journal of Hydrogen Energy* **2003**, *28*, 267-284.
- ⁹⁰ Chen, H.; Ding, Y.; Cong, N.; Dou, B.; Dupont, V.; Ghadiri, M.; Williams, P. Progress in Low Temperature Hydrogen Production with Simultaneous CO₂ Abatement. *Chemical Engineering Research and Design* **2011**, *89*, 1774-1782.
- ⁹¹ Dry, M. E. The Fischer–Tropsch Process: 1950–2000. *Catalysis Today*, **2002**, *71*, 227-241.
- ⁹² Alayoglu, S.; Nilekar, A. U.; Mavrikakis, M.; Eichhorn, B. Ru–Pt Core–shell Nanoparticles for Preferential Oxidation of Carbon Monoxide in Hydrogen. *Nature Materials*, **2008**, *7*, 333-338.
- ⁹³ Fu, Q.; Saltsburg, H.; Flytzani-Stephanopoulos, M. Active Nonmetallic Au and Pt Species on Ceria-based Water-gas Shift Catalysts. *Science*, **2003**, *301*, 935-938.
- ⁹⁴ Pistonesi, C.; Juan, A.; Irigoyen, B.; Amadeo, N. Theoretical and Experimental Study of Methane Steam Reforming Reactions Over Nickel Catalyst. *Applied Surface Science* **2007**, *253*, 4427-4437.
- ⁹⁵ Li, Y.; Fu, Q.; Flytzani-Stephanopoulos, M. Low-temperature Water-gas Shift Reaction over Cu- and Ni-loaded Cerium Oxide Catalysts. *Applied Catalysis B: Environmental*, **2000**, *27*, 179-191.
- ⁹⁶ Rodríguez, J.A.; Ma, S.; Liu, P.; Hrbek, J.; Evans, J.; Perez, M. Activity of CeO_x and TiO_x Nanoparticles Grown on Au (111) in the Water-gas Shift Reaction. *Science*, **2007**, *318*, 1757-1760.
- ⁹⁷ Si, R.; Flytzani-Stephanopoulos, M. Shape and Crystal-Plane Effects of Nanoscale Ceria on the Activity of Au–CeO₂ Catalysts for the Water–Gas Shift Reaction. *Angewandte Chemie*, **2008**, *120*, 2926-2929.
- ⁹⁸ Fu, Q.; Weber, A.; Flytzani-Stephanopoulos, M. Nanostructured Au–CeO₂ Catalysts for Low-temperature Water–gas Shift. *Catalysis Letters*, **2001**, *77*, 87-95.
- ⁹⁹ Panagiotopoulou, P.; Kondarides, D.I. Effect of Morphological Characteristics of TiO₂-supported Noble Metal Catalysts on their Activity for the Water–gas Shift Reaction. *Journal of Catalysis*, **2004**, *225*, 327-336.
- ¹⁰⁰ Rodríguez, J. A.; Evans, J.; Graciani, J.; Park, J. B.; Liu, P.; Hrbek, J.; Sanz, J. F. High Water-Gas Shift Activity in TiO₂ (110) Supported Cu and Au Nanoparticles: Role of the Oxide and Metal Particle Size. *Journal of Physical Chemistry C*, **2009**, *113*, 7364-7370.
- ¹⁰¹ Park, J.B.; Graciani, J.; Evans, J.; Stacchiola, D.; Senanayake, S.D.; Barrio, L.; Liu, P.; Sanz, J.F.; Hrbek, J.; Rodriguez, J.A. Gold, Copper, and Platinum Nanoparticles Dispersed on CeO_x/TiO₂ (110) Surfaces: High Water-Gas Shift Activity and the Nature of the Mixed-Metal Oxide at the Nanometer Level. *Journal of the American Chemical Society*, **2009**, *132*, 356-363.
- ¹⁰² Kim, H.Y.; Liu, P. Tuning the Catalytic Selectivity of Copper Using TiO₂: Water-Gas Shift versus CO Oxidation. *ChemCatChem*, **2013**, *5*, 3673-3679.
- ¹⁰³ Bunluesin, T.; Gorte, R.J.; Graham, G.W. Studies of the Water-gas-shift Reaction on Ceria-supported Pt, Pd, and Rh: Implications for Oxygen-storage Properties. *Applied Catalysis B: Environmental*, **1998**, *15*, 107-114.
- ¹⁰⁴ Henderson, M.A. Structural Sensitivity in the Dissociation of Water on TiO₂ Single-Crystal Surfaces. *Langmuir* **1996**, *12*, 5093-5098.
- ¹⁰⁵ Lindan, P.J.D.; Harrison, N.M.; Holender, J. M.; Gillan, M.J. First-principles Molecular Dynamics Simulation of Water Dissociation on TiO₂ (110). *Chemical Physics Letters*, **1996**, *261*, 246-252.
- ¹⁰⁶ Bikondoa, O.; Pang, C.L.; Ithnin, R.; Murn, C.A.; Onishi, H.; Thornton, G. Direct Visualization of Defect-Mediated Dissociation of Water on TiO₂ (110). *Nature Materials*, **2006**, *5*, 189-192.
- ¹⁰⁷ Panagiotopoulou, P.; Kondarides, D.I. Effect of the Nature of the Support on the Catalytic Performance of Noble Metal Catalysts for the Water–gas Shift Reaction. *Catalysis Today*, **2006**, *112*, 49-52.
- ¹⁰⁸ Olympiou, G.G.; Kalamaras, C.M.; Zeinalipour-Yazdi, C.D.; Efstathiou, A.M. Mechanistic Aspects of the Water–gas Shift Reaction on Alumina-supported Noble Metal Catalysts: In Situ DRIFTS and SSITKA-mass Spectrometry Studies. *Catalysis Today*, **2007**, *127*, 304-318.
- ¹⁰⁹ Bruix, A.; Rodriguez, J.A.; Ramirez, P.J.; Senanayake, S.D.; Evans, J.; Park, J.B.; Stacchiola, D.; Liu, P.; Hrbek, J.; Illas, F.; A New Type of Strong Metal–Support Interaction and the Production of H₂

- through the Transformation of Water on Pt/CeO₂ (111) and Pt/CeO_x/TiO₂ (110) Catalysts. *Journal of the American Chemical Society*, **2012**, *134*, 8968-8974.
- ¹¹⁰ Ammal, S.C.; Heyden, A. Origin of the Unique Activity of Pt/TiO₂ catalysts for the Water-gas Shift Reaction. *Journal of catalysis*, **2013**, *306*, 78-90.
- ¹¹¹ Ammal, S.C.; Heyden, A.; Nature of Pt_n/TiO₂ (110) Interface under Water-gas Shift Reaction Conditions: A Constrained ab Initio Thermodynamics Study. *Journal of Physical Chemistry C*, **2011**, *115*, 19246-19259.
- ¹¹² Xue, E.; O'Keeffe, M.; Ross, J. Water-Gas Shift Conversion Using a Feed with a Low Steam to Carbon Monoxide Ratio and Containing Sulphur. *Catalysis Today* **1996**, *30*, 107-118.
- ¹¹³ Fiolitis, E.; Hofmann, H. Dependence of the Kinetics of the Low-temperature Water-gas Shift Reaction on the Catalyst Oxygen Activity as Investigated by Wavefront Analysis. *Journal of Catalysis* **1983**, *80*, 328-339.
- ¹¹⁴ Amadeo, N. E.; Laborde, M.A. Hydrogen Production from the Low-temperature Water-gas Shift Reaction: Kinetics and Simulation of the Industrial Reactor. *International Journal of Hydrogen Energy* **1995**, *20*, 949-956.
- ¹¹⁵ Keiski, R.L.; Desponds, O.; Chang, Y.F.; Somorjai, G.A. Kinetics of the Water-gas Shift Reaction over Several Alkane Activation and Water-gas Shift Catalysts. *Applied Catalysis A: General*, **1993**, *101*, 317-338.
- ¹¹⁶ Grenoble, D.C.; Estadt, M.M.; Ollis, D.F. The Chemistry and Catalysis of the Water Gas Shift Reaction: 1. The Kinetics Over Supported Metal Catalysts. *Journal of Catalysis* **1981**, *67*, 90-102.
- ¹¹⁷ Gorte, R.J.; Zhao, S. Studies of the Water-gas-shift Reaction with Ceria-supported Precious Metals. *Catalysis Today*, **2005**, *104*, 18-24.
- ¹¹⁸ Yoshihara, J.; Parker, S.C.; Schafer, A.; Campbell, C.T. Methanol Synthesis and Reverse Water-gas Shift Kinetics Over Clean Polycrystalline Copper. *Catalysis Letters*, **1995**, *31*, 313-324.
- ¹¹⁹ Shekhar, M.; Wang, J.; Lee, W.S.; Williams, W.D.; Kim, S.M.; Stach, E.A.; Miller, J.T.; Delgass, W.N.; Ribeiro, F.H. Size and Support Effects for the Water-gas Shift Catalysis Over Gold Nanoparticles Supported on Model Al₂O₃ and TiO₂. *Journal of the American Chemical Society*, **2012**, *134*, 4700-4708.
- ¹²⁰ Grabow, L.C.; Gokhale, A.A.; Evans, S.T.; Dumesic, J.A.; Mavrikakis, M. Mechanism of the Water Gas Shift Reaction on Pt: First Principles, Experiments, and Microkinetic Modeling. *Journal of Physical Chemistry C* **2008**, *112*, 4608-4617.
- ¹²¹ Gokhale, A.A.; Dumesic, J.A.; Mavrikakis, M. On the Mechanism of Low-temperature Water Gas Shift Reaction on Copper. *Journal of the American Chemical Society* **2008**, *130*, 1402-1414.
- ¹²² Zhai, Y.; Pierre, D.; Si, R.; Deng, W.; Ferrin, P.; Nilekar, A.U.; Peng, G.; Herron, J.A.; Bell, D.C.; Saltsburg, H.; Mavrikakis, M.; Flytzani-Stephanopoulos, M. Alkali-Stabilized Pt-OH_x Species Catalyze Low-Temperature Water-Gas Shift Reactions. *Science*, **2010**, *329*, 1633-1636.
- ¹²³ Scanlon, D.O.; Dunnill, C.W.; Buckeridge, J.; Shevlin, S.A.; Logsdail, A.J.; Woodley, S.M.; Catlow, C.R.A.; Powell, M.J.; Palgrave, R.G.; Parkin, I.P.; Watson, G.W.; Keal, T.W.; Sherwood, P.; Walsh, A.; Sokol, A.A. Band Alignment of Rutile and Anatase TiO₂. *Nature Materials*, **2013**, *12*, 798-801.
- ¹²⁴ Linsebigler, A.; Lu, G.; Yates, J. Photocatalysis On TiO₂ Surfaces: Principles, Mechanisms, And Selected Results. *Chemical Reviews*, **1995**, *95*, 735-758.
- ¹²⁵ Luttrell, T.; Halpegamage, S.; Tao, J.; Kramer, A.; Sutter, E.; Batzill, M. Why is Anatase A Better Photocatalyst Than Rutile? – Model Studies on Epitaxial TiO₂ Films. *Scientific Reports*, **2014**, *4*, 4043.
- ¹²⁶ Park, J.B.; Graciani, J.; Evans, J.; Stacchiola, D.; Ma, S.G.; Liu, P.; Nambu, A.; Sanz, J.F.; Hrbek, J.; Rodriguez, J.A. High Catalytic Activity of Au/CeO_x/TiO₂(110) Controlled by the Nature of the Mixed-metal Oxide at the Nanometer Level *Proceedings of the National Academy of Sciences of the United States of America*. **2009**, *106*, 2009, 4975-4980.
- ¹²⁷ Panagiotopoulou, P.; Christodoulakis, A.; Kondarides, D.I.; Boghosian, S. Particle Size Effects on the Reducibility of Titanium Dioxide and its Relation to the Water-gas Shift Activity of Pt/TiO₂ Catalysts. *Journal of Catalysis*. **2006**, *240*, 114-125.
- ¹²⁸ Bocuzzi, F.; Chiorino, A.; Manzoli, M.; Andreeva, D.; Tabakova, T.; Ilieva, L.; Iadakev, V. Gold, Silver and Copper Catalysts Supported on TiO₂ for Pure Hydrogen Production, *Catalysis Today*. **2002**, *75*, 169-175.

-
- ¹²⁹ Burke, K. Perspective on Density Functional Theory. *Journal of Chemical Physics* . **2012**, *136* , 150901.
- ¹³⁰ Wang, J.; Tafen, D.N.; Lewis, J.P.; Hong, Z.L.; Manivannan, A.; Zhi, M.J.; Li, M.; Wu, N.Q. Origin of Photocatalytic Activity of Nitrogen-doped TiO₂ Nanobelts. *Journal of the American Chemical Society* **2009**, *131*, 12290-12297.
- ¹³¹ Di Valentin, C.; Finazzi, E.; Pacchioni, G.; Selloni, A.; Livraghi, S.; Paganini, M.; Giamello, E. N-Doped TiO₂: Theory And Experiment. *Chemical Physics* **2007**, *339*, 44-56.
- ¹³² Morgan, B.J.; Watson, G.Q. A DFT+U Description of Oxygen Vacancies at the TiO₂ Rutile (110) Surface. *Surface Science* **2007**, *601*, 5034-5041.
- ¹³³ Tilocca, A.; Selloni, A. Structure and Reactivity of Water Layers on Defect-Free and Defective Anatase TiO₂(101) Surfaces. *Journal of Physical Chemistry B*. **2004**, *108*, 4743-4751.
- ¹³⁴ Aschauer, U.; He, Y.; Cheng, H.; Li, S.-C.; Diebold, U.; Selloni, A. Influence of Subsurface Defects on the Surface Reactivity of TiO₂: Water on Anatase (101). *Journal of Physical Chemistry C*. **2010**, *114*, 1278-1284.
- ¹³⁵ Sun, C.; Liu, L.-M.; Selloni, A.; Lu, G.Q.(M.); Smith, S.C. Titania-water Interactions: A Review of Theoretical Studies. *Journal of Materials Chemistry*. **2010**, *20*, 10319-10334.
- ¹³⁶ Aschauer, U.J.; Tilocca, A.; Selloni, A. *Ab Initio* Simulations of the Structure of Thin Water Layers on Defective Anatase TiO₂(101) Surfaces. *International Journal of Quantum Chemistry* **2015**, *115*, 1250–1257.
- ¹³⁷ Perdew, J.P.; Burke, K.; Ernzerhof, M. Generalized Gradient Approximation Made Simple. *Physical Review Letters* **1997**, *78*, 1396.
- ¹³⁸ Anisimov, V.I.; Korotin, M.A.; Mylnikova, A.S.; Kozhevnikov, A.V.; Korotin, D.M.; Lorenzana, J. Computation of Stripes in Cuprates within the LDA+U Method, *Physical Review B* **2004**, *70*, 172501.
- ¹³⁹ Dudarev, S.L.; Botton, G.A.; Savrasov, S.Y.; Humphreys, C.J.; Sutton, A.P. Electron-energy-loss Spectra and the Structural Stability of Nickel Oxide: An LSDA+U Study. *Physical Review B* **1998**, *57*, 1505.
- ¹⁴⁰ Allen, J.; Watson, G. Occupation Matrix Control of D- And F-Electron Localisations Using DFT + U. *Physical Chemistry Chemical Physics* **2014**, *16*, 21016-21031.
- ¹⁴¹ Hu, Z.; Metiu, H. Choice of U for DFT+U Calculations for Titanium Oxides. *Journal of Physical Chemistry C* **2011**, *115*, 5841-5845.
- ¹⁴² Morgan, B.; Watson, G. A DFT+U Description of Oxygen Vacancies at the TiO₂ Rutile (110) Surface. *Surface Science* **2007**, *601*, 5034-5041.
- ¹⁴³ Howard, C.; Sabine, T.; Dickson, F. Structural and Thermal Parameters for Rutile and Anatase. *Acta Crystallographica Section B Structural Science* **1991**, *47*, 462-468.
- ¹⁴⁴ Geng, Z.; Chen, X.; Yang, W.; Gui, Q.; Xu, C.; Dai, D.; Yang, X. Highly Efficient Water Dissociation on Anatase TiO₂(101). *Journal of Physical Chemistry C*. **2016**, *120*, 26807-26813.
- ¹⁴⁵ Qunjun, X.; Yu, J.; Wong, P.K. Quantitative Characterization of Hydroxyl Radicals Produced by Various Photocatalysts. *Journal of Colloid and Interface Science* **2011**, *357*, 163-167.
- ¹⁴⁶ Hirakawa, T.; Nosaka, Y. Properties of O₂•- and OH• Formed in TiO₂ Aqueous Suspensions by Photocatalytic Reaction and the Influence of H₂O₂ and Some Ions. *Langmuir* **2002**, *18*, 3247-3254.
- ¹⁴⁷ Bronkema, J.L.; Leo, D.C.; Bell, A.T. Mechanistic Studies of Methanol Oxidation to Formaldehyde on Isolated Vanadate Sites Supported on High Surface Area Anatase. *Journal of Physical Chemistry C*. **2007**, *111*, 14530-14540.
- ¹⁴⁸ Maeda, Y.; Iizuka, Y.; Kohyama, M. Generation of Oxygen Vacancies at a Au/TiO₂ Perimeter Interface During CO Oxidation Detected by In situ Electrical Conductance Measurement. *Journal of the American Chemical Society*, **2013**, *135*, 906-909.
- ¹⁴⁹ Yamakata, A.; Ishibashi, T.; Onishi, H. Water- and Oxygen-Induced Decay Kinetics of Photogenerated Electrons in TiO₂ and Pt/TiO₂: A Time-Resolved Infrared Absorption Study. *Journal of Physical Chemistry, B* **2001**, *105*, 7258-7262.
- ¹⁵⁰ Zafir, M.; Gavrilidis, A. Catalytic Combustion Assisted Methane Steam Reforming in a Catalytic Plate Reactor. *Chemical Engineering Science* **2003**, *58*, 3947-3960.
- ¹⁵¹ Xu, J.; Froment, G. Methane Steam Reforming, Methanation and Water-Gas Shift: I. Intrinsic Kinetics. *AIChE Journal* **1989**, *35*, 88-96.

-
- ¹⁵² Wang, F.; Tan, J.; Ma, L.; Leng, Y. Effects of Key Factors on Solar Aided Methane Steam Reforming in Porous Medium Thermochemical Reactor. *Energy Conversion and Management* **2015**, *103*, 419-430.
- ¹⁵³ Ahmed, K.; Foger, K. Kinetics of Internal Steam Reforming of Methane on Ni/YSZ-Based Anodes for Solid Oxide Fuel Cells. *Catalysis Today* **2000**, *63*, 479-487.
- ¹⁵⁴ Wei, J.; Iglesia, E. Reaction Pathways and Site Requirements for the Activation and Chemical Conversion of Methane on Ru-Based Catalysts. *Journal of Physical Chemistry B* **2004**, *108*, 7253-7262.
- ¹⁵⁵ Ligthart, D.; van Santen, R.; Hensen, E. Influence of Particle Size on the Activity and Stability in Steam Methane Reforming of Supported Rh Nanoparticles. *Journal of Catalysis* **2011**, *280*, 206-220.
- ¹⁵⁶ Shinde, V.M.; Madras, G. Catalytic Performance of Highly Dispersed Ni/TiO₂ for Dry and Steam Reforming of Methane. *RSC Advances* **2014**, *4*, 4817-4826.
- ¹⁵⁷ Kho, E.T.; Scott, J.; Amal, R. Ni/TiO₂ for Low Temperature Steam Reforming of Methane. *Chemical Engineering Science* **2016**, *140*, 161-170.
- ¹⁵⁸ Li, K.; Jia, L.; Wang, X.; Pu, J.; Chi, B.; Li, J. Enhanced Methane Steam Reforming Activity and Electrochemical Performance of Ni_{0.9}Fe_{0.1}-supported Solid Oxide Fuel Cells with Infiltrated Ni-TiO₂ Particles. *Scientific Reports* **2016**, *6*, 35981.
- ¹⁵⁹ Chiarello, G.L.; Aguirre, M.H.; Selli, E. Hydrogen Production by Photocatalytic Steam Reforming of Methanol on Noble Metal-modified TiO₂. *Journal of Catalysis* **2010**, *273*, 182-190.
- ¹⁶⁰ Nichele, V.; Signoretto, M.; Menegazzo, F.; Rossetti, I.; Cruciani, G.; Hydrogen Production by Ethanol Steam Reforming: Effect of the Synthesis Parameters on the Activity of Ni/TiO₂ Catalysts. *International Journal of Hydrogen Energy* **2014**, *39*, 4252-4258.
- ¹⁶¹ Rossetti, I.; Gallo, A.; Dal Santo, V.; Bianchi, C.L.; Nichele, V.; Signoretto, M.; Finocchio, E.; Ramis, G.; Di Michele, A. Nickel Catalysts Supported Over TiO₂, SiO₂ and ZrO₂ for the Steam Reforming of Glycerol. *ChemCatChem* **2013**, *5*, 294-306.
- ¹⁶² Yoshida, H.; Hirao, K.; Nishimoto, J.I.; Shimura, K.; Kato, S.; Itoh, H.; Hattori, T. Hydrogen Production from Methane and Water on Platinum Loaded Titanium Oxide Photocatalysts. *Journal of Physical Chemistry C* **2008**, *112*, 5542-5551.
- ¹⁶³ Shimura, K.; Yoshida, H. Hydrogen Production from Water and Methane over Pt-loaded Calcium Titanate Photocatalyst. *Energy & Environmental Science* **2010**, *3*, 615-617.
- ¹⁶⁴ Shimura, K.; Kawai, H.; Yoshida, T.; Yoshida, H. Bifunctional Rhodium Cocatalysts for Photocatalytic Steam Reforming of Methane over Alkaline Titanate. *ACS Catalysis* **2012**, *2*, 2126-2134.
- ¹⁶⁵ Yoshida, H.; Kato, S.; Hirao, K.; Nishimoto, J.I.; Hattori, T. Photocatalytic Steam Reforming of Methane Over Platinum-loaded Semiconductors for Hydrogen Production. *Chemistry Letters* **2007**, *36*, 430-431.
- ¹⁶⁶ Shimura, K.; Kato, S.; Yoshida, T.; Itoh, H.; Hattori, T.; Yoshida, H. Photocatalytic Steam Reforming of Methane Over Sodium Tantalate. *Journal of Physical Chemistry C* **2010**, *114*, 3493-3503.
- ¹⁶⁷ Shimura, K.; Yoshida, T.; Yoshida, H. Photocatalytic Activation of Water and Methane over Modified Gallium Oxide for Hydrogen Production. *Journal of Physical Chemistry C* **2010**, *114*, 11466-11474.
- ¹⁶⁸ Pennington, A.M.; Yang, R.A.; Munoz, D.T.; Celik, F.E. Characterization and Catalytic Activity for Metal-Free Hydrogen Evolution of Defect-Rich Anatase Titanium Dioxide. **2018**, manuscript in preparation.
- ¹⁶⁹ Ravi, M.; Ranocchiari, M. van Bokhoven, J.A. The Direct Catalytic Oxidation of Methane to Methanol-A Critical Assessment. *Angewandte Chemie-International Edition* **2017**, *56*, 16464-16483.